

Processing development of 4TaC-HfC and related carbides and borides for extreme environments

by

Osama Gaballa Bahig Gaballa

A dissertation submitted to the graduate faculty

in partial fulfillment of the requirements for the degree of

DOCTOR OF PHILOSOPHY

Major: Materials Science and Engineering

Program of Study Committee:

Alan M. Russell, Major Professor

Vitalij Pecharsky

Scott Chumbley

Kristen Constant

Sriram Sundararajan

Iowa State University

Ames, Iowa

2012

Copyright © Osama Gaballa Bahig Gaballa, 2012. All rights reserved.

Table of Contents

Abstract	1
Chapter 1: Introduction	4
1.1 Aluminum Silicon Carbide (Al_4SiC_4)	4
1.2 Tantalum Hafnium Carbide (4TaC-HfC)	5
1.2.1 Tantalum Carbide (TaC)	5
1.2.2 Hafnium Carbide	9
1.2.3 Tantalum Hafnium Carbide (Ta_4HfC_5)	10
1.3 Tungsten Tetraboride (WB_4), and Tantalum Tetraboride (TaB_4)	13
1.4 Aluminum magnesium boride (AlMgB_{14})	14
1.4.1 Structure	14
1.4.2 Synthesis	15
1.4.3 Mechanical Properties	16
1.5 Mechanical Alloying	18
1.5.1 The process of mechanical alloying	19
1.5.2 Raw materials	19
1.5.3 Types of mills	20
1.5.3.1 SPEX shaker mills	20
1.5.3.2 Planetary ball mills	21
1.5.3.3 Attritor mills	21
1.5.4 Process variables	22
1.5.4.1 Type of mill	22
1.5.4.2 Milling container	23
1.5.4.3 Milling speed	23
1.5.4.4 Milling time	23
1.5.4.5 Grinding medium	24
1.5.4.6 Ball-to-powder-weight ratio (BPR)	24
1.5.4.7 Extent of filling the vial	25
1.5.4.8 Milling atmosphere	25

Chapter 2: General experimental procedures	26
2.1 Preparation of the starting powders	26
2.2 Consolidation	27
2.3 Evaluation	28
 Chapter 3: Formation, densification, and selected mechanical properties of hot pressed Al_4SiC_4, Al_4SiC_4 with 30 vol. % WC, and Al_4SiC_4 with 30 vol. % TiC	32
3.1 Abstract	32
3.2 Introduction	32
3.3 Experimental	33
3.3.1 Preparation of the starting powders	33
3.3.2 Consolidation	34
3.3.3 Evaluation	34
3.4 Results and discussion	35
3.4.1 Formation, densification, and XRD analysis of the samples	35
3.4.2 Microstructure	38
3.4.3 Mechanical properties	41
3.5 Conclusions	44
3.6 Acknowledgements	45
 Chapter 4: Properties of AlMgB_{14} hot pressed with additions of ZrB_2 and HfB_2	46
4.1 Abstract	46
4.2 Introduction	47
4.3 Experimental	48
4.4 Results and discussion	50
4.4.1 XRD	50
4.4.2 Microstructure of AlMgB_{14} samples with additions of ZrB_2	51
4.4.3 Microstructure of fracture surfaces of AlMgB_{14} samples with TiB_2 additions, ZrB_2 additions, and HfB_2 additions	63

4.4.4 Densification and mechanical properties of AlMgB ₁₄ samples with additions of ZrB ₂ and HfB ₂	65
4.5 Conclusions	68
4.6 Acknowledgements	68
Chapter 5: Reduced-temperature processing and consolidation of ultra-refractory Ta₄HfC₅	69
5.1 Abstract	69
5.2 Introduction	70
5.3 Experimental	73
5.3.1 Preparation of the starting powders	73
5.3.2 Consolidation	74
5.3.3 Analysis	74
5.4 Results and discussion	74
5.4.1 Powder Characterization	74
5.4.2 XRD, densification, microstructure, and hardness	78
5.4.3 Addition of 30% and 50% WC to Ta ₄ HfC ₅	86
5.5 Conclusions	90
5.6 Acknowledgements	90
Chapter 6: Conclusions	92
6.1 General conclusions	92
6.2 Future work	93
6.2.1 Ta ₄ HfC ₅ Nano structure	94
6.2.2 Ta ₄ HfC ₅ coating	97
6.2.3 WB ₄ and TaB ₄ formation and coating	99
Acknowledgements	101

Appendix: Standard Deviation for Calculated Hardness and Densities	102
References	105

Abstract

Carbides, nitrides, and borides ceramics are of interest for many applications because of their high melting temperatures and good mechanical properties. Wear-resistant coatings are among the most important applications for these materials. Materials with high wear resistance and high melting temperatures have the potential to produce coatings that resist degradation when subjected to high temperatures and high contact stresses.

Among the carbides, Al_4SiC_4 is a low density (3.03 g/cm^3), high melting temperature ($>2000^\circ\text{C}$) compound, characterized by superior oxidation resistance, and high compressive strength. These desirable properties motivated this investigation to (1) obtain high-density Al_4SiC_4 at lower sintering temperatures by hot pressing, and (2) to enhance its mechanical properties by adding WC and TiC to the Al_4SiC_4 .

Also among the carbides, tantalum carbide and hafnium carbide have outstanding hardness; high melting points (3880°C and 3890°C respectively); good resistance to chemical attack, thermal shock, and oxidation; and excellent electronic conductivity. Tantalum hafnium carbide (Ta_4HfC_5) is a 4-to-1 ratio of TaC to HfC with an extremely high melting point of 4215 K (3942°C), which is the highest melting point of all currently known compounds. Due to the properties of these carbides, they are considered candidates for extremely high-temperature applications such as rocket nozzles and scramjet components, where the operating temperatures can exceed 3000°C .

Sintering bulk components comprised of these carbides is difficult, since sintering typically occurs above 50% of the melting point. Thus, Ta_4HfC_5 is difficult to sinter in

conventional furnaces or hot presses; furnaces designed for very high temperatures are expensive to purchase and operate.

Our research attempted to sinter Ta_4HfC_5 in a hot press at relatively low temperature by reducing powder particle size and optimizing the powder-handling atmosphere, milling conditions, sintering temperature, and hot-pressing pressure. Also, WC additions to Ta_4HfC_5 were found to improve densification and increase microhardness. The ability to process these materials at relatively low temperature would save energy and reduce cost.

Boron-based hard materials are used in numerous applications such as industrial machining, armor plating, and wear-resistant coatings. It was often thought that in addition to strong bonding, super-hard materials must also possess simple crystallographic unit cells with high symmetry and a minimum number of crystal defects (e.g., diamond and cubic boron nitride (cBN)). However, one ternary boride, AlMgB_{14} , deviates from this paradigm; AlMgB_{14} has a large, orthorhombic unit cell (oI64) with multiple icosahedral boron units. TiB_2 has been shown to be an effective reinforcing phase in AlMgB_{14} , raising hardness, wear resistance, and corrosion resistance. Thus, it was thought that adding other, similar phases (i.e., ZrB_2 and HfB_2) to AlMgB_{14} could lead to useful improvements in properties vis-à-vis pure AlMgB_{14} . Group IV metal diborides (XB_2 , where $\text{X} = \text{Ti}, \text{Zr}, \text{or Hf}$) are hard, ultra-high temperature ceramics. These compounds have a primitive hexagonal crystal structure (hP3) with planes of graphite-like boride rings above and below planes of metal atoms. Unlike graphite, there is strong bonding between the planes, resulting in high hardness. For this study two-phase

composites of 60 vol. % metal diborides with 40 vol. % AlMgB_{14} were produced and characterized.

Chapter 1: Introduction

1.1 Aluminum Silicon Carbide (Al_4SiC_4)

Al_4SiC_4 is a low-density (3.03 g/cm^3), high-melting temperature ($>2000^\circ\text{C}$) compound, characterized by superior oxidation resistance and high compressive strength [1–5]. These desirable properties motivated several investigators to determine the material's high-temperature strength, thermal conductivity, temperature dependence of linear thermal expansion coefficient, heat capacity from 5.26 to 1047 K, temperature dependence of electrical resistivity, and equation of state [3, 6–9]. Additional work has been performed on the synthesis, densification, microstructure, and mechanical properties of Al_4SiC_4 [5, 10–16]. Some work has also been performed on the effects of C, AlN, and SiC additions to Al_4SiC_4 [17, 18].

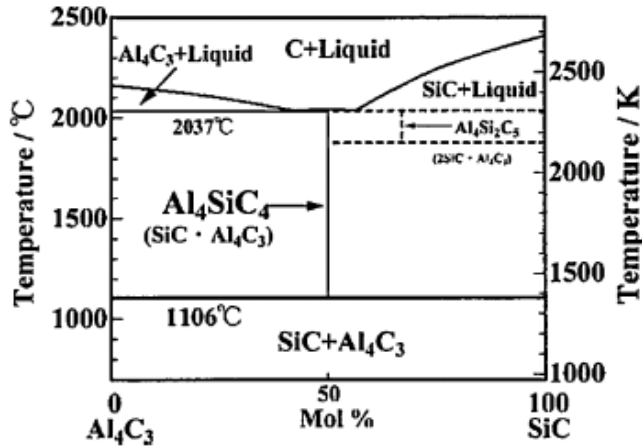


Fig. 1 The equilibrium phase diagram for the SiC- Al_4C_3 system [14]

In all earlier work reported on Al_4SiC_4 , the sintering temperature was above 1600°C , and many of these trials involved other phases mixed with the Al_4SiC_4 . In this study, we attempted to obtain high-density Al_4SiC_4 at lower sintering temperatures by hot pressing and by adding two different materials, WC and TiC, to the Al_4SiC_4 [19].

1.2 Tantalum Hafnium Carbide (4TaC-HfC)

1.2.1 Tantalum Carbide (TaC).

As Fig. 2 shows, single-phase, cubic TaC_y is stable over a large range of C/Ta ratios ($0.74 < y < 1$). TaC_y can accommodate carbon deficiencies from near 0% up to 20%, without changing the crystal structure [20, 21].

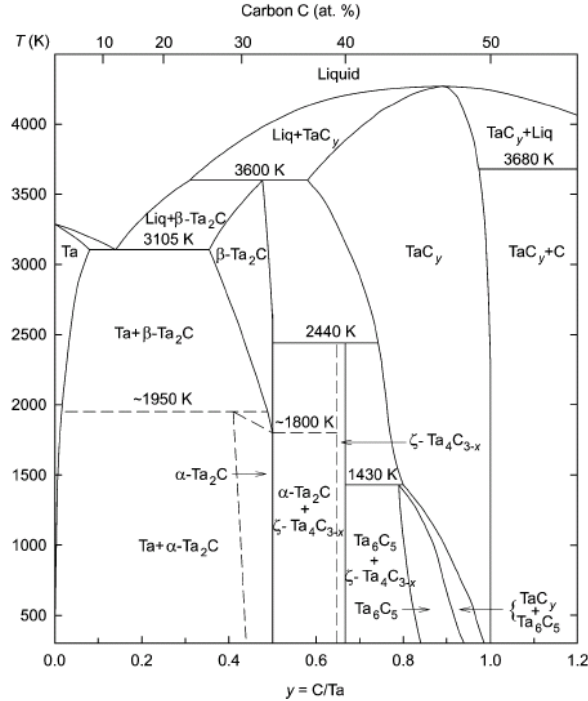


Fig. 2 Ta-C binary equilibrium phase diagram [20]

Tantalum carbide has the NaCl-type structure (B1, space group $Fm\bar{3}m$) where the carbon atoms are located inside the octahedral interstitial sites. TaC has an exceptionally high melting point of 3880°C [22-25].

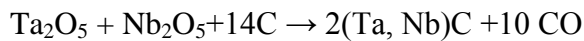
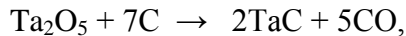
Other investigators have shown that TaC has metal-like conducting properties (e.g., electrical resistivity = 42.1 $\mu\Omega\text{cm}$ at 25°C). As its composition deviates from $y=1$ stoichiometry, the electrical conductivity of TaC_y rapidly decreases. This is due to weakening of the electron-phonon interaction parameter and also a decrease in the density of electron states at the Fermi level. Also, the energy bands and density of states indicate a metallic-like behavior of TaC, showing its potential utility as a high-melting-point electrical conductor. It is worth noting that overall mapping of Fermi surfaces in TaC is contributed from a limited number of bands. The electronic structure of TaC could be attributed to strong interaction between Ta 5d and C states. TaC's heat capacity (C_p) values decrease as the carbon concentration decreases [26, 27]. The monocarbide TaC shows good oxidation behavior. When TaC is non-stoichiometric, the vacant sites can be occupied by oxygen atoms but limited numbers of such sites are available if the TaC is almost stoichiometric (e.g., $\text{TaC}_{0.99}$). The resistance to chemical attack and oxidation can be attributed to the presence of strong covalent-metallic bonding [28].

TaC is the most metallic of the IV and V transition metal monocarbides. Its properties include high strength, high hardness (between 11 to 26 GPa), wear resistance, fracture toughness ($K_{IC} \approx 12.7\text{MPa}\cdot\text{m}^{1/2}$), resistance to chemical attack, and high modulus (537GPa). It is reported to exhibit a ductile-to-brittle transition in the temperature range

1750-2000°C that allows it to be shaped above the DBTT. Ductility of 33% has been reported at 2160°C [29-32].

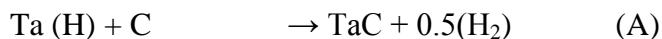
TaC's high melting point (3880°C), high hardness (up to 25GPa), high elastic modulus (up to 550 GPa), low electrical resistivity (42.1 $\mu\Omega$ -cm at 25°C), good chemical stability, good corrosion resistance, durability, high-temperature strength, high temperature erosion resistance, and oxidation resistance suggest that this material could be used in tool steels, wear-resistant parts, diffusion barriers, hypersonic vehicles (leading edges and nose-caps), propulsion components (rocket nozzles), scramjet components, supersonic re-entry vehicles, hard coatings, conducting films, oxidation-resistant coatings, optical coatings, electrical contacts, and electronic applications [33-40].

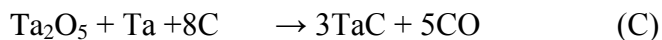
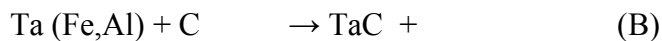
There are different methods to produce TaC powder:



This is the standard production method, starting materials are the oxides either pure or as mixtures. They are mixed with carbon black and reacted in inert atmosphere or vacuum at temperatures between 1400°C and 1800°C.

The following four reactions are less commonly employed and may be used under special conditions:





Method A is applied when the raw material is pure Ta-metal scrap. This brittle compound is milled to a powder and mixed with carbon black. Method B is analogous to A but uses liquid metals such as Fe or Al as the reaction-promoting medium. One problem yet to be economically solved is isolation of the hard materials from the auxiliary metal. Process C is a combination of the standard process and A. Method D is a gas-phase reaction and offers the possibility of producing fine TaC powder [41, 42].

For most materials, sintering occurs above 50% of the melting point, so sintering TaC is difficult, due to its 3880°C melting point. The challenge is made greater still by TaC's low self-diffusion coefficient and its high activation energy for viscous flow. Many investigators have attempted to sinter TaC. Densification of TaC has been studied by hot pressing at temperatures ranging from 1900°C to 2400°C, often with use of additives to decrease the sintering temperature. These additives can lead to a reduction in the sintering temperature but can also lead to grain growth, inability to attain full density, and degraded mechanical properties [43-49].

To inhibit grain growth, rapid sintering of nanostructured TaC hard material was investigated [50]. Rapid sintering by spark plasma sintering was studied, with and without additives [51-53]. It has also been found that high pressure assists densification

and reduces the sintering temperature [54]. Reducing the particle size of the powders was found to improve densification [55]. Also, adding excess carbon can help decrease grain growth and increase density [49].

1.2.2 Hafnium Carbide (HfC)

As Fig. 3 shows, the cubic HfC_x phase is stable with a homogeneity range corresponding to $0.56 \leq x \leq 1.00$. Hafnium carbide has the NaCl-type structure (B1, space group Fm3-m, close packed) where the carbon atoms are located inside the octahedral interstitial sites. Its melting point (3890°C) is the highest among the binary metallic compounds [50-52].

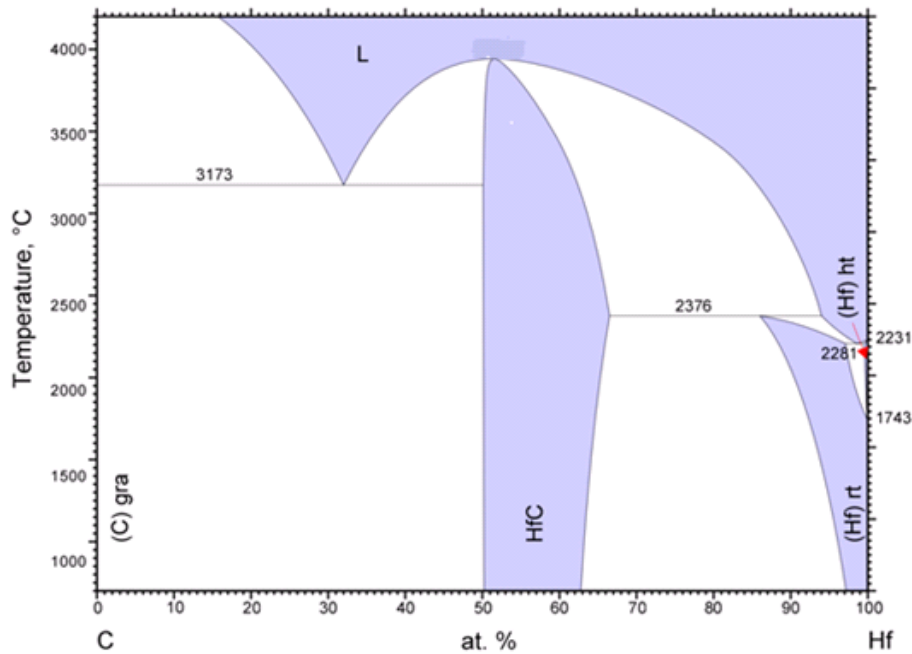


Fig. 3 The Hf-C binary equilibrium phase diagram

Similar to TaC, HfC has excellent chemical stability, high oxidation resistance, high hardness (up to 33 GPa[61]), high electrical and thermal conductivity, and a high Young's modulus (up to 434GPa) [53-62].

HfC is used mainly in aerospace applications due to its high melting point and low diffusion coefficients at high temperatures (thermal protection materials in both re-entry and hypersonic vehicles). It is used in coatings for ultrahigh-temperature environments due to its high hardness, excellent wear resistance, good resistance to corrosion, and low thermal conductivity. It is also used in cutting tools, high-temperature shielding, field emitter tips, and arrays [63-66] HfC has the lowest work function of all transition metal carbides.

As with TaC, HfC is difficult to sinter due to its high melting point and low diffusion coefficient. Many trials have been done using MoSi₂ (hot press and pressure-less) or TaSi₂ as additives to aid sintering or using ultrafine powder to decrease the sintering temperature [67-69].

1.2.3 Tantalum Hafnium Carbide (Ta₄HfC₅)

Transition metal carbides of groups IVB and VB of the Periodic Table that are crystallized in the NaCl-type structure have unlimited solid solutions [M_{1x}M_{21-x}]C_y, where M₁ and M₂ are transition metals [70]. As a result, HfC and TaC form a continuous single-phase cubic (NaCl structure) Ta-Hf-C solid solution (Fig. 4), reported to possess the highest melting temperature among all known materials. Studies of the electronic structure of tantalum hafnium carbide showed the main contribution to chemical bonding

in HfC and TaC results from a very-strong hybridization of the Hf (Ta) 5d- and C 2p-like states [71].

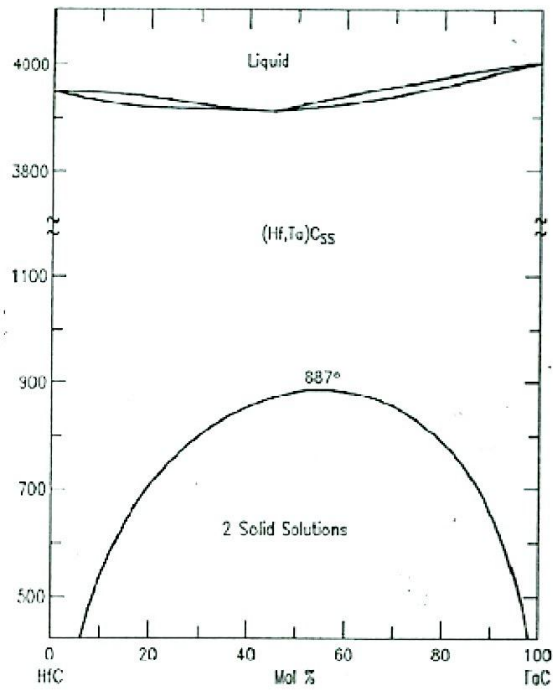


Fig. 4 HfC-TaC phase diagram [72]. Note that this older diagram does not show the melting point elevation now known to occur at the 80 mol. % TaC composition.

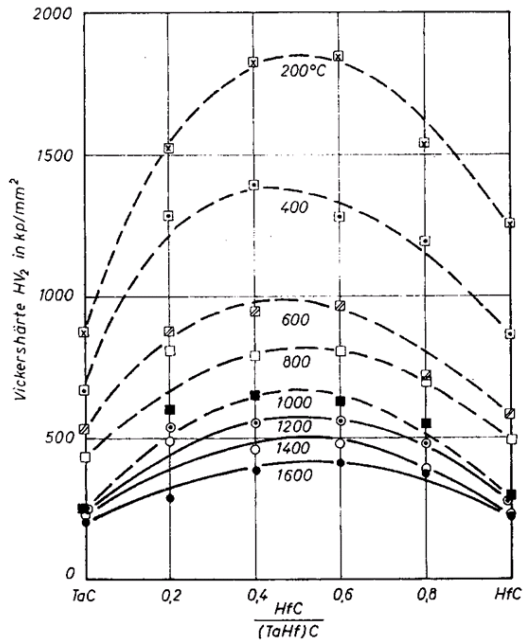


Fig.5 Hardness of HfC/(TaHf)C at different temperatures [76].

The phase diagram of the Ta-Hf-C system exhibits complete miscibility within a broad temperature region above 1200 K. At lower temperatures, the decomposition of the solid solutions is thermodynamically favored, and an immiscibility region appears [72]. Since such decompositions would occur at low fractions of the melting temperature, the reaction kinetics may be so slow as to make the solid solution metastable, at least for reasonable time scales.

Agte, et al reported that the melting point of 4TaC-HfC is 4215K, which is higher than that of either pure TaC or HfC [73], and the finding was subsequently confirmed by Andrievskii [74]. Also, the high-temperature hardness of $(\text{Ta}_{0.8}\text{Hf}_{0.2})\text{C}_{1+x}$ exceeds that of both pure-metal carbides TaC_{1-x} and HfC_{1+x} as shown in Figure 5. [75, 76].

Due to its extreme melting point and high hardness, one of the primary expected applications for Ta_4HfC_5 is in aerospace components such as composite rocket thrusters [77, 78].

Due to the extremely refractory nature of tantalum hafnium carbide, it is a difficult material to consolidate, and reports on its properties are limited. With starting powder of 1.5 μm average particle diameter, Fisher achieved full densification of 4TaC-HfC at 2538°C with an applied pressure of 48 MPa and 15 minute holding time [79]. This shows the difficulty of sintering 4TaC-HfC , a challenge shared by all the high-melting materials.

1.3 Tungsten Tetraboride (WB_4), and Tantalum Tetraboride (TaB_4)

The unique properties of boron allow it to form compounds with metals (M) over an unusually wide range of stoichiometries: M_2B , MB , MB_2 , MB_4 , MB_6 and MB_{12} . For the higher borides (MB_2 - MB_{12}), various 2D- and 3D-like sublattices of strong covalently-bonded boron atoms are formed that often have high hardness. New boron-rich materials with a WB_4 -like structure (hexagonal with $\text{P6}_3/\text{mmc}$ space group) have been predicted to be potentially super-hard materials. These materials include WB_4 , TaB_4 , ReB_4 , TcB_4 , OsB_4 , and MoB_4 . Most of these tetraborides do not appear on phase diagrams, thus they are not equilibrium compounds. These tetraborides have a WB_4 -like structure (Fig. 6) with additional B_2 dimers aligned along the c-axis included between boron sheets. Most data about this group of materials have come from computational work, with hardness values predicted at 41.1, 46.7, and 54.4 GPa for WB_4 , TaB_4 , and ReB_4 respectively. These values look promising for many applications such as hard coatings [80-83].

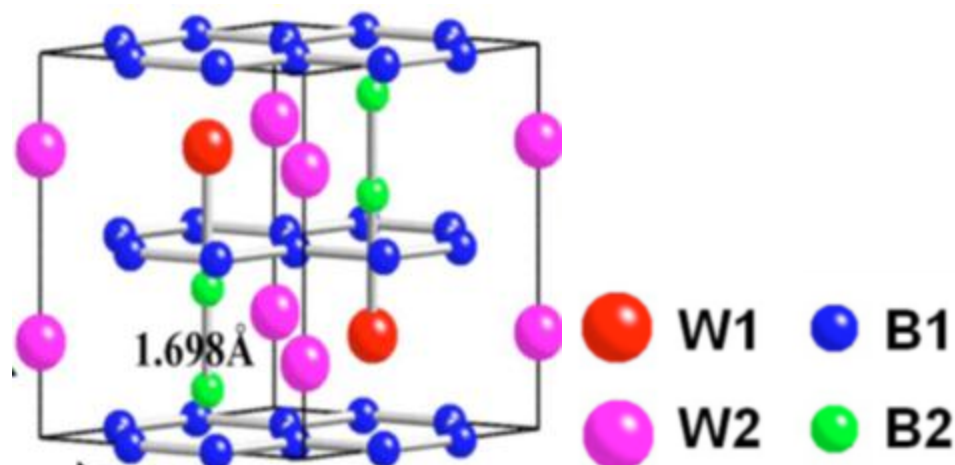


Fig. 6 Crystal structure of WB_4 , This is a hexagonal structure, space group $P63/mmc$ with $a=5.195 \text{ \AA}$ and $c=6.332 \text{ \AA}$. There are four formula units per cell with four inequivalent crystallographic sites, labeled as W1, W2, B1, and B2).

1.4 Aluminum magnesium boride ($AlMgB_{14}$)

1.4.1 Structure

$AlMgB_{14}$ was discovered by Matkovich in 1969, who made the initial report on its crystal structure [84]. Several years later Higashi and Ito made a more accurate determination of crystal structure using more advanced techniques [85]. The $AlMgB_{14}$ structure is $oI64$, an orthorhombic unit cell with 64 atoms. The lattice parameters for the unit cell are $a = 10.313 \text{ \AA}$, $b = 8.115 \text{ \AA}$, and $c = 5.848 \text{ \AA}$. The unit cell contains 56 boron atoms, 4 aluminum atoms, and 4 magnesium atoms. The 56 boron atoms divided into four icosahedral B_{12} units where their centers lie at the $(0,0,0)$, $(0, \frac{1}{2}, \frac{1}{2})$, $(\frac{1}{2}, 0, 0)$, and $(\frac{1}{2}, \frac{1}{2}, \frac{1}{2})$

positions. This accounts for 48 atoms, and the remaining atoms bond the icosahedra together and occupy an eight-fold position at $(0.152, 0.622, 0)$ [84]. Matkovich determined that the magnesium atoms are located at a fourfold location of $(\frac{1}{4}, 0.359, 0)$. The aluminum atoms are located at a fourfold location at $(\frac{1}{4}, \frac{3}{4}, \frac{1}{4})$. Later, Higashi determined that aluminum site occupancy is just 75%, while magnesium sites occupancy is 78%, which gives a composition of $\text{Al}_{0.75}\text{Mg}_{0.78}\text{B}_{14}$. Figure 7 shows a modeled unit cell of the AlMgB_{14} compound as drawn by Harmon in 1999 [87].

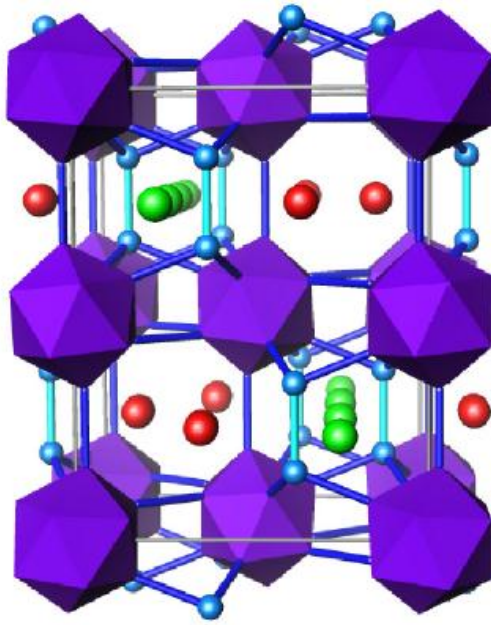


Figure 7: Schematic crystal structure of AlMgB_{14} unit cell

1.4.2 Synthesis

Matkovich and Higashi studied AlMgB_{14} single crystals [84, 85]. For Matkovich; the single crystal was grown by heating at 900°C a mixture of aluminum, magnesium, and boron in an atomic ratio of 14:1:2. Aluminum was used as a flux material, and the excess

Al was removed by dissolving in hydrochloric acid. The excess of magnesium was used due to substantial magnesium loss at 900°C (melting point is 1091°C [86]). Similar to Matkovich's process, Higashi used an atomic ratio of 31:1:6 for aluminum, magnesium, and boron respectively at 1500°C under an inert atmosphere. The excess of magnesium was used due to its volatility at 1500°C. In both processes, other compounds such as AlB_{12} were also produced [87].

More recent attempts to produce AlMgB_{14} used a mixture of fine commercially purchased powders of aluminum, magnesium, and boron, which were then hot pressed at 1400°C or 1500°C. This process resulted in low yields of AlMgB_{14} . A higher yield of AlMgB_{14} resulted when mechanical alloying was used prior to hot pressing. Hot pressing mechanically alloyed powders at 1400°C, with a pressure of 106 MPa, has been shown to produce almost 100% dense compacts of AlMgB_{14} [88].

1.4.3 Mechanical Properties

Although AlMgB_{14} was first synthesized in 1969, little research was performed on its mechanical properties prior to 1993 when Higashi, et al reported single crystal hardness around 30 GPa [89]. Cook, et al reported a hardness of 46 GPa for AlMgB_{14} - 30 wt. % TiB_2 composite [90], which revived the interest of the scientific community in this material. Table 1 compares the hardness of AlMgB_{14} to other commercially available hard materials.

Table 1: Some hard materials and selected properties of those materials [87]

Material	Density (g/cm ³)	Hardness (GPa)	Crystal Structure
C (Diamond)	3.52	70	Cubic
BN _(Cubic)	3.48	45-50	Cubic
AlMgB ₁₄ +TiB ₂	3.14	30-46	Orthorhombic + Tetragonal
B ₄ C	2.52	38-44	Rhombohedral
AlMgB ₁₄	2.66	25-35	Orthorhombic
TiB ₂	4.50	30-33	Tetragonal
WC	15.77	23-30	Hexagonal
Al ₂ O ₃	3.98	21-22	Hexagonal
Si ₃ N ₄	3.44	17-21	Amorphous

Peters, et al showed that small amounts of iron and/or oxygen affect the hardness and the other properties of AlMgB₁₄ [91]. The iron mainly forms FeB and Fe₃O₄ when reacting with the other elements in the material. Oxygen forms Al₂MgO₄. All three of these phases are softer than the AlMgB₁₄ phase [88]. The Al₂MgO₄, FeB, and Fe₃O₄ showed hardnesses of 13.7, 11.8, and 14.7 GPa respectively. These comparatively low hardness values decrease the overall hardness of the material [92].

The thermal expansion of AlMgB₁₄ is important, especially if it is used as a coating material. It is well known that a big difference in thermal expansion between the coating material and the substrate generates internal stresses during heating or cooling [93].

Lewis, et al [87] showed that, AlMgB₁₄ has an average thermal expansion coefficient value of $8.22 \times 10^{-6} \text{K}^{-1}$. This value is much higher than that for diamond-like carbon ($0.7 \times 10^{-6} \text{K}^{-1}$), fairly close to that of steel ($11.8 \times 10^{-6} \text{K}^{-1}$), and nearer still to that of titanium ($8.6 \times 10^{-6} \text{K}^{-1}$) [94].

Also, AlMgB_{14} has a low erosion rate; Peters showed that when mechanically alloyed AlMgB_{14} was hot pressed at 1500°C , it has an erosion rate of $0.67 \text{ mm}^3/\text{kg}$ of erodent powder. Peters also showed that, AlMgB_{14} displays plane strain fracture toughness (K_{IC} , $\text{MPa}\sqrt{\text{m}}$) of $2.7K_{\text{IC}}$ and Young's modulus (E) of 510 GPa [95].

AlMgB_{14} is a candidate for use as a hard, wear-resistant coating. Also, it can be used in cutting, grinding, and machining. It is also a potential candidate as a low-friction material or as a semiconductor material [96, 97].

1.5 Mechanical Alloying

It is well known that the structure and composition of advanced materials can often be better controlled by processing them under non-equilibrium conditions [98]. Mechanical alloying is one such process that has received attention from researchers [99]. Mechanical alloying is a solid-state powder processing technique that imposes repeated welding, fracturing, and re-welding of powder particles in a high-energy ball mill to produce homogeneous materials starting from blended elemental powder mixtures. It is also used to reduce powder particle sizes. When a mixture of powders is milled and material transfer takes place, this is true mechanical alloying. When there is no material transfer, such as in milling pure powder to reduce particle size, it is no longer mechanical alloying, but rather mechanical milling. Because mechanical milling is mainly used to reduce particle size, it needs shorter milling times, and so causes less contamination from milling wear debris [100]. Mechanical alloying has the ability to synthesize a variety of equilibrium and non-equilibrium phases such as supersaturated solid solutions,

metastable crystalline and quasicrystalline phases, nanostructures, and amorphous alloys [101]. Benjamin developed this process in the mid-1960's to produce oxide-dispersion strengthened nickel- and iron-base super alloys [102-104]. Mechanical alloying has seen many uses since Benjamin's early work to produce such materials as Y-Co intermetallic compound and non-equilibrium Ni-Nb structures [105].

1.5.1 The process of mechanical alloying

The process of mechanical alloying starts with mixing of the powders in the right percentage. The mixed powders are then loaded into the mill along with the grinding media. The mixed powder is then milled for the desired length of time until a steady state is reached when the composition of every powder particle is the same as the percentage of the elements in the starting powder mix. Raw materials, mill, and process variables are the most important variables for mechanical alloying.

1.5.2 Raw materials

Typically, raw materials are commercially available as pure metals, master alloys, or pre-alloyed powders with particle sizes ranging from 1 to 200 μm . Although the particle size is not critical due to the exponential decrease in size with time, the starting powder size should be smaller than the grinding ball size. After milling for only few minutes, the powder size can reach a few microns. In the early days of mechanical alloying, the powder load consisted of at least 15 vol. % of a ductile metal powder to be used as a binder. Nowadays, mixtures of fully brittle materials are successfully milled resulting in alloy formation [106].

1.5.3 Types of mills

There are different types of high-energy mills that are used to form mechanically alloyed powders. These mills differ in their capacity, efficiency of milling, the amount of wear debris accumulated, and other factors.

1.5.3.1 SPEX shaker mills

The most common shaker mill for laboratory use is the SPEX mill, a vial containing the powder and grinding balls that is violently shaken in an eccentrically agitated structural frame. A SPEX mill can mill about 10 to 20 grams of powder per load. The vial is secured by a clamp that holds it firmly in the shaker frame, which oscillates the vial thousands of times per minute. During oscillation, the vial traces the path of a figure-8 due to the combination of back and forth motion combined with lateral motion of the vial ends. Vial materials are available that are made of several different materials, including tungsten carbide, chrome steel, zirconia, and alumina. The SPEX mill is considered a high-energy mill; during vibration of the vial, the balls impact both the powder and the vial ends that mill and mix the powder. The amplitude of oscillation (around 5 cm) and the speed of motion (around 1200 rpm), generates mill ball velocities as high as 300 meters per minute, which produces high impact energy for the balls' collisions with the vial walls and powder. Recently, different versions of SPEX mills have appeared that include two vials to increase productivity. Some units provide cooling time to extend the milling time. Most research on mechanical alloying has been done using SPEX mills.

1.5.3.2 Planetary ball mills

Another popular mill is the planetary ball mill, which allows more powder to be milled in each load (hundreds of grams). It is named planetary due to the planet-like orbital movement of the vials. The vials rotate around their own axes, producing centrifugal force that grinds the powders. Different materials for vials and balls are available such as zirconia, chrome steel, and tungsten carbide. Although the linear velocity of the balls in planetary mills is higher than in SPEX mills, the planetary mill is considered to be a lower energy mill due to the lower frequency of impacts compared to SPEX mills.

1.5.3.3 Attritor mills

The attritor mills are conventional ball mills that can mill a large quantity of powder (up to kilograms of powders at a time). This provides faster comminution throughput than other ball mills. It consists of a vertical drum with a number of impellers inside that energize the ball charge, causing powder size reduction. Attritors are available in different capacities and sizes. If compared to the SPEX mill, the attritor is a low-energy mill because the grinding medium velocity is lower (30 m/minute). A variety of materials for grinding containers and grinding media are available in attritor mills such as silicon nitride and zirconia. During attritor milling the tank with the grinding media contains the powder, while a high-speed rotating shaft with arms agitates the powder and the grinding media. This action imposes both impact and shearing forces on the powder. There are different attritor mills for various specific purposes such as vibrating frame mills and rod mills. The commercial mills are available in much larger sizes than SPEX mills; the

largest attritor mills can mill hundreds of kilograms of powder in one load. It is well known that the higher the energy of the mill, the shorter the time needed to achieve the desired degree of alloying and comminution. The process that takes a few days in a commercial mill can take hours in an attritor and a few minutes in the SPEX mill. It has been reported that 20 hours milling in a low energy mill is equivalent to just 20 minutes of milling time in a SPEX mill [107].

1.5.4 Process variables

Mechanical alloying has different process variables that can be adjusted to obtain the required constitution. The most important of these are: type of mill, milling container composition and size, milling speed, milling time, type, size, and size distribution of the grinding media, ball-to-powder weight ratio, extent of filling the vial, milling atmosphere, process control agent, and milling temperature. Most of these variables are interdependent. For example, the milling time depends on the type of mill and the ball-to-powder weight ratio.

1.5.4.1 Type of mill

Since different types of mills have greatly differing capacities, speeds, etc., the best mill will vary with the particular milling task at hand. For example, milling large quantities of powder suggests use of attritors (e.g., Zoz mill) or a planetary ball mill (e.g., Fritsch Pulverisette). For alloy screening studies and basic research, the SPEX mill is often preferable since it can reach a given degree of comminution so much more rapidly.

1.5.4.2 Milling container

The milling container material is important due to the possibility of powder contamination from wear debris resulting from media impact on the walls of the container. The most common materials used for milling containers are tungsten carbide, chromium steel, and tool steel [108]. Also, the internal design of the vials seems to be important; alloying was found to be done at higher rates when using flat-ended vials compared to round-ended vials [109].

1.5.4.3 Milling speed

The familiar relation $E = 0.5mv^2$ indicates that the higher the milling speed, the greater the energy transferred into the powder. However, there are limitations on milling speed. For example, above a certain critical speed, the balls will stick to the vial walls, which drop collision energy to zero. Also, the higher the speed of milling, the higher the temperature of the vials; which increases the probability of powder contamination.

1.5.4.4 Milling time

Milling time is the most important factor in milling. Since milling causes powder particle welding, fracturing, and re-welding, the milling time is usually chosen to be the minimum time necessary for the powder to achieve a steady-state balance between powder fracturing and welding. As previously described, the milling time needed to achieve this steady-state condition depends on many parameters, such as mill type, the ball-to-powder mass ratio, the speed of milling, and milling temperature. So for every milling task, there

is an optimum milling time dependent on the combination of all these parameters. In all cases, the milling time should not exceed the required milling time in order to minimize contamination from wear debris [110].

1.5.4.5 Grinding medium

The most common types of grinding media are tungsten carbide, hardened chromium steel, and stainless steel. Some precautions can be taken for milling such as ball densities, ball material, and ball diameter. Higher impact forces on the powder result from denser and larger media balls. In an ideal case, the balls and the vials would have the same material composition as the powder, but, of course, this is not usually possible. To have the highest possible collision energy and to minimize the amount of powder coated onto the vial walls and ball surfaces, use of two different sizes of balls has been shown to be effective [111, 112].

1.5.4.6 Ball-to-powder weight ratio (BPR)

The ball-to-powder-weight ratio (BPR) affects the time required to obtain the desired phase or size. The higher the BPR, the shorter the milling time required. Usually, low BPR ratio and low speed of rotation favor formation of metastable phases, while high BPR ratio and high speed of rotation favor formation of equilibrium phases [113, 114].

High BPR ratios deliver more energy to the powders and speed mechanical alloying. The most common ratio for the SPEX mill is 10:1 while large-capacity mills are sometimes run with BPR values as high as 200:1 [115, 116].

1.5.4.7 Extent of filling the vial

Open space is needed in a vial for the balls to impact the powders freely; thus, the extent to which the vial is filled is an important factor. A balance must be struck when filling the vial; too many balls and too much powder will not give enough space for the balls to impact the powder with high energy. If too little space in the vial is filled with balls and powder, productivity drops. Fifty percent balls and powder and fifty percent free space is often a good compromise between these factors.

1.5.4.8 Milling atmosphere

The milling atmosphere has a profound effect on the amount of powder contamination and/or oxidation. For this reason powders for research are mainly milled in evacuated vials or in vials back-filled with inert gas. The main inert gases used are argon or helium, but nitrogen can be used when producing nitrides, and hydrogen can be used when producing hydrides [117, 118]. To minimize contamination, all handling, loading, and unloading of powders into vials should take place in atmospherically controlled glove boxes that are repeatedly evacuated and refilled with an inert gas.

Chapter 2: General Experimental Procedures

2.1 Preparation of the starting powders

The majority of the samples examined in this study were prepared through high-energy milling of powders followed by uniaxial hot-pressing into dense compacts. Most starting materials were commercially prepared by Aesar with purities greater than 99.5%.

The powders were handled in a He-filled glove box and weighed to achieve the proper stoichiometric atomic ratio. The powders were then loaded in small, hardened steel vials with a sealed lid along with three 8-gram and three 1-gram Cr-steel milling media. The small size of the vials limits samples to only a few grams. Milling was done mainly in high-energy Spex 8000 vibratory/oscillatory mills for different times. The sealed vials were returned to the glove box after milling to recover the milled powder. Some material was lost to agglomeration against the walls of the vials, and only powder that could be scraped away easily was recovered. The powder was then ready for hot pressing to produce compacts or for subsequent processing to add second phase materials.

A second milling is usually used to add reinforcement phases to produce a composite. The second phases were loaded into a clean vial along with the first phase as in the previous step. Most of the second millings were done for only 30 minutes to reduce wear and contamination caused by the hard additive; the primary purpose of the second milling step is to break down agglomerates and ensure even mixing. The second milling was not intended to induce any mechanical alloying. The milled powder was then loaded into a graphite die for hot pressing.

Graphite dies with a bore diameter slightly larger than one-half inch were prepared by coating their interiors with a thin layer of boron nitride to lubricate and protect the dies. Half-inch diameter push rods were also coated with boron nitride. The die components' internal surfaces were then lined with a flexible graphite sheet material for additional protection. Powder was loaded into a die within the glove box, and the upper push rod was inserted before the whole die assembly was transferred to the pressing chamber in a closed clear bag as quickly as possible to minimize contact with room air. The pressing chamber was then evacuated immediately, and high vacuum was achieved with a diffusion pump.

2.2 Consolidation

Powder consolidation was performed in a 75-ton Centorr hot press using graphite dies under a flowing argon atmosphere. All samples were pressed for 60 min at a pressure of 106 MPa. All samples were 0.5" diameter. The pressure used was measured using the following equation: $P_{\text{sample}} = (33.1126) P_{\text{digital gauge}}$, where P is expressed in p.s.i. Most of the samples were pressed at 1500 °C, although some were pressed at lower temperatures.

After hot pressing, the compacts were removed from the dies and cleaned by sand blasting. Usually, dense compacts were produced, and these were metallographically polished on at least one surface prior to subsequent analysis.

2.3 Evaluation

Since the resulting samples are hard, polishing requires much more time and effort than normal metallographic polishing operations; diamond is the only effective abrasive. So a high-speed diamond grinder was used first to produce flat, parallel faces. When at least one flat surface was produced, the samples were mounted in Buehler Epoxicure resin; where the ratio of resin to hardener is 5 to 1 with a total of 10 gram.

The polishing steps involve grinding with a combination of a metal-bonded 45- μm diamond pad and a 45- μm diamond paste to increase material removal rates. This was followed by use of 9- and then 6- μm diamond suspensions on discontinuous pads to again improve removal rates. A 3- μm diamond suspension on felt was used next, and the final step was vibratory polishing of the samples under a submersion of colloidal silica. The majority of material removal in the final step is by etching, and differential erosion rates of the various phases can result in a slightly uneven surface. Polished samples were then ready for scanning electron microscopy (SEM), hardness testing, XRD analysis, etc.

Standard measurements were made on these materials to determine their microhardness, toughness, wear, and density. X-ray diffraction (XRD) was used to identify the formation of the phases and to identify unknown impurities and reaction products in all specimens. The hot-pressed microstructures were analyzed by SEM and energy dispersive spectroscopy (EDS). SEM was frequently used to analyze the microstructure because the majority of the materials contained sub-micron grains.

Density was determined by the Archimedes displacement method (according to MPIF Standards 42, 1998); the sintered specimen was weighed in air, and the sample was then lowered into water to measure its weight in water. To convert the measured masses to density, one divides the mass in air by that in water (equal to the volume displaced by the water). Then the relative density of the sintered materials was calculated according to the following formula: Relative density (ρ) % = ρ_s / ρ_t where ρ_s is the sintered density (actual density), and ρ_t the theoretical density respectively.

Hardness measurements were performed with a Wilson-Tukon 2100B model microhardness tester using a Vickers indenter equipped with CCD image enhancement capability. Hardness was measured at loads of 1000, 2000, or 5000 grams-f. The hardness values of the investigated materials were measured as the average of ten readings along the cross section surface of polished specimens. Toughness was estimated by the Palmqvist technique, which measures average crack length extending from indentation corners, and calculated using:

$$K_{IC} = 0.016 \left(\frac{E}{H} \right)^{1/2} \left(\frac{P}{C^{3/2}} \right)$$

where E is the elastic modulus, H is the Vickers hardness (kg/mm^2), P is the applied load (N), and C is half the average length (μm) of the cracks radiating from the corners of the Vickers indent, from tip to tip. The constant, 0.016, is a materials constant that has been found experimentally for many materials to be approximately 0.016 [1-2].

The erosion test method employed for this work was performed with a Comco, Inc. Microblaster, in accordance with the ASTM G 76 standard. Angular alumina grit (Al_2O_3) with a typical +100 micron size was used as the abrasive material in a stream of dry compressed air or N_2 at an operating pressure of 275 kPa. The abrasive stream struck the sample at a constant rate, and particle velocity was over 100 m/s. The samples were cleaned with ethanol and an ultrasonic bath to remove loosely bonded grit before weighing. The mass of each sample was measured 10 times each at 0, 30, 60, 90, and 120 minutes of total of erosion time. Multiple measurements were averaged to reduce error because the mass loss of a typical sample at each stage was only about 1 mg or less. The mass of erodent used was also weighed at each stage. These values were used to calculate the ratio of sample volume loss to erodent mass consumed. The reported erosion rate corresponds to the steady-state value, which was found to remain constant as testing time varied. The erosive jet was constrained to a diameter much smaller than each sample's diameter, which assured that all erodent impacts occurred on the target. Used grit was collected and never reused.

A variable-pressure JEOL 5910 scanning electron microscope (SEM) was used to study the microstructure of the various samples. Imaging capabilities include secondary and backscattered electron imaging modes, the latter having topographical, compositional, and shadow mode options. The instrument has an accelerating voltage range of 0.5 - 30 kV. It uses a tungsten gun, and it has an ultimate resolution of 4 nm. The lower magnification limit is 18x. It is equipped with a Noran Vantage EDS system with light-

element Si(Li) detector. Software allows for quantitative analysis, line scans, and elemental mapping. The EDS was not used for quantitative compositional analysis because this method is unreliable for light elements such as these boron-rich materials; EDS was used only to identify the elements present.

A PANalytical X-Pert Pro Diffraction System was used to generate XRD patterns using CuK_α radiation. XRD was used to analyze the as-received powders, the powders after mixing and/or different milling times, and the hot-pressed samples. A sample spinner stage was used to detect hot-pressed samples while most powder samples were analyzed with the XCelerator Detector. The diffraction patterns were mainly used to verify phase formation and sometimes indexed to identify the unknown phases. The hot-pressed samples were examined on their polished faces, and it was assumed that the fine microstructure did not produce any preferential orientation.

Chapter 3: Formation, densification, and selected mechanical properties of hot pressed Al_4SiC_4 , Al_4SiC_4 with 30 vol. % WC, and Al_4SiC_4 with 30 vol. % TiC

A paper published in *Ceramics International* Vol. 37(8), pp. 3117-3121 (2011)

Osama Gaballa ^{a,b,c}, Bruce Cook ^b, Alan Russell ^{a,b}

^a Department of Materials Science and Engineering, Iowa State University, Ames, IA 50011, USA

^b Ames Laboratory Division of Materials Science and Engineering, Iowa State University, Ames, IA 50011

^c Central Metallurgical Research and Development Institute, Helwan, Cairo, Egypt

3.1 Abstract

Powders of Al_4C_3 and SiC were combined by high-energy milling to produce Al_4SiC_4 , $\text{Al}_4\text{SiC}_4 + 30$ vol. % TiC, and $\text{Al}_4\text{SiC}_4 + 30$ vol. % WC. Five different temperatures were used to hot press the constituents. XRD, SEM, relative density, and hardness measurements showed that formation of single-phase Al_4SiC_4 occurred at 1450°C and full densification (99%) was achieved at 1500°C. Both of these temperatures are lower than previously reported. Adding TiC and WC increases hardness, while WC improves densification (99.5%).

3.2 Introduction

Al_4SiC_4 is a low-density (3.03 g/cm³), high-melting-temperature (>2000°C) compound, characterized by superior oxidation resistance, and high compressive strength [1–5]. These desirable properties motivated several investigators to determine the material's high-temperature strength, thermal conductivity, temperature dependence of linear thermal expansion coefficient, heat capacity from 5.26 to 1047 K, temperature

dependence of electrical resistivity, and equation of state [3, 6–9]. Additional work has been performed on the synthesis, densification, microstructure, and mechanical properties of Al_4SiC_4 [5, 10–16]. Some work has also been performed on the effects of C, AlN, and SiC additions to Al_4SiC_4 [17, 18].

In all earlier work reported on Al_4SiC_4 , the sintering temperature was above 1600°C , and many of these trials involved other phases mixed with the Al_4SiC_4 . In this study, we attempted to obtain high-density Al_4SiC_4 at lower sintering temperatures by hot pressing and by adding two different materials, WC and TiC, to the Al_4SiC_4 .

3.3 Experimental

3.3.1 Preparation of the starting powders

The Al_4SiC_4 starting powder for this study was prepared by mixing high-purity Al_4C_3 and SiC (99.8% purity) powders in a He-atmosphere. A Spex-8000 mixer/mill was used to comminute the powders in sealed, hardened steel vials with chrome steel milling media. The constituents were milled for 6 h, a milling time found to be suitable in earlier studies on processing $\text{TiB}_2\text{--ZrB}_2$ and TiB_2 [19,20]. For some samples, the mechanically alloyed Al_4SiC_4 powder was then mixed with 30 vol. % TiC or 30 vol. % WC and milled for an additional 30 min. The second-phase additions were 99.5% pure, 1 μm average size for WC and 2 μm for TiC. All powder handling occurred in a He-atmosphere glove box to minimize oxygen contamination.

3.3.2 Consolidation

Powder consolidation was performed in a 75-ton Centorr hot press using graphite dies under a flowing argon atmosphere. All samples were pressed for 60 min at a pressure of 106 MPa. The dies were lined with boron nitride and graphite sheet as lubricants. Al_4SiC_4 samples were pressed at five different temperatures, 1200°C, 1300°C, 1400°C, 1450°C, and 1500°C. $\text{Al}_4\text{SiC}_4 + 30\%$ WC and $\text{Al}_4\text{SiC}_4 + 30\%$ TiC specimens were pressed only at 1500°C (Fig. 1).

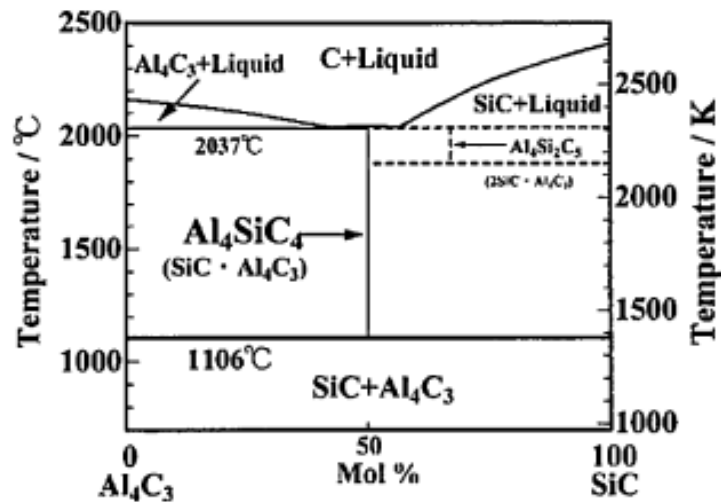


Fig. 1. The phase diagram for SiC–Al₄C₃ system [14]

3.3.3 Evaluation

XRD was used to identify the formation of Al_4SiC_4 phase in all specimens. The hot-pressed microstructures were analyzed by SEM and EDS. Density was determined by the

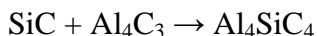
Archimedes displacement method; the sintered specimen was weighed in air, and the sample was then lowered into water to measure its weight in water. Then the relative density of the sintered materials was calculated according to the following formula:

Relative density (D) % = ρ_s/ρ_t where ρ_s is the sintered density (actual density), and ρ_t the theoretical density respectively. Hardness was measured at a load of 2000 g by Vickers microindentation with a Wilson-Tukon 2100B microhardness tester equipped with CCD image enhancement capability. The hardness values of the investigated materials were measured as the average of ten readings along the cross section surface of polished specimens.

3.4 Results and discussion

3.4.1 Formation, densification, and XRD analysis of the samples

Al_4SiC_4 can be obtained from the following reaction [21].



The standard Gibbs energy of formation for this reaction changes from positive to negative at 1106°C. Therefore, formation of the ternary compound is favored at temperatures above 1106°C, as can be seen from the phase diagram for the SiC– Al_4C_3 system. Actually, the detection of Al_4SiC_4 starts at 1200°C so this temperature was used as the first in a series of sintering temperatures [14, 2].

The degree of densification achieved during hot-pressing of powders relates to several variables: powder particle size, powder handling atmosphere, milling conditions,

sintering temperature, and hot pressing pressure. For example, a mixture of particle sizes can improve the fill ratio of a pressed compact.

Also, milling under an inert atmosphere produces surfaces nearly free of oxides, which have high activity and are more readily sintered. High pressure during sintering generally increases densification [22–24].

Fig. 2 shows the XRD patterns of the Al_4SiC_4 sintered samples hot pressed for 1 h at five different temperatures (1200°C, 1300°C, 1400°C, 1450°C, and 1500°C). Fig. 3 shows the XRD patterns for Al_4SiC_4 , $\text{Al}_4\text{SiC}_4 + 30\% \text{ TiC}$, and $\text{Al}_4\text{SiC}_4 + 30\% \text{ WC}$ samples sintered at 1500°C for 1 h.

As shown in Fig. 2, the XRD patterns of the powders sintered at 1200°C and 1300°C clearly show the presence of four phases, SiC, Al_4C_3 , the Al_4SiC_4 reaction product plus Fe from milling wear debris. Prior work on related materials indicates that the Fe content may be less than 1.5% [25], the intensity of the iron peak is strong due to the higher atomic number of the iron compared to the atomic number of the Al_4SiC_4 . At these two temperatures, the two starting powder phases are dominant. At 1400°C, however, the Al_4SiC_4 phase dominates, and at 1450°C, and 1500°C Al_4SiC_4 is the only non-ferrous crystalline phase detected. Taken together, these patterns show that Al_4C_3 and SiC powders can be fully reacted to Al_4SiC_4 by milling 6 h and hot pressing for 1 h at 106 MPa and 1450°C.

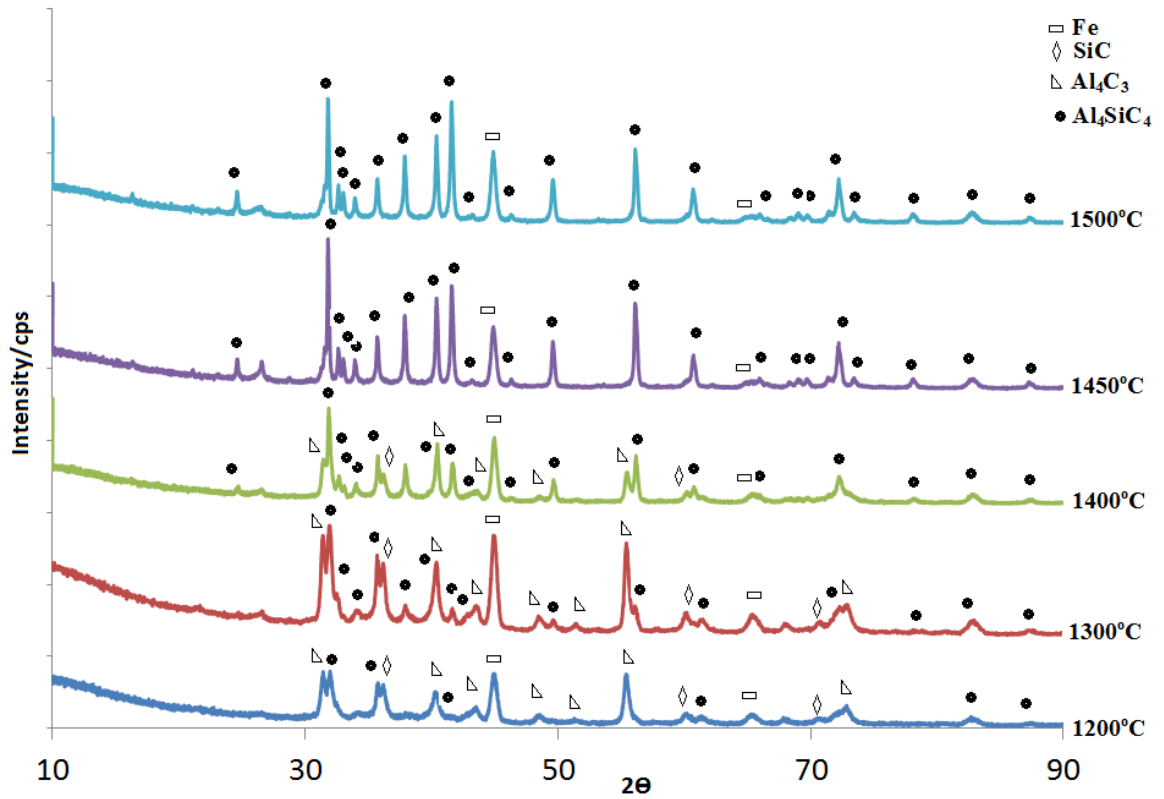


Fig. 2, XRD patterns of the various hot-pressed powders of Al_4SiC_4 at 1200°C, 1300°C, 1400°C, 1450°C, and 1500°C for 1 h in flowing Ar. Fe is present in these samples from wear debris during milling.

The XRD patterns show hexagonal crystal structures for two detected phases of Al_4SiC_4 and WC and a cubic crystal structure for the TiC. As shown in Fig. 3 middle and 3 top, the intensities of Al_4SiC_4 peaks are low relative to those of TiC and WC, presumably due to the large differences in atomic weights of the elements in these three phases. Also, fewer peaks are observed in Fig. 3 middle than in Fig. 3 bottom and 3 top. This could be explained by the negative correlation between the crystal symmetry and the number of peaks. In support of this explanation, the cubic structure, which has the highest symmetry, was found to give rise to the minimum number of peaks [26].

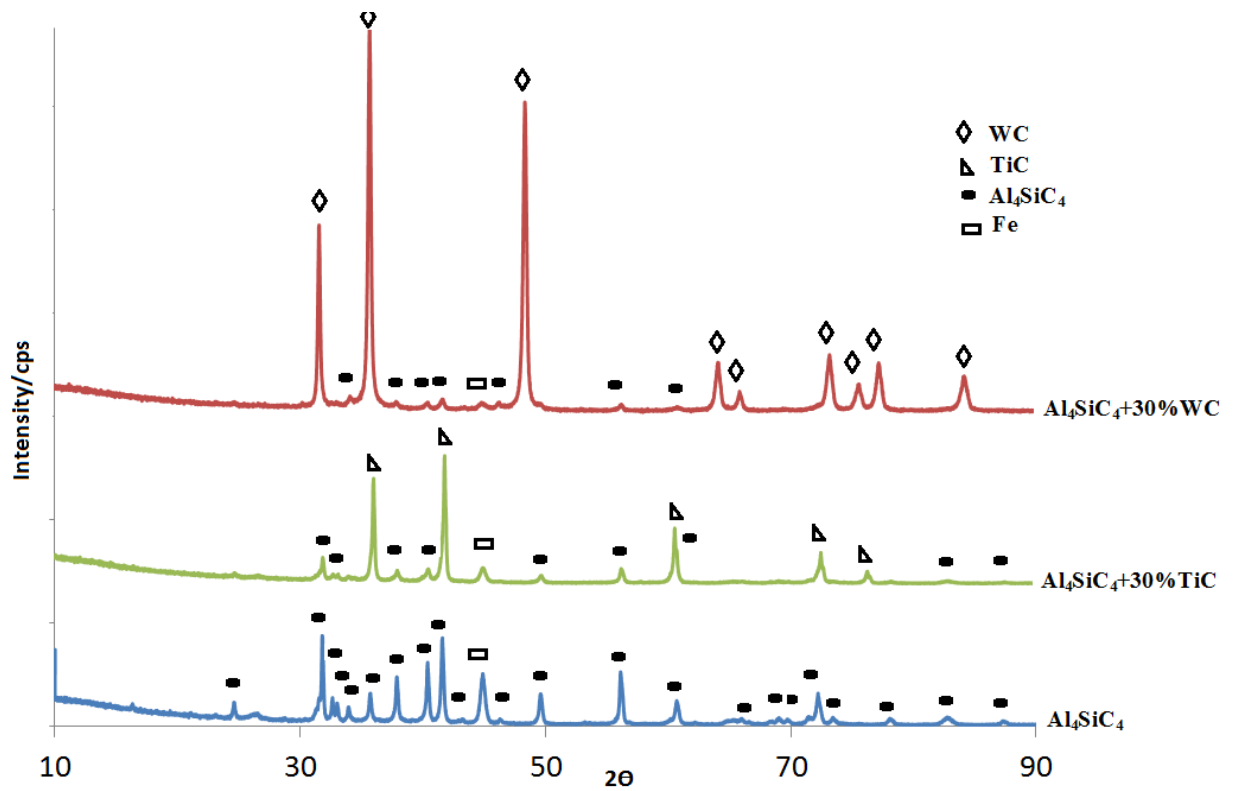


Fig. 3. XRD patterns of Al_4SiC_4 , $\text{Al}_4\text{SiC}_4 + 30\%$, and $\text{Al}_4\text{SiC}_4 + 30\%$ TiC hot pressed at 1500°C for 1 h in flowing Ar.

These results indicate that hot pressing of Al_4C_3 and SiC with TiC or WC milled powders for 1 h under a pressure of 106 MPa at 1500°C is adequate to produce two-phase $\text{Al}_4\text{SiC}_4 + \text{TiC}$ or $\text{Al}_4\text{SiC}_4 + \text{WC}$ with reasonably good phase purity.

3.4.2 Microstructure

Most of the phases were found to be smaller than $1\ \mu\text{m}$, except for WC, where abnormal grain growth was observed (Fig. 4c). This grain growth in the presence of carbon has been noted before but is not totally understood. This may be explained by the presence of

carbon, which could lower the activation energy of two-dimensional nucleation on singular grain boundary surfaces of WC [27]. In contrast, the $\text{Al}_4\text{SiC}_4 + 30\% \text{ TiC}$ showed no abnormal grain growth, which is consistent with previous observations that TiC can prevent grain growth during sintering [23,24].

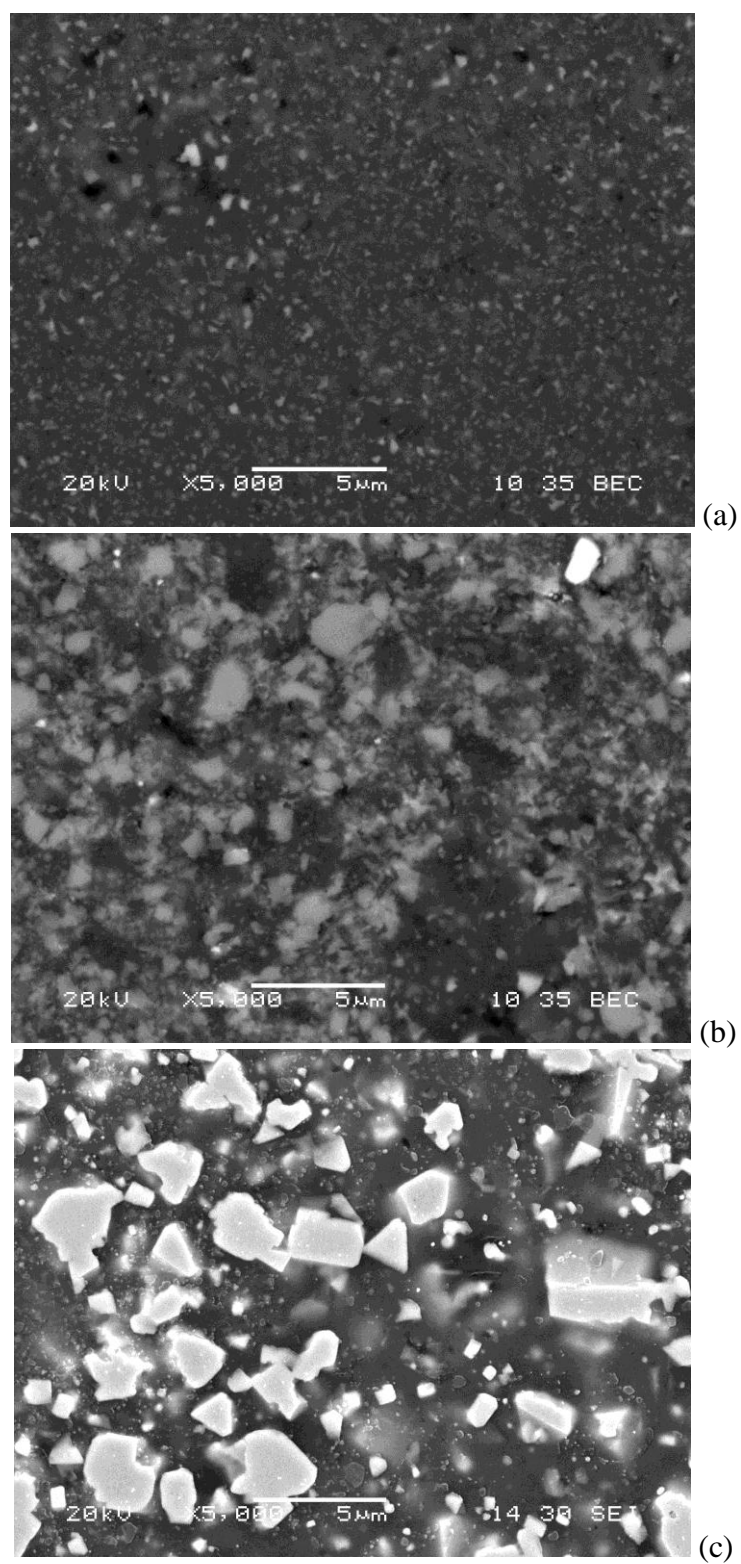


Fig. 4. Back-scattered SEM micrographs of (a) Al_4SiC_4 , and (b) $\text{Al}_4\text{SiC}_4 + \text{TiC}$, and secondary electron micrograph of (c) $\text{Al}_4\text{SiC}_4 + \text{WC}$.

3.4.3 Mechanical properties

Relative density

We found that the relative densities of hot-pressed Al_4SiC_4 were significantly increased as temperature increased and reached nearly full densification at 1500°C (Fig. 5). The high relative density percentages are thought to result mainly from rearrangement of grains, which results in closer packing. Also, the closer packing of grains may be partly promoted by hot pressing [28].

Table 1 shows the 1500°C densification values for the three compositions examined in this study. It can be seen that the Al_4SiC_4 achieves nearly full densification (98.8%), while addition of WC gave rise to higher densification (99.5%), and addition of TiC resulted in reduced densification (98%). The lower densification of $\text{Al}_4\text{SiC}_4 + \text{TiC}$ was expected due to the higher consolidation temperature required for TiC [29]. A similar trend for $\text{Al}_4\text{SiC}_4 + \text{WC}$ was expected, but the results of the relative densities show higher densification. It is unclear why this occurred, but it may be due to the carbon content in the $\text{Al}_4\text{SiC}_4 + \text{WC}$, where the presence of sufficient carbon can help the densification of WC as previously stated. The presence of sufficient carbon is consistent with the fact that all the experiments were performed in a controlled atmosphere in order to keep the oxygen content as low as possible and subsequently prevent decarburization due to reduction of surface oxide. In support of this explanation, Oskroft et al. [28] reported that the presence of oxygen in the chamber consumes carbon and consequently reduces the carbon content. The XRD results confirmed the absence of W_2C , which

supports the idea of preventing decarburization [30]. Finally, the presence of sufficient carbon content leads to abnormal grain growth, which can be supported by the SEM micrographs [27, 30–32]. Hot pressing TiC and WC to high density at 1500 °C is notable, because this temperature corresponds to only 47% and 52% of the absolute melting temperatures of TiC and WC, respectively.

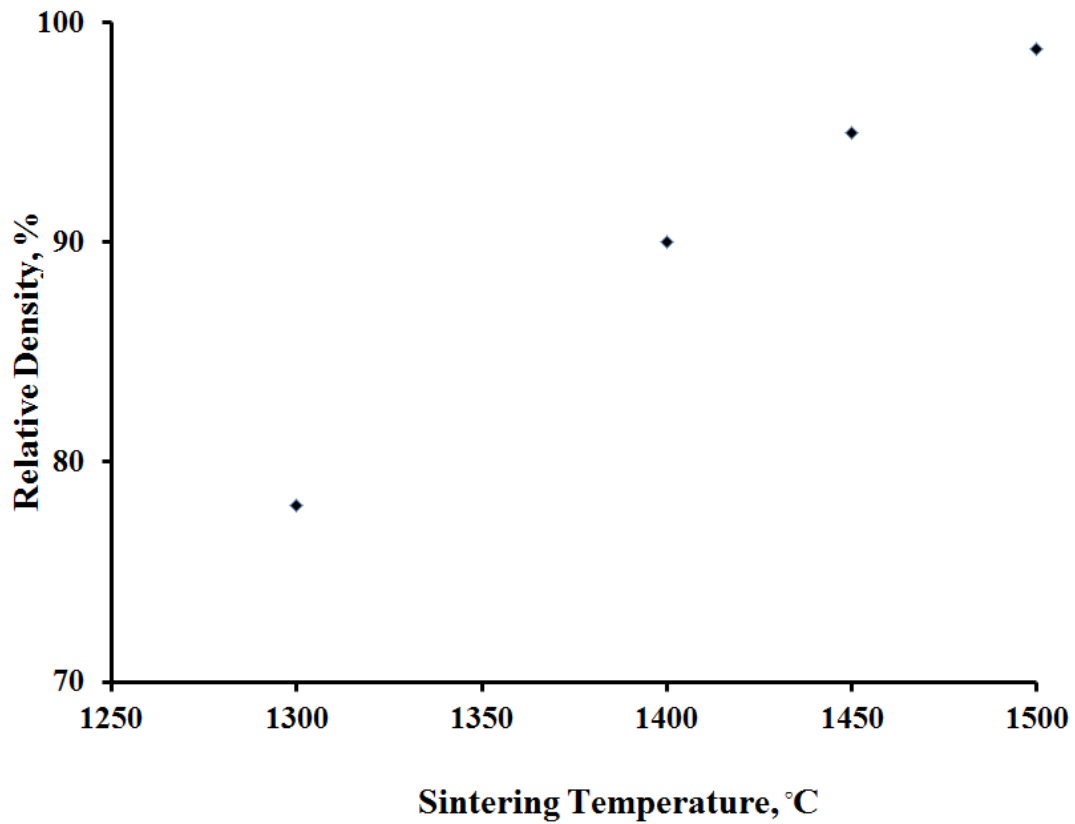


Fig. 5. Effect of sintering temperature on the relative density of hot-pressed Al_4SiC_4

Hardness

As shown in Fig. 6, the hardness values of hot-pressed Al_4SiC_4 increase with increasing sintering temperatures. In Table 1 the maximum Vickers hardness for Al_4SiC_4 of 12.73 GPa agrees well with the value reported previously [16]. The 14.63 GPa hardness of $\text{Al}_4\text{SiC}_4 + 30\% \text{ WC}$ and the 15.5 GPa hardness of $\text{Al}_4\text{SiC}_4 + 30\% \text{ TiC}$ were expected due to the higher hardness values of WC and TiC.

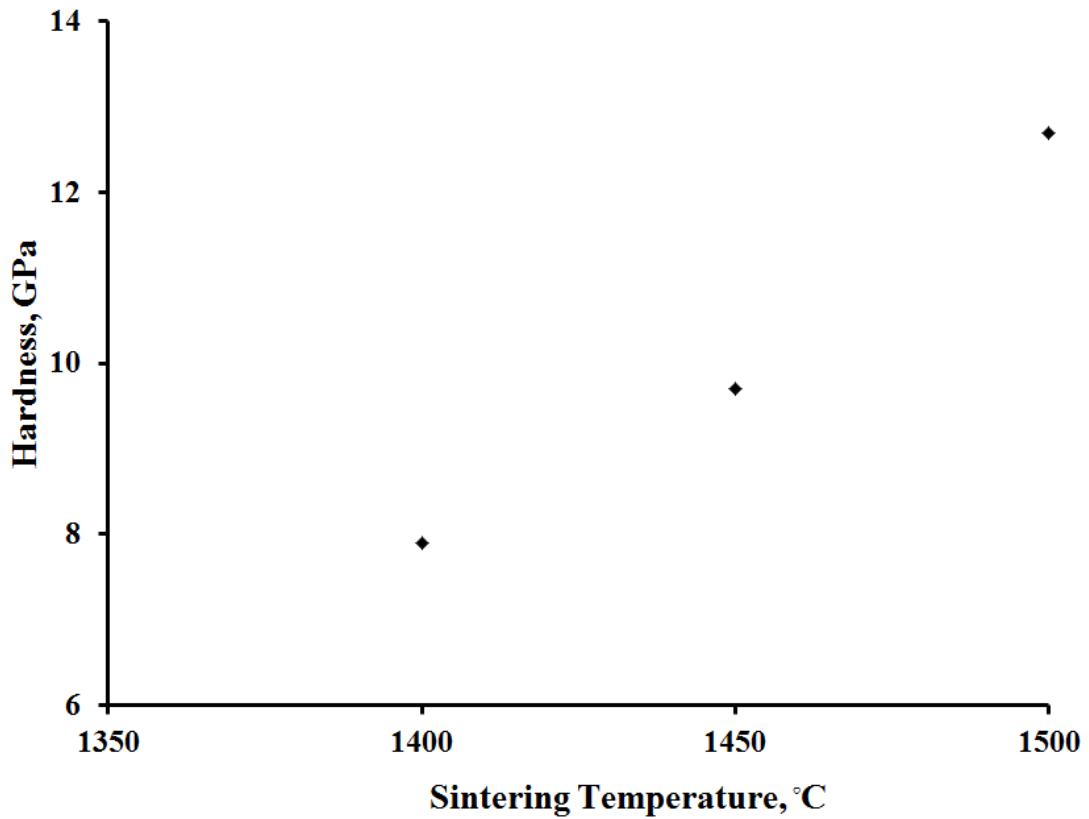


Fig. 6. Effect of sintering temperature on the hardness of hot-pressed Al_4SiC_4

Note that there are no values below 1400 °C because the samples were too porous to be measured.

Table 1 compares theoretical density, relative density, and hardness values of Al_4SiC_4 , $\text{Al}_4\text{SiC}_4 + 30\% \text{ WC}$, and $\text{Al}_4\text{SiC}_4 + 30\% \text{ TiC}$ to the values for two other ternary carbides, Ti_3SiC_2 and Ti_3AlC_2 . The hardness values of Ti_3SiC_2 and Ti_3AlC_2 are much lower than those of the materials used in this study. These lower values can be attributed to the planar Si layers linked together by TiC octahedra, forming a highly deformable basal slip plane [33]. However, in the crystal structure of Al_4SiC_4 , such a weak connective layer may not exist [1].

Table 1: Comparison of some properties of carbides, *Indicates results from current study.

	Ti_3SiC_2 ^[3]	Ti_3AlC_2 ^[3]	Al_4SiC_4 [*]	$\text{Al}_4\text{SiC}_4 + 30\% \text{ WC}^*$	$\text{Al}_4\text{SiC}_4 + 30\% \text{ TiC}^*$
Theoretical density (g/cm³)	4.53	4.21	3.03	6.83	3.6
Relative density (%)	99	99	98.8	99.5	98
Vickers hardness (GPa)	4	3.5	12.7	14.6	15.5

3.5 Conclusions

1. Single-phase Al_4SiC_4 was produced at 1450°C , which is a lower temperature than has been previously reported.
2. Full densification of Al_4SiC_4 occurred at 1500°C

3. As expected, the Al_4SiC_4 specimens containing 30% TiC and WC had higher hardness than single-phase Al_4SiC_4 .
4. Adding WC to Al_4SiC_4 increased densification to 99.5%.

3.6 Acknowledgements

Work at the Ames Laboratory was supported by the U.S. Department of Energy, Division of Materials Science & Engineering under contract DE-AC02-07CH11358. One of the authors (OG) wishes to acknowledge support from the Egyptian Ministry of Higher Education and Scientific Research.

Chapter 4: Properties of AlMgB₁₄ hot pressed with additions of ZrB₂ and HfB₂

A paper submitted November, 2011 to *Powder Technology*

Osama Gaballa ^{a,b,c}, Jonathon H. Ball, J. S. Peters ^b, Bruce Cook ^b, Alan Russell ^{a,b}

^a Department of Materials Science and Engineering, Iowa State University, Ames, IA 50011, USA

^b Ames Laboratory Division of Materials Science and Engineering, Iowa State University, Ames, IA 50011

^c Central Metallurgical Research and Development Institute, Helwan, Cairo, Egypt

^d Department of Materials Science and Engineering, Clemson University

4.1 Abstract

Powders of AlMgB₁₄, ZrB₂, and HfB₂ were combined by high-energy milling to produce AlMgB₁₄ + 60 vol. % ZrB₂ and AlMgB₁₄ + 60 vol. % HfB₂ composites. The powder constituents were hot pressed at two different temperatures, depending on prior conditioning of the milling vials. SEM and EDS were used to analyze microstructure impurities, and fracture mechanisms. XRD was used to verify proper phase formation and to check for impurity phases. The bulk AlMgB₁₄ + ZrB₂, and AlMgB₁₄ + HfB₂ show up to 97.3% and 98% densification, 22.2 and 24.5 GPa hardness (measured at 5K-gf), and 4.1 and 3.7 MPa(m)^{1/2} toughness, respectively. Also the study of bulk AlMgB₁₄ + ZrB₂, and AlMgB₁₄ + HfB₂ composites has shown that these materials exhibit high resistance to erosive and abrasive wear. Multi-hour ASTM erosion tests with Al₂O₃ abrasive material against composite samples comprised of AlMgB₁₄ (40 vol. %) + ZrB₂ (60 vol. %) and AlMgB₁₄ (40 vol. %) + HfB₂ (60 vol. %) resulted in erosion rates as low as 4.49 mm³ of (AlMgB₁₄ + ZrB₂) wear per kg of erodent and 2.85 mm³ of (AlMgB₁₄ + HfB₂) wear per

kg of erodent. These values compare with $14.9\text{mm}^3/\text{kg}$ for wear-resistant grades of WC–6% Co.

Keywords: Hard materials; Aluminum magnesium boride; Hafnium diboride; Zirconium diboride; Hot press;

4.2 Introduction

Hard materials are needed in numerous applications such as industrial machining, armor plating, and wear-resistant coatings [1-4]. While hardness is important for these applications, toughness, chemical stability, and corrosion resistance also play vital roles in reducing erosion and impact damage and increasing the life of tools and components.

It was often thought that in addition to strong bonding, super-hard materials must also possess simple crystallographic unit cells with high symmetry and a minimum number of crystal defects (e.g., diamond and cubic boron nitride (cBN)). However, a new hard material that deviates from this paradigm has begun to receive attention. This new material is AlMgB_{14} , which has a large, orthorhombic unit cell (oI64) with multiple icosahedral boron units [5, 6]. The AlMgB_{14} unit cell typically has a high concentration of vacancies on the metal atom sites. While the relationship between these vacancies and the material's hardness is incompletely understood [7], it may be that hardness is actually enhanced by these defects [8, 9].

Group IV metal diborides (XB_2 , where X = Ti, Zr, or Hf) are hard, ultra-high temperature ceramics (UHTCs). These compounds have a primitive hexagonal crystal structure (hP3)

with planes of graphite-like boride rings above and below planes of metal atoms [10]. Unlike graphite, there is strong bonding between the planes, resulting in high hardness.

TiB₂ has already been shown to be a reinforcing phase in AlMgB₁₄, raising hardness, wear resistance, and corrosion resistance [11]. Previous studies determined that 50-60 vol. % TiB₂ offered the highest hardness and toughness values in two-phase, sub-micron-scale composites with AlMgB₁₄. It was considered that ZrB₂ and HfB₂ might behave similarly, so for this study two-phase composites of 60 vol. % metal diborides with 40 vol. % AlMgB₁₄ were produced and characterized.

4.3 Experimental

Two types of precursor powders were prepared for this research. AlMgB₁₄ powder, previously prepared by attritor milling, was vibratory-milled with ZrB₂ or HfB₂ (both 99.5% metal basis purity and -325 mesh powder) to form 60 vol. % ZrB₂ + 40 vol. % AlMgB₁₄ and 60 vol. % HfB₂ + 40 vol. % AlMgB₁₄ samples.

The attritor-milled AlMgB₁₄ started as powders of 95% pure B, 99.8% pure Mg, and 99.99% pure Al. The milling was performed with a 10:1 media-to-powder ratio and was milled for 4 hours in a Zoz Simoloyer attritor mill. The AlMgB₁₄ and ZrB₂ or HfB₂ powders were then milled together for 30 minutes in a Spex-8000 vibratory/oscillatory milling machine. All powder handling was performed in a glove box filled with purified helium, and only sealed vials of these materials were exposed to the atmosphere. Powder produced by the initial milling was separated from subsequent millings because of differences in impurities and particle size resulting from use of an unconditioned vial

(i.e., the interior vial and media surfaces were not coated prior to milling). All subsequent millings of $\text{ZrB}_2/\text{AlMgB}_{14}$ or $\text{HfB}_2/\text{AlMgB}_{14}$ samples were considered to be conditioned (i.e., with interior surfaces pre-coated with the boride compounds).

A Centorr hot press was used for consolidation of the powders. Pressing was accomplished in graphite dies under an atmosphere of flowing argon gas. Boron nitride and graphite sheet were used as a lubricant to line the inner surfaces of the dies and protect them from reaction with the boride compounds. Three types of samples were pressed for each type of boride addition to the AlMgB_{14} . An unconditioned sample and a conditioned sample were each pressed at 1400°C for 1 hour at a pressure of 105 MPa. Another conditioned sample was also pressed at 1500°C for 1 hour with a pressure of 105 MPa to evaluate possible differences resulting from a higher consolidation temperature. After hot pressing, the compacts were removed from the dies and metallographically polished.

Sample density was determined by the Archimedes displacement method (according to MPIF Standards 42, 1998) [12]. Vickers microindentation was used to calculate the hardness of the samples. Indentation was applied with load of 5 kg-f and was also used to estimate toughness by the Palmqvist method, based on the length of the median cracks [13]. Scanning electron microscopy (SEM) and energy dispersive spectroscopy (EDS) were used to analyze microstructure, impurities, and fracture mechanisms. X-ray diffraction was also used to verify proper phase formation and to check for impurities.

Erosion resistance was determined by measuring mass change of the samples after exposure to a high-velocity abrasive jet using ASTM G 76 procedures. Alumina (Al_2O_3) grit (+100 μm , Comco, Inc.) was used in a stream of dry compressed air or N_2 at an operating pressure of 275 kPa to impact the sample at a constant rate and particle velocity over 100 m/s[14]. Mass change and abrasive usage were measured at 30, 60, 90, and 120 minutes of testing. These values were used to calculate the ratio of sample volume loss to erodent mass consumed. The reported erosion rate corresponds to the steady-state value, which was found to remain constant independent of testing time.

Samples of the previously synthesized AlMgB_{14} - TiB_2 composite were produced to serve as control specimens.

4.4 Results and discussion

4.4.1 XRD

XRD was used to verify formation of the desired phases. Fig. 1 shows the XRD patterns for AlMgB_{14} + 60 vol. % ZrB_2 and AlMgB_{14} + 60 vol. % HfB_2 sintered at 1500 °C for 1 hour. As can be seen, the XRD patterns of the hot-pressed samples show the presence of three phases; AlMgB_{14} and ZrB_2 in Fig.1A, and AlMgB_{14} and HfB_2 in Fig.1B. This indicates that hot pressing of AlMgB_{14} with ZrB_2 or HfB_2 for 1 hour under a pressure of 106 MPa is adequate to produce two-phase AlMgB_{14} + ZrB_2 and AlMgB_{14} + HfB_2 with good phase purity.

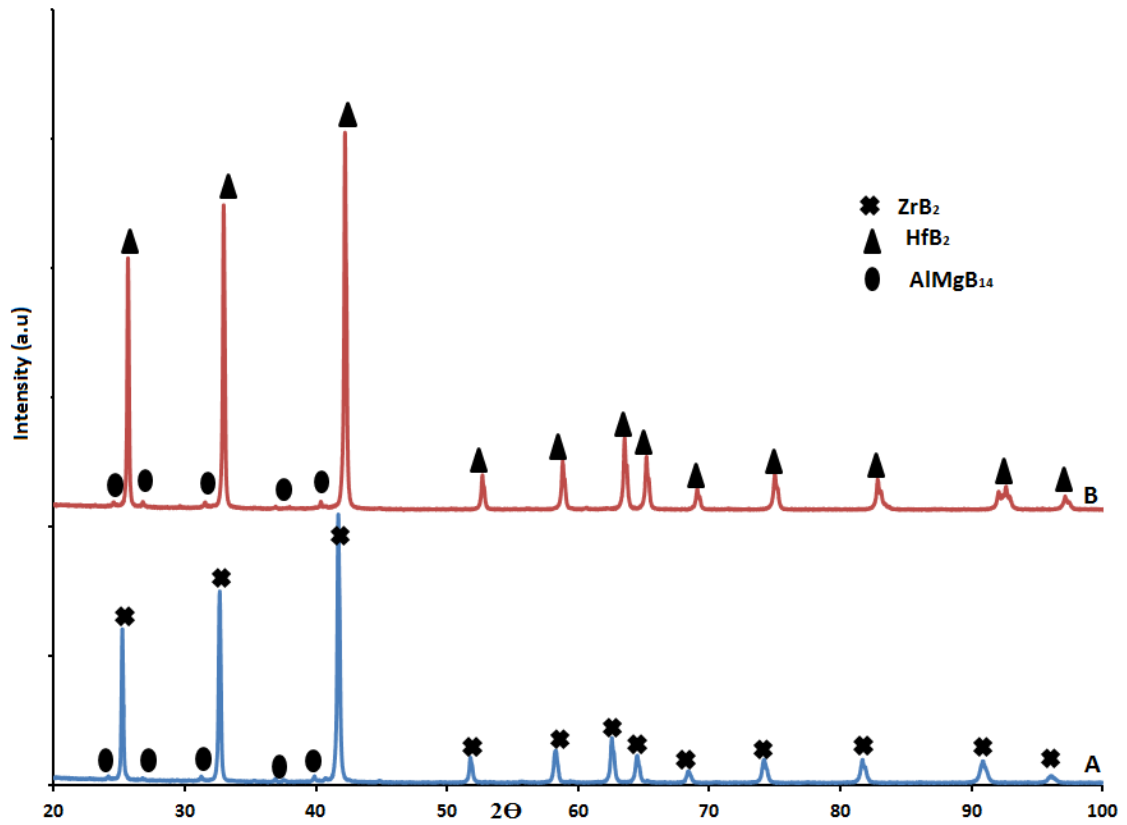
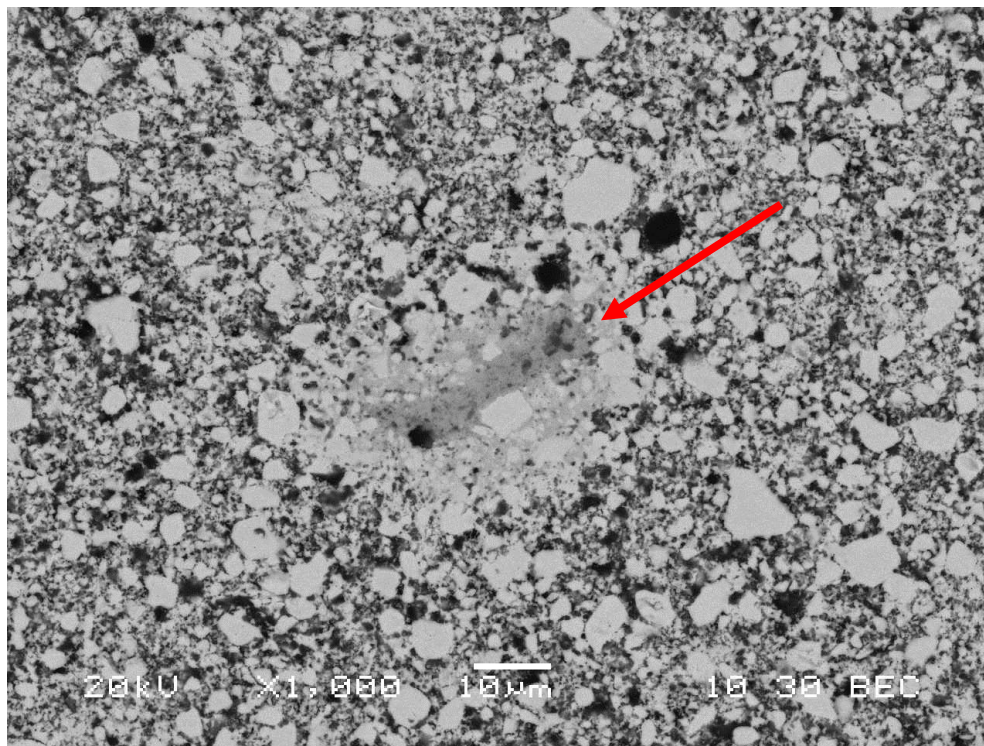


Fig. 1 XRD patterns of A) $\text{AlMgB}_{14} + \text{ZrB}_2$, and B) $\text{AlMgB}_{14} + \text{HfB}_2$ hot pressed at 1500°C for 1 hour in flowing Ar.

4.4.2 Microstructure of AlMgB_{14} samples with additions of ZrB_2

The sample of AlMgB_{14} containing 60 vol. % ZrB_2 prepared in an unconditioned Spex vial and pressed at 1400°C was examined by SEM/EDS (Fig. 2). SEM examination showed that the 30-minute milling time was sufficient to promote good mixing of the two phases and yielded a uniform, consistent microstructure. Although there were a number of relatively large particles of ZrB_2 compared to the number of AlMgB_{14} agglomerates,

the overall sample seems to be well mixed and homogenous when compared to TiB_2 and AlMgB_{14} .



(a)

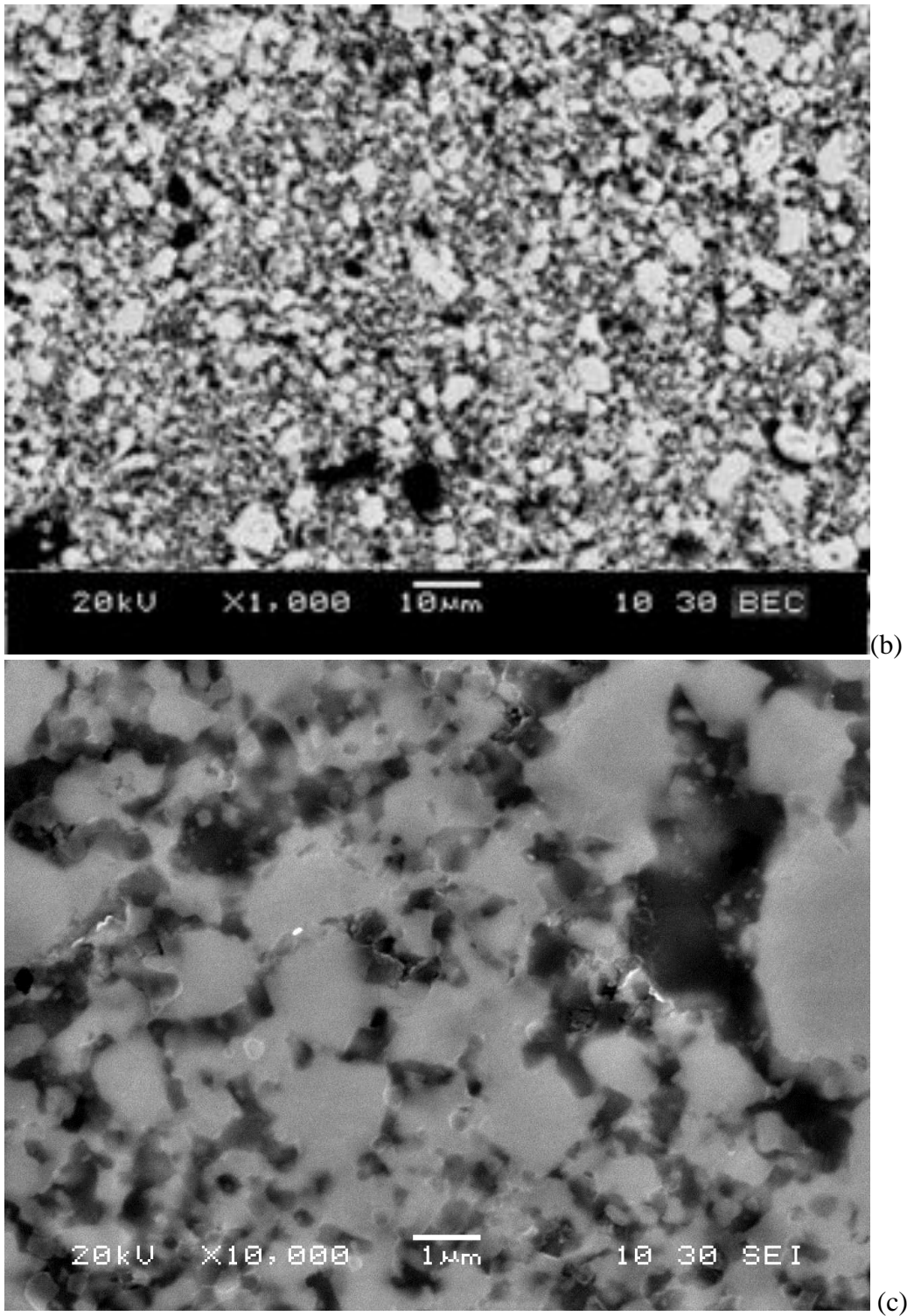


Fig. 2: Comparison of microstructures of $\text{ZrB}_2 + \text{AlMgB}_{14}$ composite produced in an unconditioned Spex vial and hot pressed at 1400°C with $\text{TiB}_2 + \text{AlMgB}_{14}$ composite produced under the same conditions. (a) backscattered SEM of $\text{ZrB}_2 + \text{AlMgB}_{14}$, (b) backscattered SEM image of $\text{TiB}_2 + \text{AlMgB}_{14}$ (c) higher magnification, secondary electron SEM image of $\text{ZrB}_2 + \text{AlMgB}_{14}$

One region shown in Figure 2a (arrow) was a multi-layered agglomerate containing three distinct microstructures. Figure 3 provides a backscattered image of one of the agglomerates along with notations on the chemical compositions of various points in this image. Since back-scattered SEM displays provide brighter images of particles with higher Z (atomic number), the dark areas in these images may be regions where the Zr atoms have been replaced with lighter metal atoms such as Fe or Cr (indicated by EDS). At the center is a much darker area with no EDS evidence of AlMgB_{14} or ZrB_2 ; farther away from the center, AlMgB_{14} and ZrB_2 phases are detected. Even in the region farther from the center, there appears to be little AlMgB_{14} , and the ZrB_2 particles that are present appear darker than normal, suggesting that their chemical composition deviates from pure ZrB_2 . In the third layer away from the center, the ZrB_2 seems to be normal, while the AlMgB_{14} phases are still scarcer than in the bulk material. EDS analysis showed that significant amounts of Fe and Cr are present, likely from wear of the hardened steel vial/milling media used for sample preparation. Prior work on similar materials indicates that the Fe content is less than 3% [15]. Also, the absence of diffraction peaks corresponding to Fe in the XRD patterns supports this claim.

It is possible that Fe and Cr contamination likely resided in the center of this region and that the Fe diffused faster than the Cr, thus areas farther away from the center are richer in Fe. Also with the pores present in the secondary image, it is possible the Cr and Fe both started in this porous region, perhaps in the form of a metal flake, and melted into a

liquid that flowed out into the sample. It's possible an FeB-rich flux was formed during hot pressing

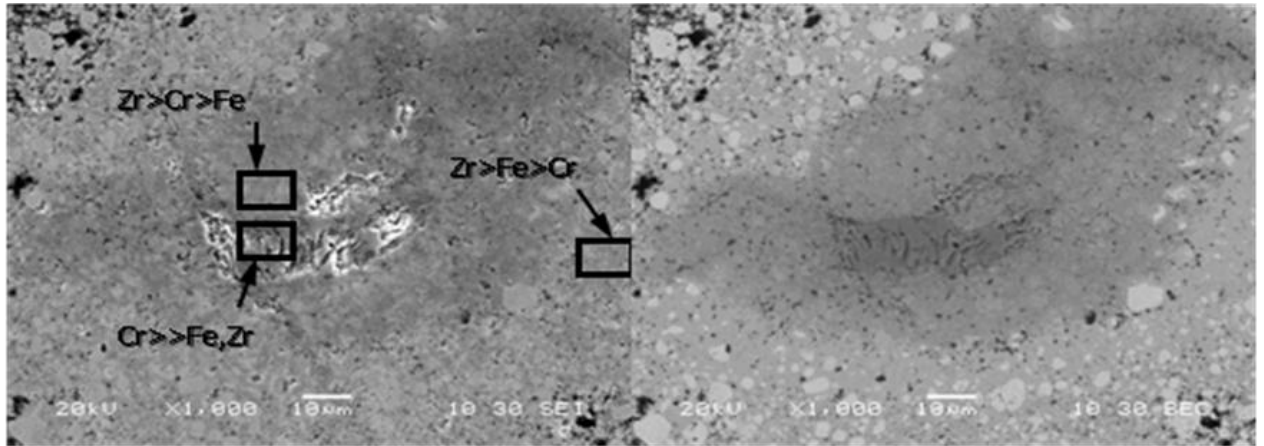


Fig. 3 SEM images of the $\text{AlMgB}_{14} + \text{ZrB}_2$ composite (agglomerate) in back-scattered (left) and secondary-electron imaging (right) modes showing pores and impurities.

The melting points of Fe and Cr are 1530°C and 1900°C respectively, which may explain why the Fe appears to diffuse faster [16]. By introducing Cr and Fe wear debris into the sample's microstructure, other phases were formed by reaction with the AlMgB_{14} and ZrB_2 . These same impurity particles were frequently observed in the samples containing ZrB_2 additions, although, their presence seemed to decrease as milling time increased. These impurity particles were much less frequently observed in the HfB_2 samples. Figure 4 shows a ZrB_2 grain surrounded by new crystals that have formed. EDS suggests that these new crystals formed by reaction of Cr and Fe with the ZrB_2 .

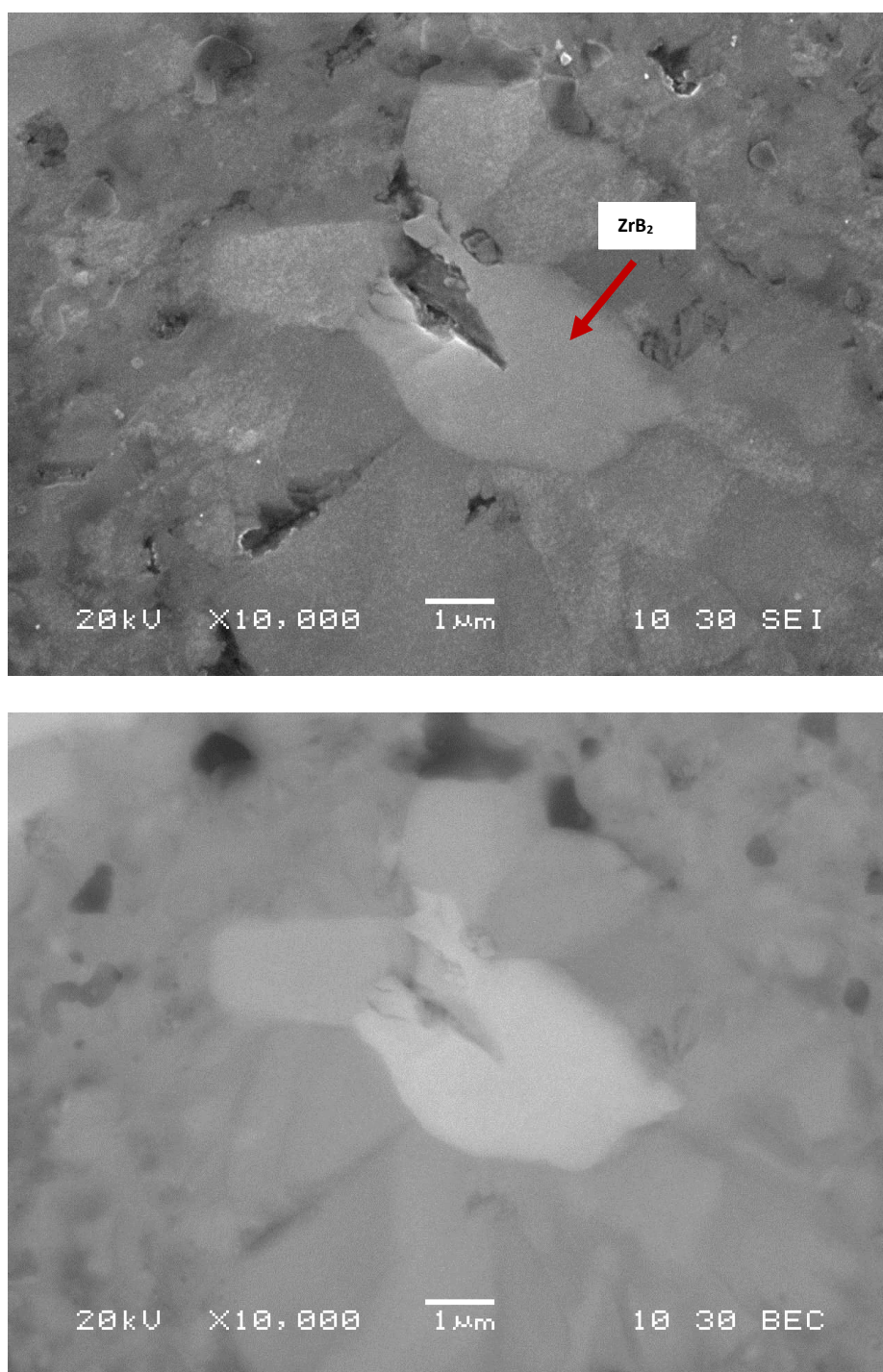
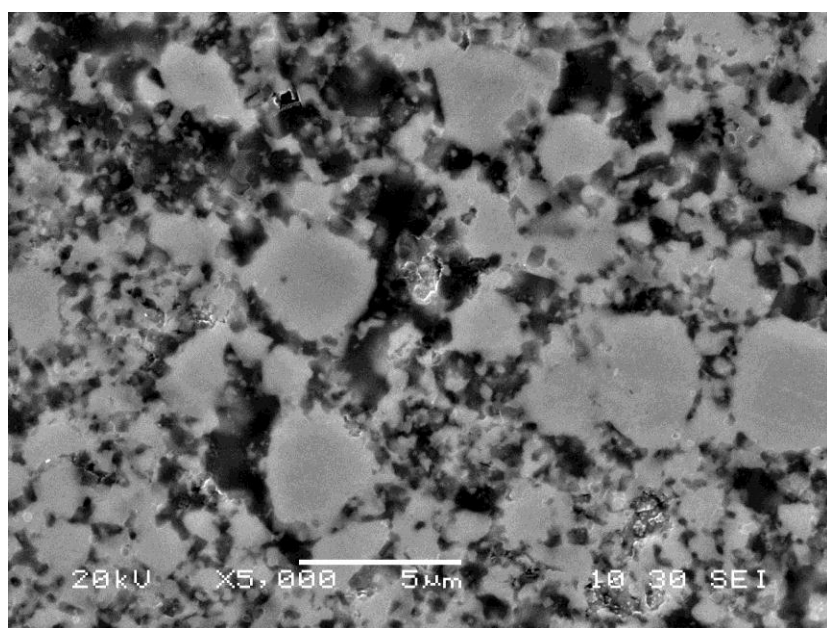
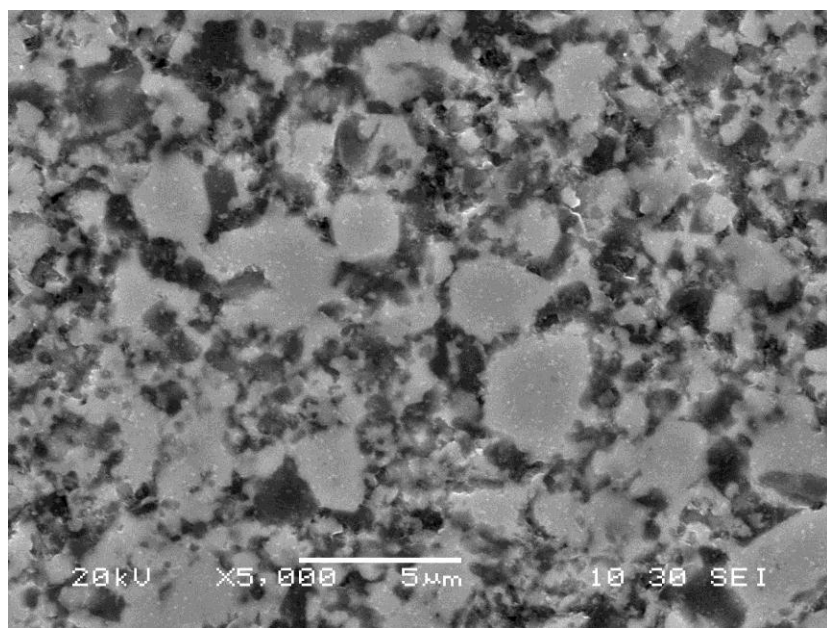


Fig. 4 ZrB₂ particle in center that has reacted with Fe and Cr, forming new crystals around the particle

SEM of the $\text{AlMgB}_{14}+\text{ZrB}_2$ samples produced in conditioned vials showed far fewer of these unusual particles. Figure 5 shows increased porosity in samples produced in Spex vials with greater amounts of conditioning. The images are arranged in order of the amount of vial conditioning, with increased conditioning as the images progress from (a) to (d). The two samples labeled (b) and (c) were both pressed at 1400°C for 60 minutes at 105 MPa. These images suggest that the impurities from the Spex vial wear debris may actually lead to better sintering and densification. The Spex vial should become more conditioned over time; although, this should have little to no effect on the samples after the first milling. In this case, porosity appears to increase, with fewer impurity particles as a vial's total milling time increases. We suspect that fewer impurities in samples produced in extensively conditioned vials deprive the material of the impurity sintering aids that reduce porosity during hot pressing.



(a)



(b)

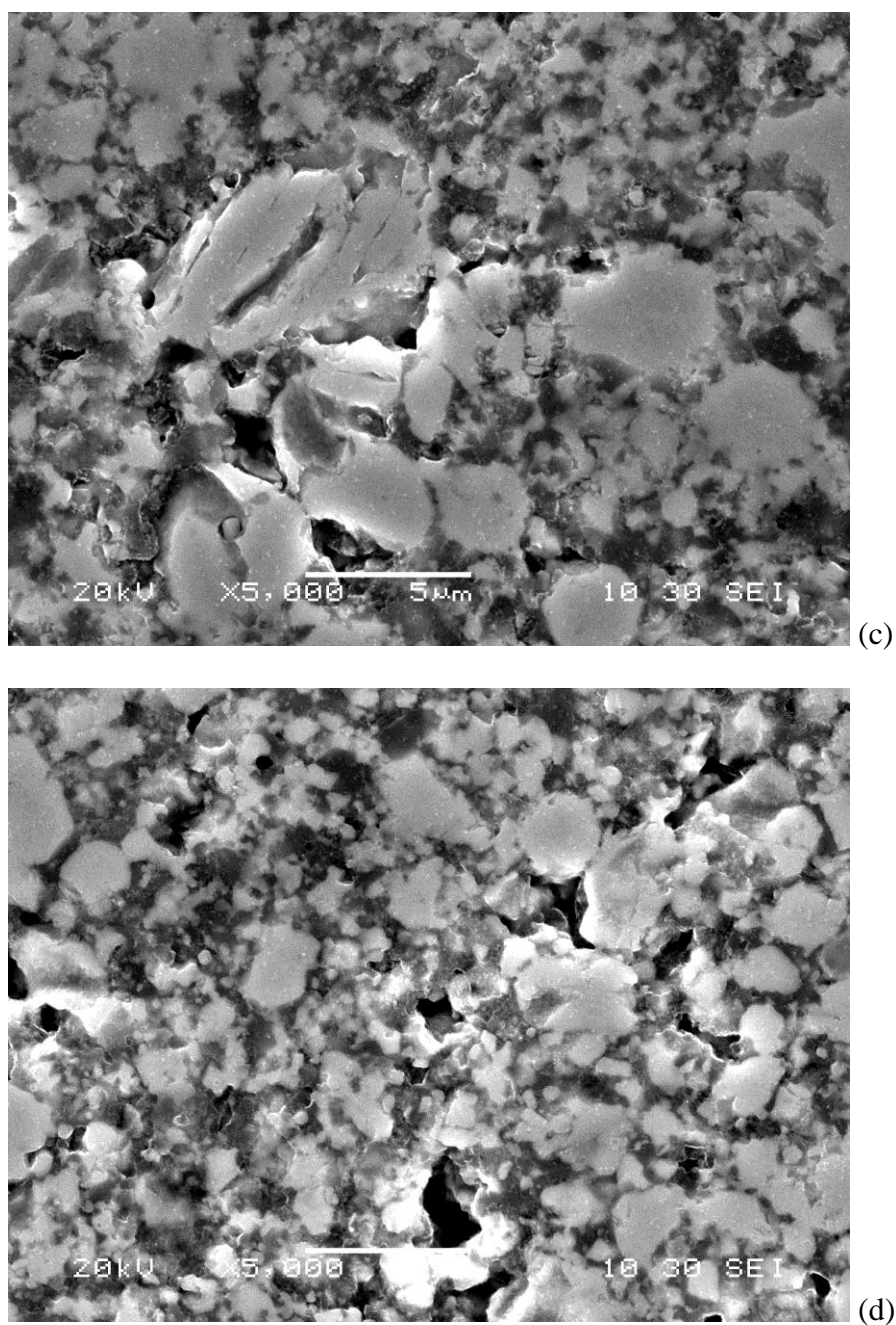
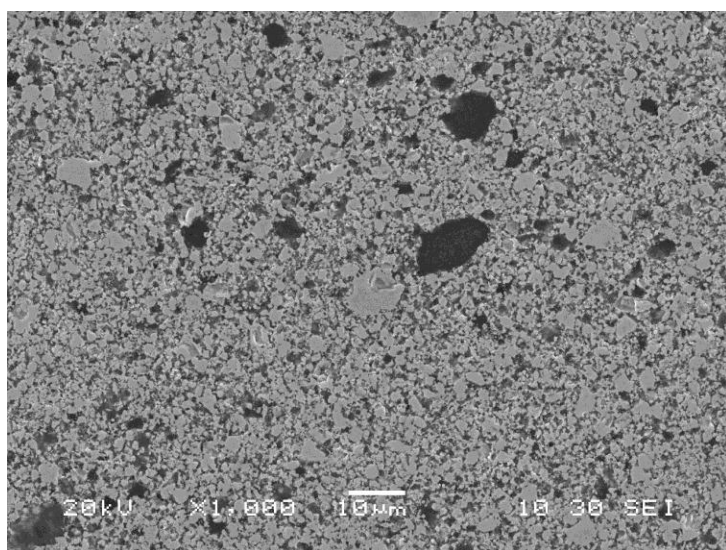
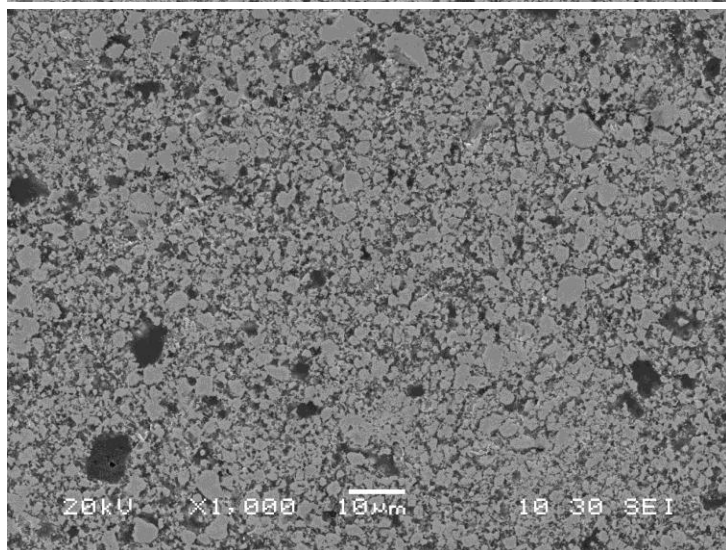


Fig. 5 Secondary SEM of ZrB_2 additions that show increasing porosity from (a) to (d). a) unconditioned powder pressed at 1400°C , b) conditioned powder pressed at 1400°C , c) extended milling of conditioned powder pressed at 1400°C , and d) additional milling beyond c) of conditioned powder pressed at 1500°C .

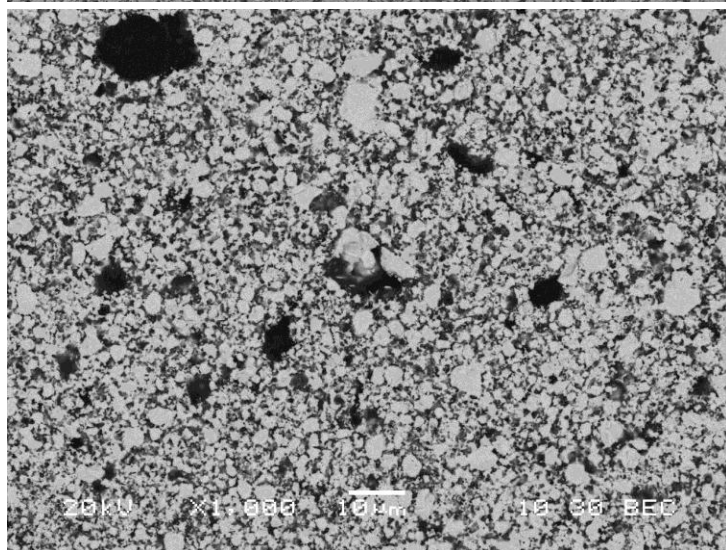
Figure 6 shows representative SEM images that verify consistent mixing throughout the $\text{AlMgB}_{14}+\text{HfB}_2$ samples. The degree of mixing and grain size are similar throughout the samples. Little porosity was seen in the samples, suggesting better densification of the material compared to ZrB_2 specimens. This can be supported when comparing between Fig. 6e and Fig. 5a and also from quantitative data given in table 1. Figure 6 compares the $\text{AlMgB}_{14}+\text{HfB}_2$ samples with a sample containing TiB_2 additions. The samples containing HfB_2 additions show more consistent mixing than do those with TiB_2 additions.



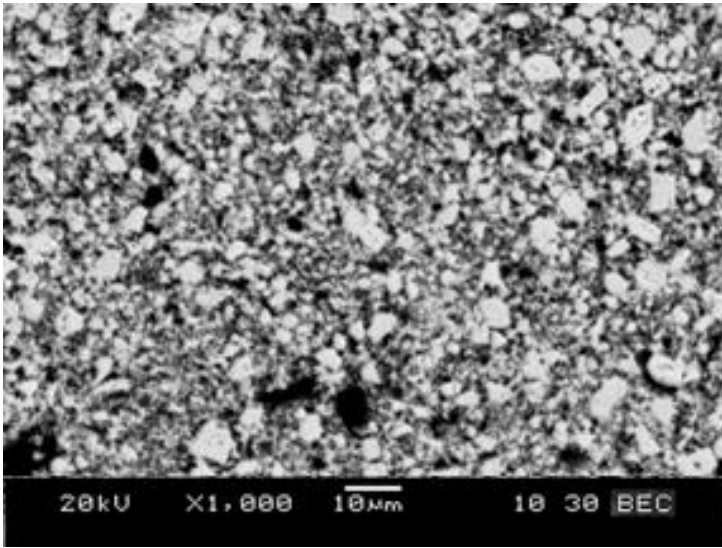
(a)



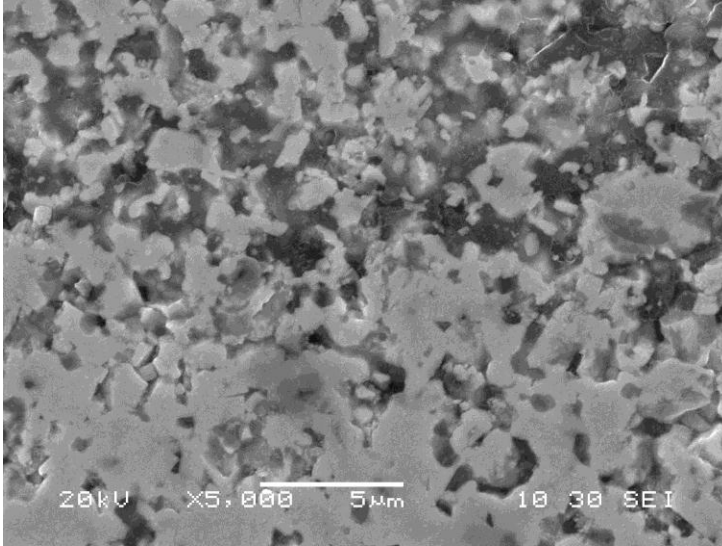
(b)



(c)



(d)

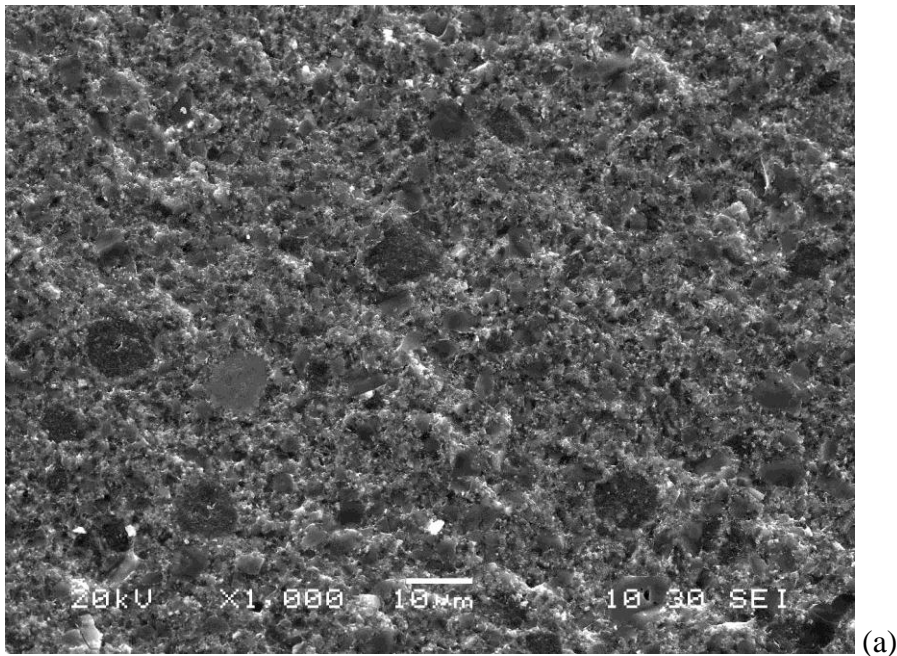


(e)

Fig. 6: Secondary-electron and back-scattered SEM micrographs of HfB_2 additions and TiB_2 additions to AlMgB_{14} . (a) unconditioned $\text{HfB}_2/\text{AlMgB}_{14}$ powder pressed at 1400°C , (b) conditioned $\text{HfB}_2/\text{AlMgB}_{14}$ powder pressed at 1400°C , (c) conditioned $\text{HfB}_2/\text{AlMgB}_{14}$ powder pressed at 1500°C , (d) conditioned $\text{TiB}_2/\text{AlMgB}_{14}$ powder pressed at 1400°C , and (e) higher magnification for Fig. 6a which is used for comparison with Fig. 5a .

4.4.3 Microstructure of fracture surfaces of AlMgB₁₄ samples with TiB₂ additions, ZrB₂ additions, and HfB₂ additions

Figure 7 shows fracture surfaces of AlMgB₁₄ samples containing additions of TiB₂, ZrB₂, and HfB₂. Although the fracture appears to be a mixed-mode fracture, it is predominately intragranular in all three compositions. While intergranular fracture is generally thought to improve fracture toughness in ceramics [17], the exceptionally strong bonding between phases in these composites raises the activation energy for intergranular crack propagation. This is believed to act as a positive contribution to hardness, because the grain boundaries do not act as crack propagation paths [18]. This is thought to contribute to the high wear resistance of AlMgB₁₄ - TiB₂ composites, and suggests that wear resistance may also be high in AlMgB₁₄ with ZrB₂ and HfB₂ additions.



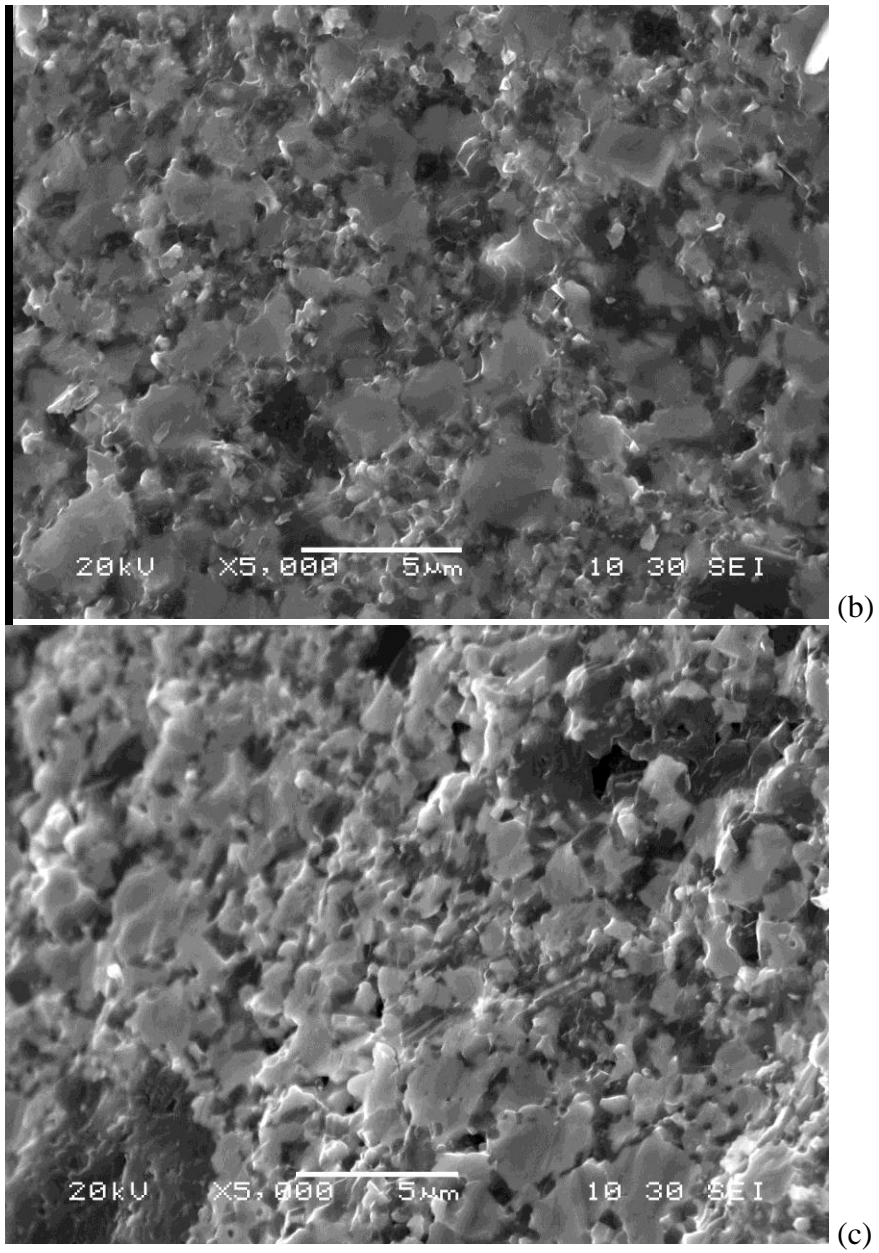


Fig.7 Secondary SEM micrographs of fracture surfaces of AlMgB₁₄ samples containing additions of; (a) TiB₂, (b) ZrB₂, and (c) HfB₂.

4.4.4 Densification and mechanical properties of AlMgB₁₄ samples with additions of ZrB₂ and HfB₂

AlMgB₁₄ samples with ZrB₂ and HfB₂ additions were hot pressed at 1400°C and 1500°C, followed by measurement of the density of the resulting compacts and some of their mechanical properties (Table 1). Two trends were observed in the densification data of the three samples pressed at 1400°C containing ZrB₂ additions. First, as milling time increased, the % density decreased, most likely due to reduction in the amount of sintering aid present, as previously discussed. This is consistent with the samples' appearance in the SEM micrographs. Second, as the porosity increased, so did the erosion rate, which was expected. For the sample pressed at 1500°C with ZrB₂ additions, the erosion rate was substantially lower even though the percent density remained nearly the same. This is may be attributable to the fact that the sintering aid had a longer time to chemically react with neighboring grains. In addition, pressure is not applied until temperature is stabilized, which is likely occurring after the new bonds are formed. Thus, the particles were unable to rearrange and change their shape during bond formation, leaving porosity behind. Although pressure was applied after bond formation, the applied pressure may not have been sufficiently high to rearrange the new, stronger structure and remove porosity. For the samples containing ZrB₂ additions, the sample pressed with powder from the unconditioned vial displayed the highest wear resistance, probably because its density was the highest, stemming from its impurity/sintering aid concentration. This was the case even though the hardness and toughness were both lower than in the first sample made with a conditioned vial and pressed at 1400°C. This

implies the existence of secondary variables that, in addition to hardness and toughness, also affect the material's erosion rate. The sample pressed at 1500°C also had an erosion rate nearly as low as that of the unconditioned sample pressed at 1400°C. These observations suggest that if the unconditioned powder sample with the impurities had been pressed at 1500°C to achieve the same densification as the 1400°C sample, the erosion rate likely would have been lower still.

Table 1 Density, hardness, toughness and erosion rate of AlMgB₁₄ samples with additions of 60 vol. % ZrB₂ and HfB₂. *Sample difficult to measure.

Material	Pressing Temperature °C	Conditioned Mill Vial/media	Density g/cm ³	RD %	Vickers hardness GPa	Toughness MPa(m) ^{1/2}	Erosion Rate mm ³ /kg
AlMgB ₁₄ +							
ZrB ₂	1400	No	4.64	97.3%	21.6	3.28	4.49
ZrB ₂	1400	Yes	4.58	96.0%	22.2	3.68	5.31
ZrB ₂	1400	Yes	4.49	94.1%	19.9	4.09	7.90
ZrB ₂	1500	Yes	4.50	94.3%	*	*	4.85
HfB ₂	1400	No	7.65	98.0%	24.0	3.56	3.07
HfB ₂	1400	Yes	7.42	95.0%	24.5	3.67	2.85
HfB ₂	1500	Yes	7.54	96.5%	24.2	3.46	3.80

The AlMgB₁₄ samples containing HfB₂ additions did not follow the trends seen in the samples with ZrB₂ additions. Although the sample with HfB₂ additions pressed at 1400°C with powder from a conditioned vial had among the lowest density, it exhibited the best

wear resistance. The two samples with HfB_2 additions pressed at 1400°C displayed similar values for hardness, toughness, and wear-resistance, even though the lower density samples outperformed the other sample. The sample with HfB_2 additions pressed at 1500°C exhibited similar hardness, but also a lower toughness compared to those pressed at 1400°C , which likely accounts for the decrease in erosion resistance.

Table 2 compares AlMgB_{14} samples with ZrB_2 and HfB_2 additions to currently available commercial materials. The Roctec 500 WC outperforms the samples containing AlMgB_{14} and group IV metal diborides, but the boride samples are much lighter and may have a lower cost. The large difference in erosion rate between the AlMgB_{14} material containing TiB_2 (from previous studies) and the corresponding samples from this work containing HfB_2 or ZrB_2 is believed to be due primarily to the higher porosity in the latter. The samples containing HfB_2 additions exhibit nearly half the erosion rate of the ZrB_2 -containing samples.

Table 2 AlMgB_{14} samples with additions in comparison with materials used in industry such as K68 WC and Roctec 500 WC.

Material	Density (g/cm^3)	Hardness (GPa)	Toughness $\text{MPa(m)}^{1/2}$	Erosion Rate mm^3/kg
Roctec 500 WC	15.0	30		0.14
K68 WC	14.9	23	---	14.32
$\text{TiB}_2 + \text{AlMgB}_{14}$	3.84	26-28	3-4	0.49 [13]
$\text{ZrB}_2 + \text{AlMgB}_{14}$	4.58	22.2	3.68	5.31
$\text{HfB}_2 + \text{AlMgB}_{14}$	7.42	24.5	3.67	2.85

4.5 Conclusions

ZrB₂ and HfB₂ additions to AlMgB₁₄ show promise for industrial applications as bulk materials and as coatings for cutting tools, armor, and wear-resistant materials. The samples with HfB₂ additions were harder and more erosion-resistant than the samples with ZrB₂ additions. In other tests (such as toughness), the samples were similar. When comparing the wear resistance of these samples with industrial WC materials, the samples fall between the standard grade K68 and the wear-resistant Roctec 500 grade. Porosity was seen to increase in ZrB₂ samples prepared with conditioned vials, while this effect was not as pronounced in the corresponding samples prepared with HfB₂.

4.6 Acknowledgements

Work at the Ames Laboratory was supported by the U.S. Department of Energy, Division of Materials Science & Engineering under contract DE-AC02-07CH11358.

Chapter 5: Reduced-temperature processing and consolidation of ultra-refractory

Ta₄HfC₅

A paper submitted May, 2012 to *Materials Science and Engineering: A*

Osama Gaballa ^{a,b,c}, Bruce Cook ^b, Joel Harringa ^b, Alan Russell ^{a,b}

^a Department of Materials Science and Engineering, Iowa State University, Ames, IA 50011, USA

^b Ames Laboratory Division of Materials Science and Engineering, Iowa State University, Ames, IA 50011

^c Central Metallurgical Research and Development Institute, Helwan, Cairo, Egypt

5.1 Abstract

Powders of TaC, HfC, and WC were combined by high-energy milling and hot pressing to produce Ta₄HfC₅, in addition to composites of Ta₄HfC₅ + 30 vol. % WC, and Ta₄HfC₅ + 50 vol. % WC. Sub-micron powders were examined after four different milling intervals prior to hot pressing. XRD was used to verify proper phase formation. SEM, relative density, and hardness measurements were used to examine the resulting phases. Hot-pressed compacts of Ta₄HfC₅ showed densification as high as 98.6% along with Vickers hardness values of 21.4 GPa. Similarly, Ta₄HfC₅ + 30 vol. % WC exhibited 99% densification with a Vickers hardness of 22.5 GPa. These levels of densification were achieved at 1500°C, which is lower than any previously reported sintering temperature for Ta₄HfC₅. Microhardness values measured in this study were higher than those previously reported for Ta₄HfC₅. The WC additions to Ta₄HfC₅ were found to improve densification and increase microhardness.

Keywords: Tantalum hafnium carbide; Ultra-refractory materials; Powder processing; Tungsten carbide; Hot press

5.2 Introduction

Carbides, nitrides, and borides are of interest for many applications because of their high melting temperatures, high elastic moduli, and high hardness. Among all refractory compounds, Ta_4HfC_5 ranks among the highest, with an estimated melting temperature of 3942°C and hardness around 20 GPa at 100 gram-force [1-3]. TaC is the most metallic of the IV and V transition metal monocarbides. It has the NaCl-type structure (B1, space group $\text{Fm}\bar{3}\text{m}$) and an exceptionally high melting point of 3880°C [4-7].

TaC's good oxidation resistance and resistance to chemical attack have been attributed to strong covalent-metallic bonding [8]. Other properties of TaC include high strength, high hardness (11 to 26 GPa), wear resistance, fracture toughness ($K_{\text{IC}} \approx 12.7\text{MPa}\cdot\text{m}^{1/2}$), low electrical resistivity ($42.1\ \mu\Omega\cdot\text{cm}$ at 25°C), and high elastic modulus (up to 550GPa). TaC is also reported to exhibit a ductile-to-brittle transition in the temperature range $1750\text{-}2000^\circ\text{C}$ that allows it to be shaped above the DBTT, and it also exhibits ductility of 33% at 2160°C [9-12].

Similarly, HfC also crystallizes in the NaCl-type structure (B1, space group $\text{Fm}\bar{3}\text{m}$, close packed), and exhibits a high melting point (3890°C , the highest among the binary metallic compounds) [13-15]. HfC also has good chemical stability, high oxidation resistance, high hardness (up to 33 GPa[16]), high electrical and thermal conductivity, and a high Young's modulus (up to 434GPa) [17-24].

These properties make TaC potentially useful for a range of demanding applications, including fabrication of wear-resistant parts, diffusion barriers, hypersonic vehicles (leading edges and nose-caps), propulsion components (rocket nozzles), scramjet components, supersonic re-entry vehicles, hard coatings, conducting films, oxidation-resistant coatings, optical coatings, electrical contacts, electronic applications, and as a reinforcing phase in tool steels [25-31].

HfC could be used in aerospace applications due to its high melting point and low diffusion coefficients at high temperatures (e.g., thermal protection materials in both re-entry and hypersonic vehicles). It is used in coatings for ultrahigh-temperature environments due to its high hardness, excellent wear resistance, good resistance to corrosion, and low thermal conductivity. HfC is also found in high-temperature shielding, field emitter tips, and arrays (HfC has the lowest work function of all transition metal carbides). In addition, HfC is used as a reinforcing phase in tool steels [32-34].

For most materials, sintering requires temperatures above 50% of the absolute melting point, so the high melting points of TaC and HfC make sintering of powders challenging. The challenge is made greater still by these materials' low self-diffusion coefficients and high activation energies for viscous flow. Many investigators have reported sintering studies on TaC. Densification of TaC powders has been achieved by hot pressing at temperatures ranging from 1900°C to 2400°C, often with use of additives to decrease the sintering temperature. These additives can lead to a reduction in the sintering temperature but can also cause excessive grain growth, inability to attain full density, and degraded mechanical properties [35-39].

To inhibit grain growth, other investigators have studied rapid sintering of nanostructured TaC [44] and rapid sintering by spark plasma sintering, with and without additives [45-47]. It has also been found that the simultaneous application of high pressure (e.g., hot pressing) assists densification and reduces the sintering temperature [48]. Reducing the particle size of the powders was also found to improve densification [49]. Also, adding excess carbon decreased grain growth and increased density [50].

For HfC, many consolidation trials have been performed using MoSi₂ (hot pressing and pressure-less) or TaSi₂ as additives to aid sintering or using ultrafine powder to decrease the sintering temperature [40-42].

Transition metal carbides of groups IVB and VB that crystallize in the NaCl-type structure have unlimited solid solutions [M_{1x}M_{21-x}]C_y, where M1 and M2 are transition metals [43]. As a result, HfC and TaC form a continuous single-phase cubic (NaCl structure) Ta-Hf-C solid solution, reported to possess the highest melting temperature among all known materials. Studies of the electronic structure of Ta₄HfC₅ showed the main contribution to chemical bonding in HfC and TaC results from a strong hybridization of the Hf (Ta) 5d- and C 2p-like states [44]. Agte, et al reported that the melting point of Ta₄HfC₅ is 3942°C, which is higher than that of either pure TaC or HfC [1]. This claim was subsequently confirmed by Andrievskii [2]. Also, the high-temperature hardness of (Ta_{0.8}Hf_{0.2})C_{1+x} displays a positive deviation from the rule-of-mixtures, exceeding that of both pure-metal carbides TaC_{1-x} and HfC_{1+x}. [45].

The extreme melting point and high hardness of Ta_4HfC_5 suggest that it could be useful in aerospace components such as composite rocket thrusters. With starting powder of 1.5 μm average particle diameter, Fisher achieved full densification of 4TaC-HfC at 2538°C with an applied pressure of 48 MPa and 15 minute holding time [40]. This illustrates the difficulty of sintering 4TaC-HfC, a challenge shared by all the high-melting materials. In this study 4TaC-HfC compacts were prepared at relatively low temperature (thereby saving energy and reducing cost). The properties of consolidated samples of 4TaC-HfC were characterized at different milling conditions, and with three different amounts of WC addition (0 vol.%, 30 vol.%, and 50 vol.%). Each specimen's densification, microstructure, and hardness were characterized; XRD and SEM analyses were employed for both powder and consolidated samples.

5.3 Experimental:

5.3.1 Preparation of the starting powders

Ta_4HfC_5 specimens were prepared by mixing high-purity starting powders of TaC and HfC (both 99.5% purity, particle sizes from ~0.2 to ~2.0 μm) in a He-atmosphere. A Spex-8000 mixer/mill was used to comminute the powders in sealed, hardened steel vials with chrome-steel milling media. The constituents were milled for varying times up to a maximum of 18 hours. For some samples, the mechanically alloyed 4TaC-HfC powder was then blended with 30 or 50 vol. % WC, and milled for an additional 1 hour. All powder handling occurred in a He-atmosphere glove box to minimize oxygen contamination.

5.3.2 Consolidation

Powder consolidation was performed in a 75-ton Centorr hot press using graphite dies under a flowing argon atmosphere. All samples were pressed for 60 min at 1500°C under an applied pressure of 106 MPa.

5.3.3 Analysis

XRD was employed to identify the formation of Ta_4HfC_5 phase. The hot-pressed microstructures of fracture surface were analyzed by SEM and EDS. Density was determined by the Archimedes displacement method. Hardness was measured at a load of 2000 g by Vickers microindentation with a Wilson-Tukon 2100B microhardness tester. The hardness values of the materials investigated were measured as the average of 10 readings along the cross section surface of polished specimens.

5.4 Results and Discussion:

5.4.1 Powder Characterization

Fig. 1 shows the XRD patterns of the 4TaC-HfC for 4 different milling times; at 0, 1, 6 and 18 hours. The XRD patterns in Fig. 1 show that the powders display a small shift of the peaks after 1 hour and 6 hours, while after 18 hours no further shift is evident, but more peak broadening is observed, as indicated by the vertical line. Also, longer milling times give rise to reduced peak intensities. The shifting is due to uniform strain for 1 and 6 hours milling, while there is a non-uniform strain after 18hrs milling [46]. The full width at half maximum (FWHM) of the diffraction peaks increases with milling time due

to the strain and the refinement of powder size. Finer crystallites would decrease the consolidation temperature because the driving forces for sintering and contact points of powders for atomic diffusion both decrease [28]. Due to broadening and lower intensity of the peaks with time, HfC peaks almost disappear after 18 hours milling.

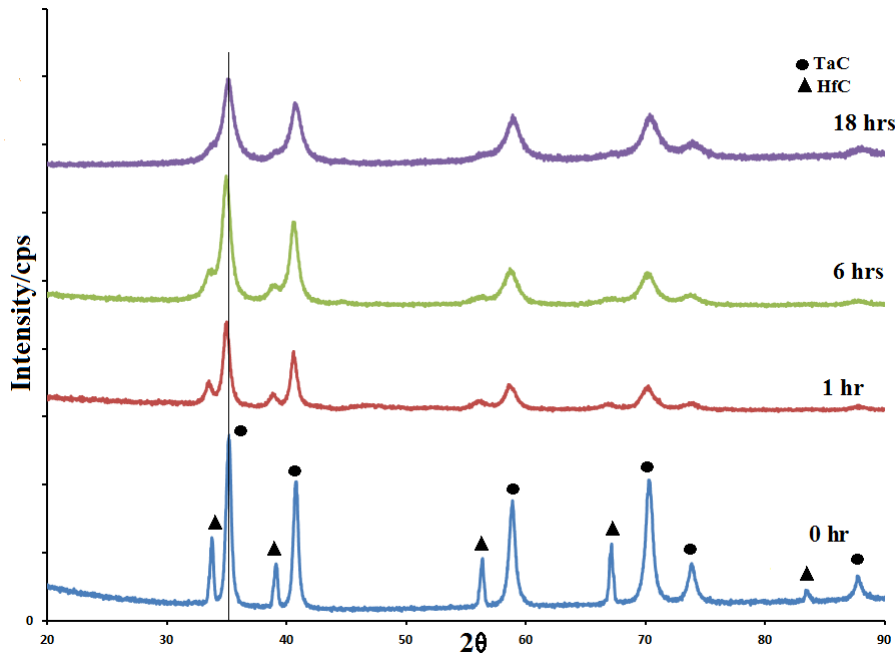
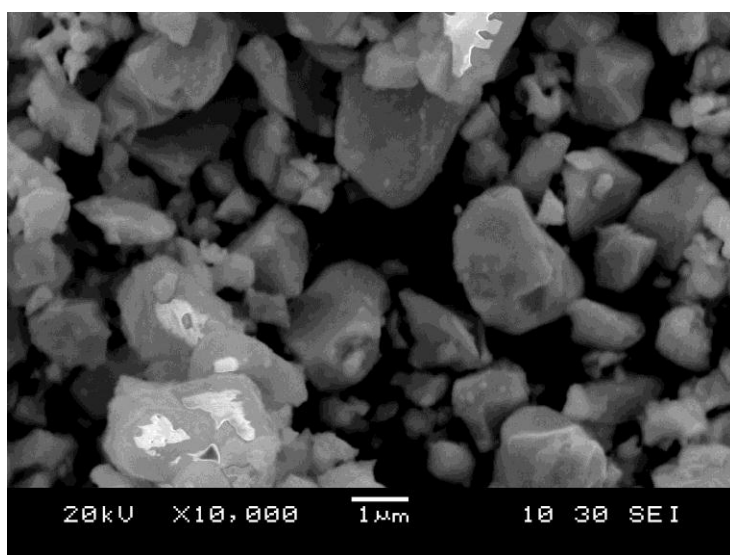
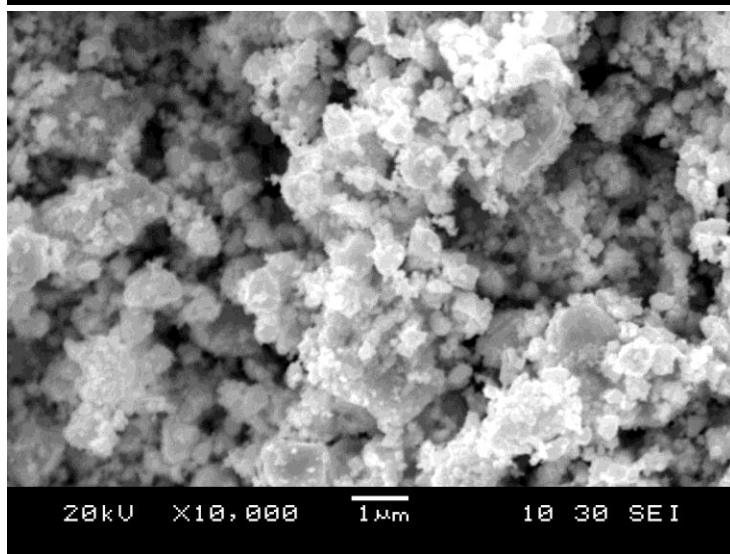


Fig. 1 XRD patterns of 4TaC-HfC powder after 0, 1, 6, and 18 hours milling time.

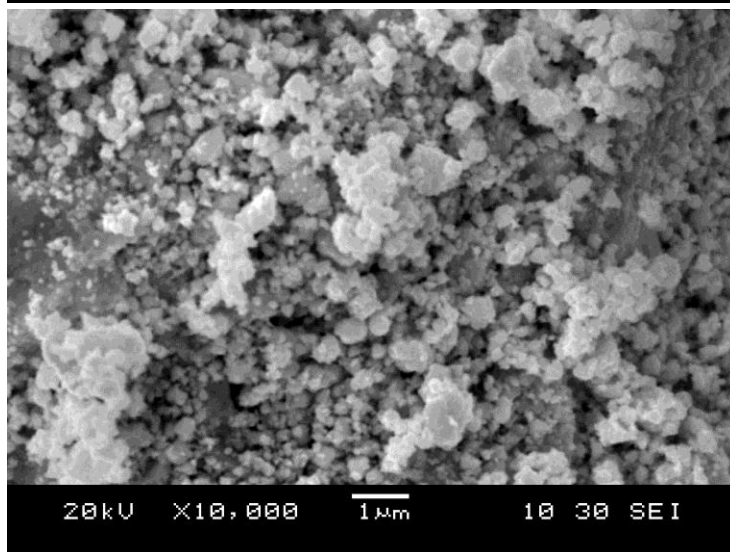
Fig. 2 shows the SEM images of the 4TaC-HfC at five different milling times (0, 3, 6, 9, and 18 hours). Fig. 2.a shows that the starting powder exhibits a range of particle sizes from ~ 0.2 to ~ 2.0 μm , where the larger particles correspond to TaC and the small ones correspond to HfC. As milling proceeds, particle size decreases up to 6 hours of milling, then increases at the highest milling time. The larger particles seen in Fig. 3d and Fig. 3e are actually agglomerates of much finer particles. The unmilled powder particles are characterized by angular shapes, while the milled powder particles become more rounded and refined with increasing milling times.



(a)



(b)



(c)

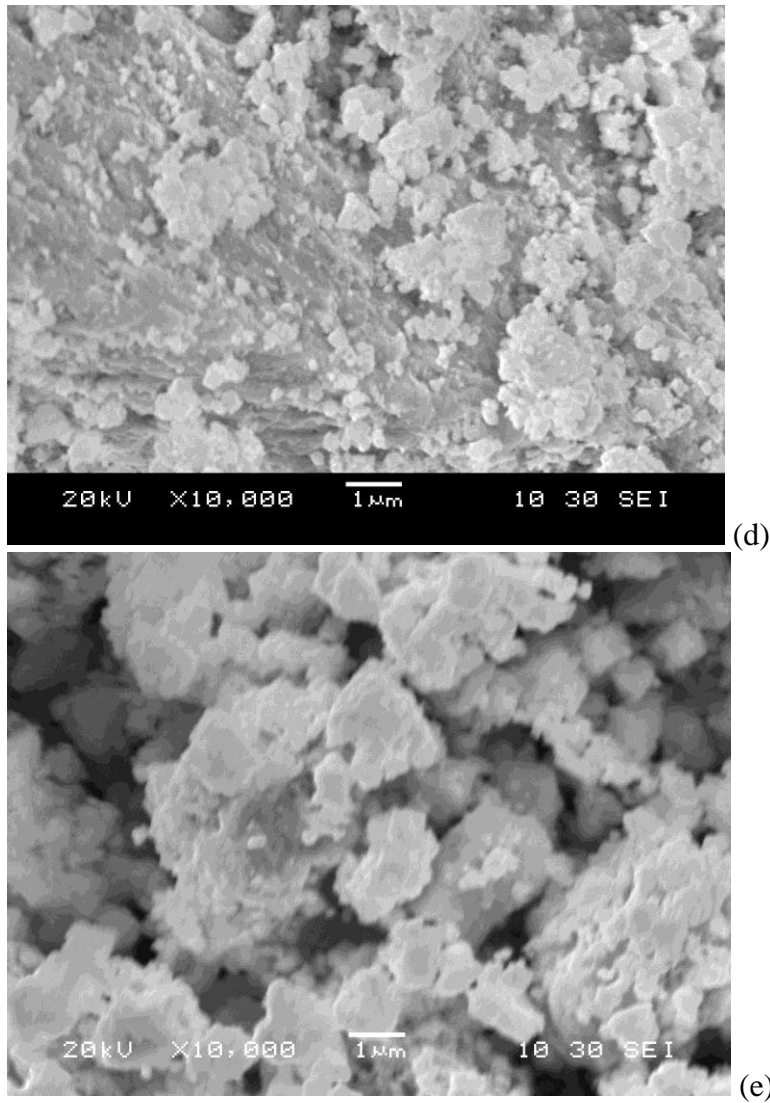


Fig. 2 Scanning electron microscopy images of a) the 4TaC-HfC powder mixture before milling b) After 3hrs milling c) after 6 hours milling d) After 9 hours milling e) After 18 hours milling

The application of high-energy ball milling can affect the rate of densification and the final density. High-energy ball milling produces finer crystallites, more strain, and higher concentrations of defects, all of which act to decrease consolidation temperature. A major issue related to the processing of powders by high-energy milling is the unavoidable introduction of impurities from wear debris. To minimize the amount of

contamination from grinding media and vessel abrasion, multiple milling runs were performed with the media and vials. In the first run, powder became coated onto the grinding medium and the inner walls of the vial. This tends to suppress subsequent wear of the grinding medium and also minimizes contamination of the powder from the steel vials and media. Repetition of this operation coats the steel surfaces with carbide and greatly reduces contamination by the underlying steel grinding media and vial [47].

Milling atmosphere has also been found to be a major cause of contamination in many milling studies. [48]. Therefore, the powders were milled in vials that were loaded in a He glove box atmosphere. The vials were sealed before their removal from the glove box to avoid contamination by air. Handling the powders in a He-atmosphere glove box minimized oxygen contamination and subsequent formation of oxide impurities that can affect the sintering temperature and grain coarsening in the later processing steps [49].

5.4.2. XRD, densification, microstructure, and hardness

We employed XRD to confirm formation of Ta_4HfC_5 , but no published XRD patterns for the Ta_4HfC_5 were available for comparison. Thus, CaRIne Crystallography 3.1 software was employed to generate a reference pattern. Table 1 shows the calculated values for Ta_4HfC_5 using structure factor, Bragg's Law, and other formulas from De Graef [50]. The values in Table 1 were confirmed using CaRIne Crystallography 3.1 software (Figure 3).

Table 1 Theoretical calculated values for XRD of ternary Ta_4HfC_5

(hkl)	(111)	(200)	(220)	(331)	(222)	(400)	(331)
2θ (deg.)	34.60627	40.173	58.116	69.4348	73.004	86.76	96.923
Relative Intensity	100	61.84	38.22	35.48	11.8	5.3	14.26

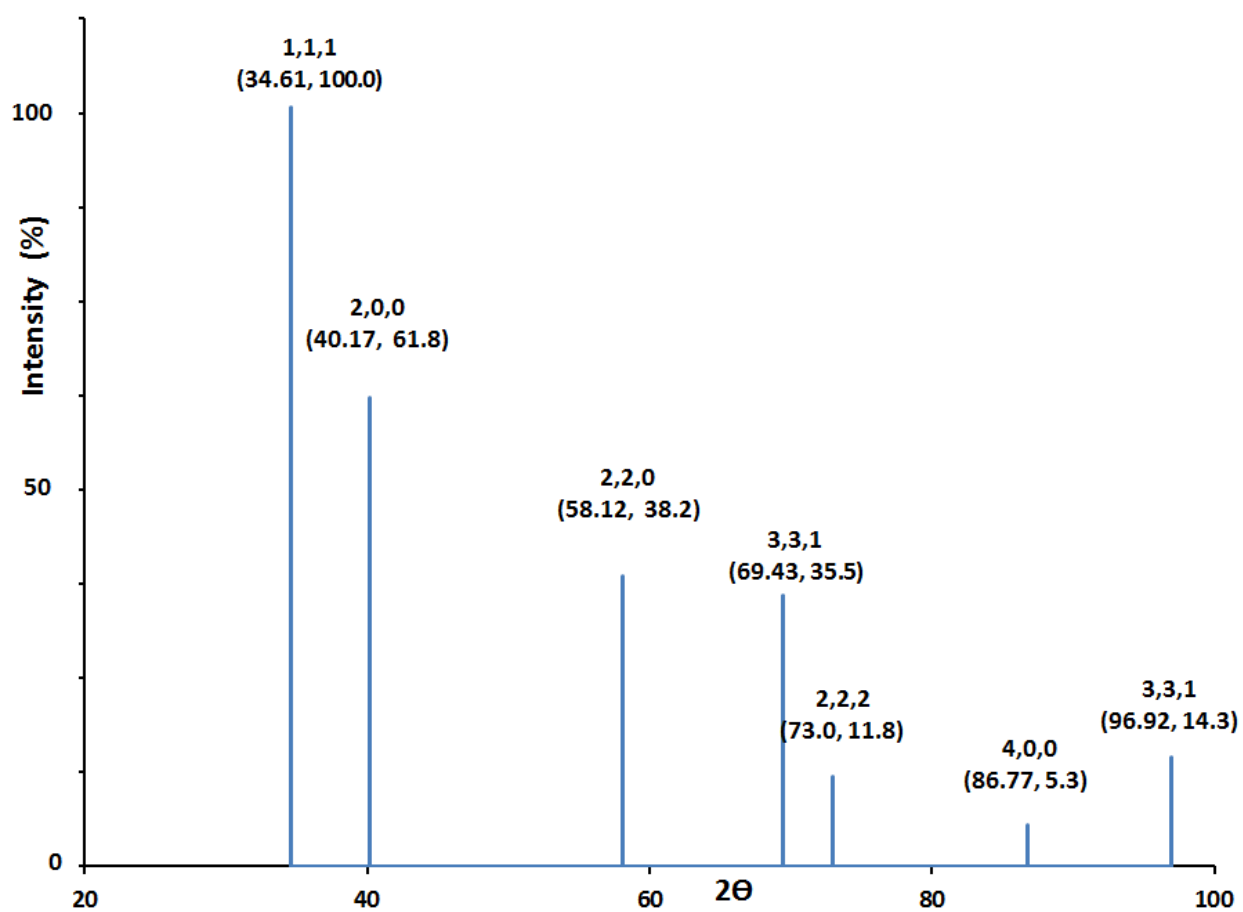
Fig. 3 XRD pattern of Ta_4HfC_5 calculated using CaRIne Crystallography 3.1 software.

Figure 4 shows the XRD pattern obtained for Ta_4HfC_5 after hot pressing at 1500°C for one hour. The lower XRD pattern in Fig. 4 corresponds to Ta_4HfC_5 after 6 hours milling, while the middle and upper patterns correspond to 9 and 18 hours of milling, respectively. All the peaks in Fig. 4 can be indexed to Ta_4HfC_5 ; each peak matches with the calculated one (Table 1 and Fig. 3). Fewer peaks are observed in Fig. 4, which could be explained by the negative correlation between the crystal symmetry and the number of peaks [50]. This result shows that hot pressing of TaC and HfC milled powders for 1 h under a pressure of 106 MPa at 1500°C can produce single-phase Ta_4HfC_5 . This formation can be correlated to the small grain size of the reacted powder plus the high pressure used during hot pressing [51].

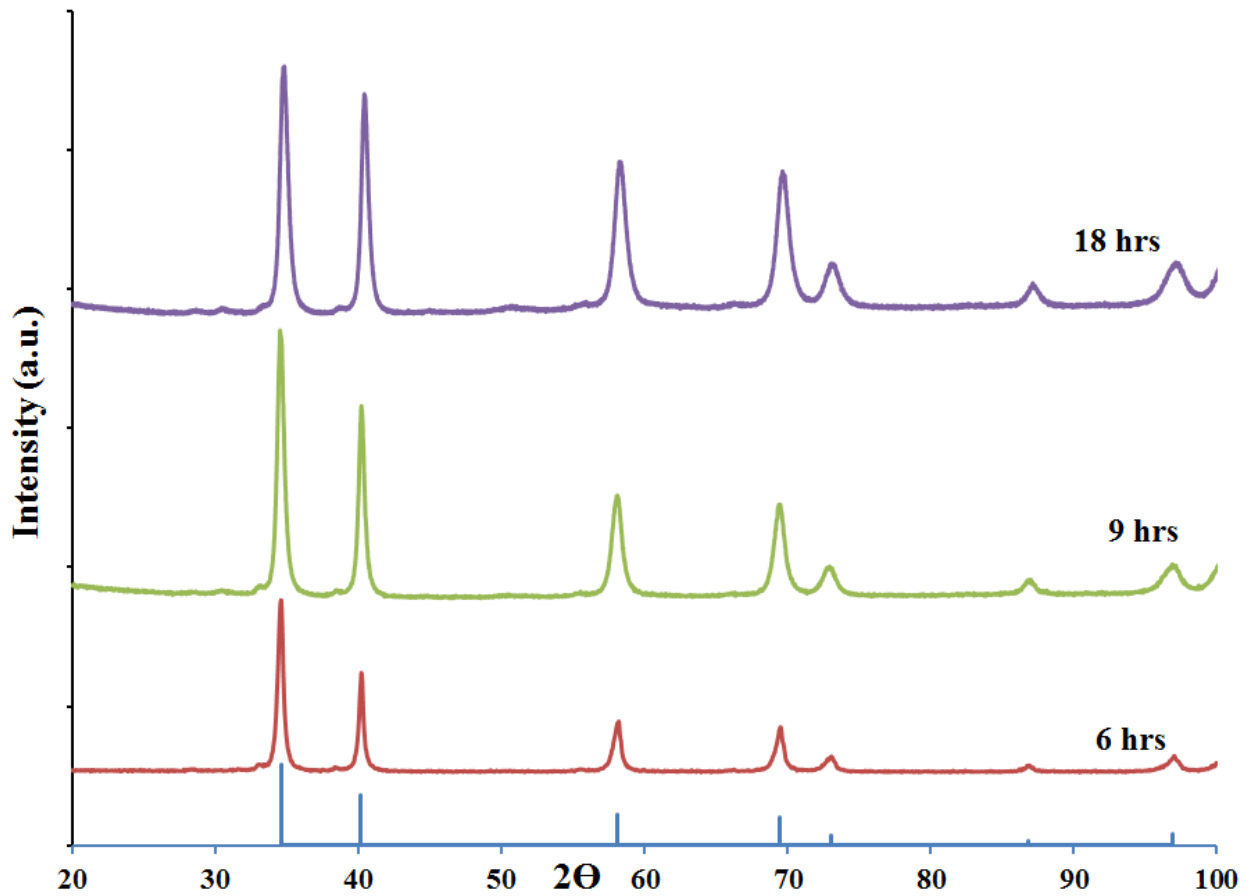


Fig. 4 XRD patterns of Ta_4HfC_5 hot pressed at 1500°C for 1 hour in flowing Ar at three different milling times; 6 hours, 9 hours, 18 hours. All the peaks correspond to Ta_4HfC_5 . The bottom of the figure shows the calculated pattern for Ta_4HfC_5 .

In past studies Ta_4HfC_5 has proven difficult to sinter because of the high temperatures ($\sim 2500^\circ\text{C}$) required. Such high temperatures lead to grain growth, which degrades mechanical properties. In many cases, sintering difficulties result from impurities, particularly oxide impurities. Even small amounts of certain impurities can lead to rapid grain growth [11]. Although there are no reports in the literature on low-temperature sintering of Ta_4HfC_5 , these difficulties have been overcome in this study by using powder

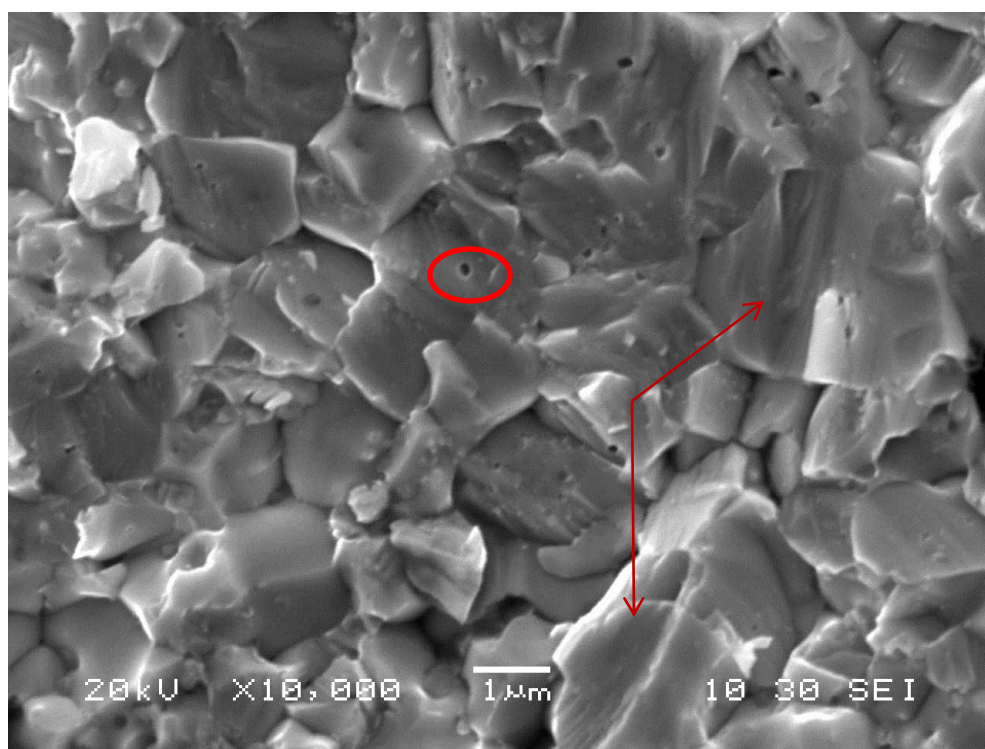
processing and high-pressure hot pressing, which make sintering possible at a reduced temperature.

We found that the relative densities of hot-pressed 4TaC-HfC increased as milling time increased, up to 9 hrs. Table 2 shows the 1500°C densification values for the four sintered Ta_4HfC_5 specimens after 3, 6, 9, and 18 hours milling. It can be seen that the Ta_4HfC_5 achieves nearly full densification (98.6%) after 9 hours milling.

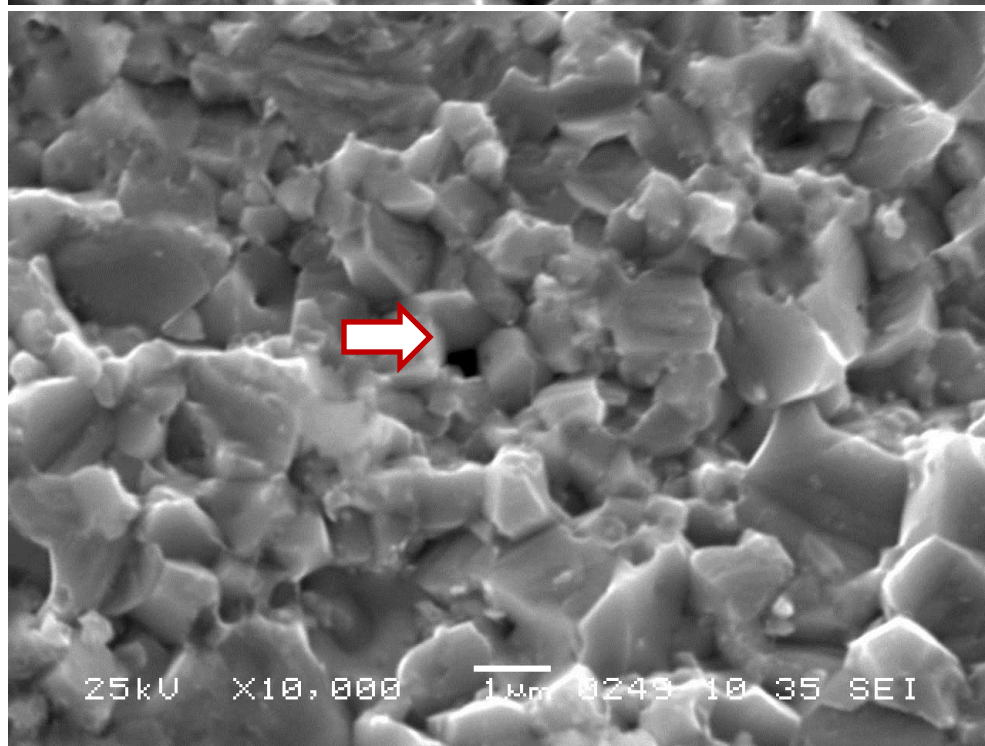
Figure 5 shows SEM micrographs of sintered Ta_4HfC_5 at four different milling times (3, 6, 9 and 18 hours). The SEM micrographs of the fractured surfaces facilitate characterization of grain size and porosity. Pores and Ta_4HfC_5 grains shown in these micrographs exhibit dark and light contrast, respectively. Fig. 5a showed many more pores than the other micrographs; these tended to appear in the inter-particle region and correspond to mixed mode fracture; trans-granular fracture (TG), and inter-granular fracture (IG). Figures 5b, c, and d showed low porosity with most of the pores segregated at multigrain junctions; these specimens showed IG fracture only.

It can be seen that the grain size becomes smaller as the milling time increases, which can help to achieve higher relative density and may lead to better mechanical properties [28].

It is clear that the grain size of the hot-pressed Ta_4HfC_5 was affected by the particle size of the starting powder. The grains range from more than a micrometer to sub-micron size. This is only slightly larger than the starting materials, which suggests that little grain growth occurred at the low sintering temperature used.



(a)



(b)

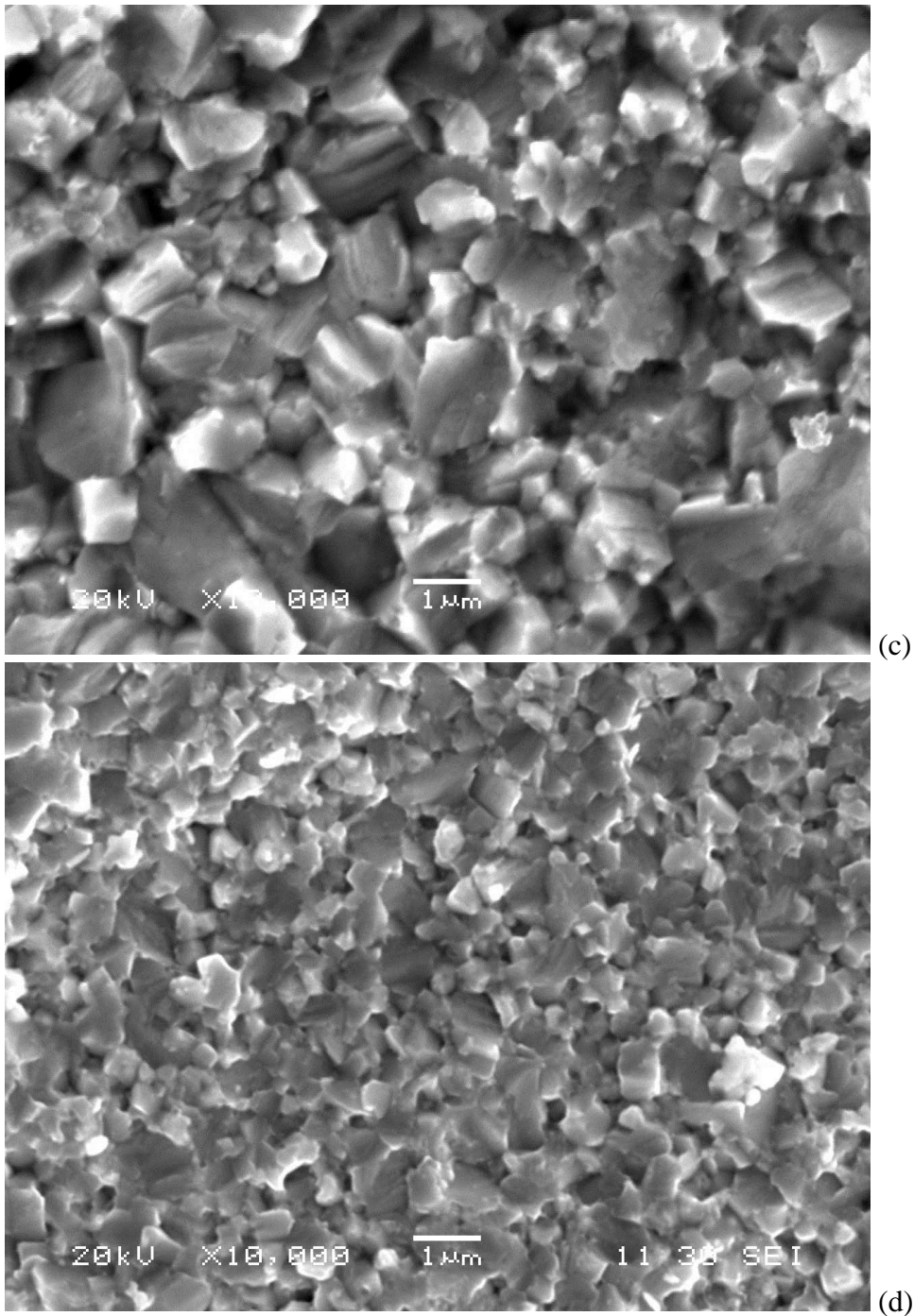


Fig. 5 Secondary electron SEM micrographs for fracture surface of hot pressed 4TaC-HfC at four different milling times; a) 3 hours, b) 6 hours, c) 9 hours, d) 18 hours, The thin arrows points to TG fracture, thick arrow shows multi-grain conjunction pore, and square shows an inter-granular pore. Minimization of oxide impurities is also thought to inhibit coarsening at intermediate

temperatures [52]. Overall, these microstructure observations indicate that high

densification can be achieved at 1500°C. We believe this low-temperature sintering was made possible by the efforts to minimize impurities, by use of high pressure for an extended time (1hour), and by use of fine powder as starting materials [53-55].

Hot pressing 4TaC-HfC to nearly full density at 1500°C is a noteworthy achievement, because this temperature corresponds to only 38% of the absolute melting temperature of Ta₄HfC₅, and this is thought to be the first time Ta₄HfC₅ has been sintered at such low temperature.

Table 2 Hardness and relative density of Ta₄HfC₅ at different milling times

Milling Time (hours)	Hardness (GPa at 1 kGf)	Relative density (%)
3	19.5	97
6	19.83	97.7
9	21	98.6
18	21.4	97

Table 2 shows the microhardness values measured in this study; these values are higher than those previously reported [3]. This could be correlated to the smaller grain size for the hot-pressed samples, a consequence of the comparatively low sintering temperature. Also, the hardness values increased as milling time increased. This is expected due to the reduction in grain size with increasing milling time and can be explained using the Hall-Petch relation between hardness and grain size. The smaller the grain size, the more grain boundaries are available to act as barriers to dislocation motion [56, 57].

5.4.3 Addition of 30% and 50% WC to Ta₄HfC₅

In this aspect of the study, WC powders (99.5% pure, 1 μm average size) were added to the 4TaC-HfC powder to form Ta₄HfC₅ + 30% WC, and Ta₄HfC₅ + 50% WC. These powders were also hot pressed at 1500°C, the resulting phases examined using XRD and SEM, and the relative density and hardness were measured.

The XRD patterns show distinct hexagonal crystal structures for the WC and a cubic crystal structure for the Ta₄HfC₅. As shown in Fig. 6B, the intensities of WC peaks are higher relatively to those peaks in Fig.6A, obviously due to the increased percent of WC from 30% to 50%.

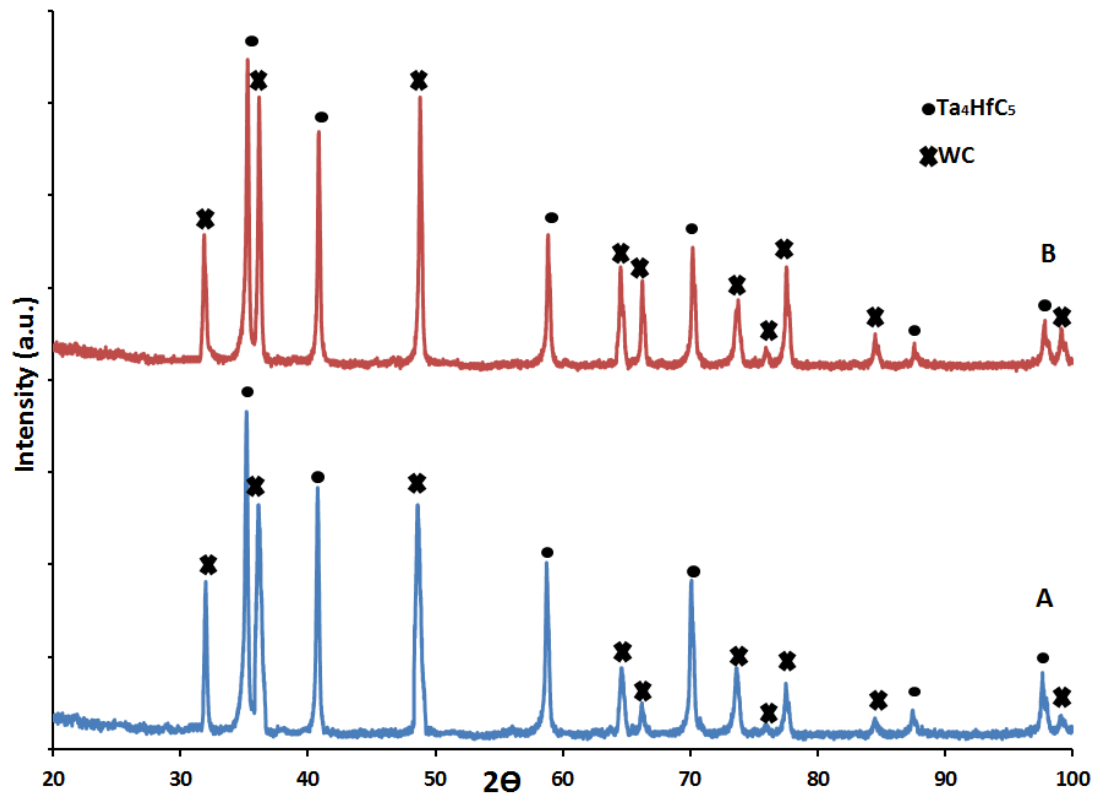


Fig. 6 XRD patterns of A) Ta₄HfC₅+30% WC, and B) Ta₄HfC₅+50%WC hot pressed at 1500°C for 1 h in flowing Ar.

Figure 7 shows fracture surfaces of the hot-pressed Ta_4HfC_5 (after 6hrs milling), Ta_4HfC_5 + 30% WC, and Ta_4HfC_5 +50% WC. Figs. 7B and 7C show that the average grain sizes of the samples containing WC were less than 1 μm , which is smaller than the sample without WC (Fig. 7A). The finer grain size also appears to correlate with higher densification; Table 3 shows an increase in densification from 97.7% for Ta_4HfC_5 up to 99% for the samples containing WC. Also, slightly higher grain size was observed in Fig. 7C (higher WC percent) compared to Fig. 7B.

Grain growth in WC in the presence of carbon has been noted previously, but is not well-understood; it may be that carbon lowers the activation energy of two-dimensional nucleation on singular grain boundary surfaces in WC [58].

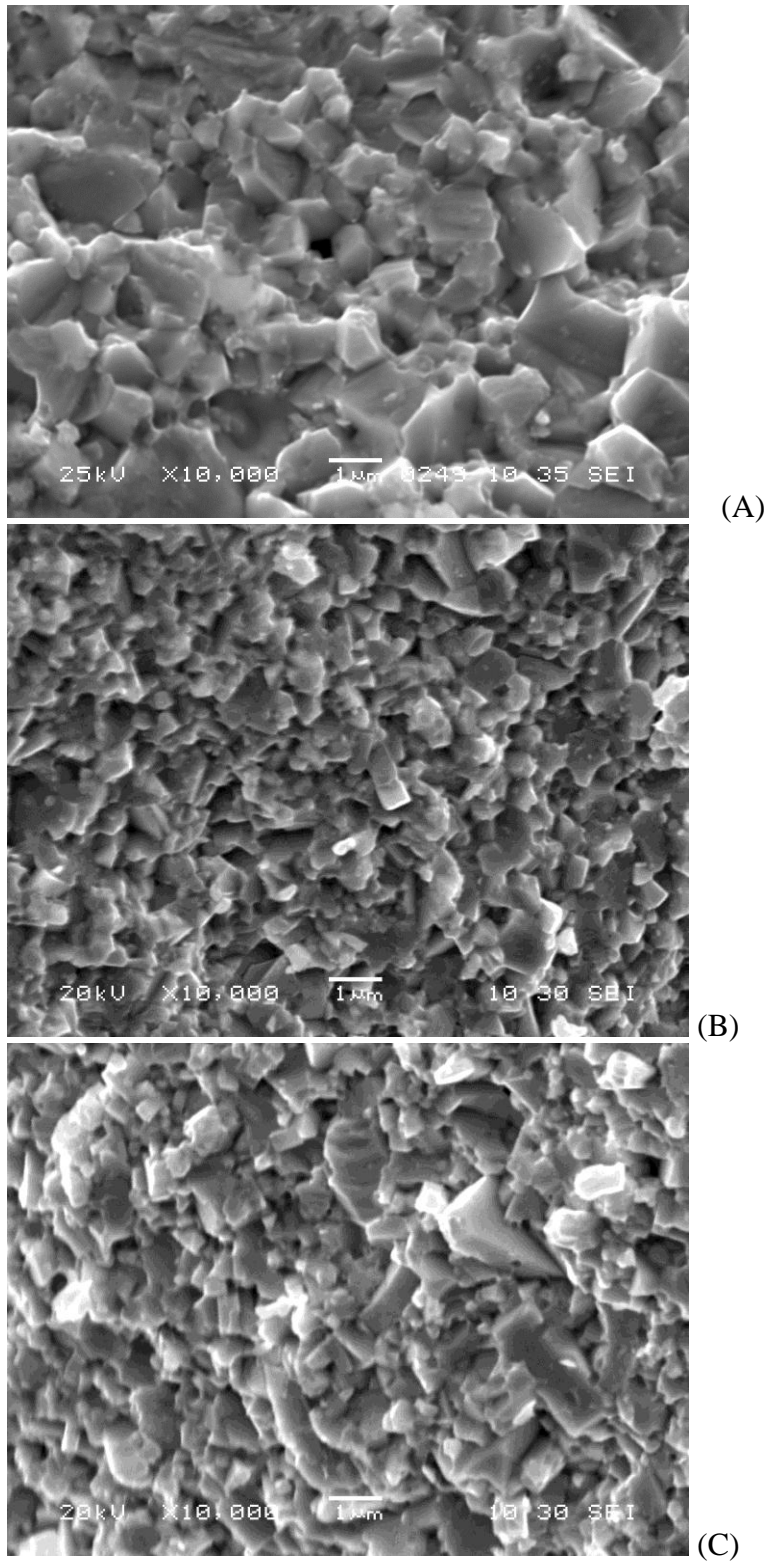


Fig. 7 Secondary electron SEM micrographs for fracture surface of hot pressed A) Ta_4HfC_5 (6hrs milling), B) $\text{Ta}_4\text{HfC}_5+30\% \text{WC}$, and C) $\text{Ta}_4\text{HfC}_5+50\% \text{WC}$

Table 3 Hardness and relative density of Ta₄HfC₅, Ta₄HfC₅+30% WC, Ta₄HfC₅+50% WC

	Hardness (GPa)	Relative density (%)
Ta ₄ HfC ₅	19.83	97.7
Ta ₄ HfC ₅ +30% WC	22.5	99
Ta ₄ HfC ₅ +50% WC	20.1	98.8

Table 3 shows the 1500°C densification values for the three compositions examined in this study. It can be seen that the Ta₄HfC₅ achieved nearly full densification (97.7%), while addition of WC gave rise to still higher densification (99%). The high relative density percentages are thought to result mainly from rearrangement of grains, which results in closer packing. Also, the closer packing of grains may be facilitated by hot pressing [59]. The reason for the higher densification for samples with WC is unclear, but it may be due to the carbon content in the Ta₄HfC₅ + WC, where the presence of sufficient carbon may aid densification of WC as previously stated. The presence of sufficient carbon is consistent with the fact that all the experiments were performed in a controlled atmosphere in order to keep the oxygen content as low as possible and subsequently prevent decarburization due to reduction of surface oxide. In support of this explanation, Oscroft et al. [59] reported that the presence of oxygen in the chamber consumes carbon and consequently reduces the carbon content. Also, the XRD results confirmed the absence of W₂C, which is consistent with the absence of decarburization [60].

Hot pressing WC to high density at 1500°C is notable, because this temperature corresponds to only 52% of the absolute melting temperature of WC.

These results indicate that hot pressing of 4TaC-HfC powder with WC milled powders for 1 h under a pressure of 106 MPa at 1500°C is adequate to produce two-phase Ta₄HfC₅ + 30% WC or Ta₄HfC₅ + 50% WC with good phase purity.

5.5 Conclusions:

Ta₄HfC₅ is a promising material for a variety of demanding technological applications, especially for aerospace components as a bulk material and as a coating. The most notable result in this study is achieving nearly full densification for the highest known melting material (Ta₄HfC₅) at just 1500°C, a temperature much lower than any previously reported to sinter Ta₄HfC₅. This sintering temperature is just 38% of the Ta₄HfC₅ melting point. The decrease in the grain size of Ta₄HfC₅ by milling and the minimal amount of grain growth due to very low sintering temperature, produced microhardness for Ta₄HfC₅ higher than previously reported. When comparing Ta₄HfC₅ and Ta₄HfC₅ with WC additions, samples with WC show higher densification and higher hardness.

5.6. Acknowledgements

Work at the Ames Laboratory was supported by the U.S. Department of Energy, Division of Materials Science & Engineering under contract DE-AC02-07CH11358. One

of the authors (OG) wishes to acknowledge support from the Egyptian Ministry of Higher Education and Scientific Research.

Chapter 6: Conclusions

6.1 General conclusions

- Controlling powder processing, milling, and hot pressing of the powder can produce high-density material at lower sintering temperature. A lower sintering temperature for a material can decrease its grain coarsening, and so improve its properties. Lower temperatures also place fewer demands on sintering processing equipment and reduce sintering costs.
- Hot pressing of TaC and HfC milled powders for 1 h under a pressure of 106 MPa at 1500°C can produce single-phase Ta₄HfC₅. This formation can be correlated to the small grain size of the reacted powder plus the high pressure used during hot pressing.
- A nearly full densification of Ta₄HfC₅ was obtained at 1500°C. This is a noteworthy achievement, because this temperature corresponds to only 38% of the absolute melting temperature of Ta₄HfC₅, and this is thought to be the first time Ta₄HfC₅ has been sintered at such low temperature. We believe this low-temperature sintering was made possible by the efforts to minimize impurities, by use of high pressure for an extended time (1 hour), and by use of fine powder as starting materials.
- Hot pressing of 4TaC-HfC powder with WC milled powders for 1 h under a pressure of 106 MPa at 1500°C is adequate to produce two-phase Ta₄HfC₅ + 30% WC or Ta₄HfC₅ + 50% WC with good phase purity.

- The ability demonstrated by this study to produce bulk Ta_4HfC_5 with a fine grain structure at a lower sintering temperature opens the possibility of exploiting this material's unusual properties for a variety of demanding technological applications, especially for aerospace components as a bulk material and as a coating.
- The decrease in the grain size of Ta_4HfC_5 by milling and the minimal amount of grain growth due to very low sintering temperature, produced microhardness for Ta_4HfC_5 higher than those previously reported.
- ZrB_2 and HfB_2 additions to AlMgB_{14} show similar results to that with TiB_2 and could be promising in industrial applications as bulk materials and as coatings.
- Single-phase Al_4SiC_4 was produced at 1450°C , which is a lower temperature than has been previously reported.
- Adding WC to both Ta_4HfC_5 and Al_4SiC_4 increased densification and hardness. This is may be due to the carbon content in the $\text{Al}_4\text{SiC}_4 + \text{WC}$ or $\text{Ta}_4\text{HfC}_5 + \text{WC}$, where the presence of sufficient carbon can help the densification.

6.2 Future work:

Preliminary work has been done to use nano-scale Ta_4HfC_5 as a thin-film coating, as well as WB_4 and TaB_4 production and application as a thin-film coating. These results show promise, and if further work could be done this might lead to better properties for Ta_4HfC_5 and the possibility of making this material available as targets for producing coatings.

6.2.1 Nanostructured Ta₄HfC₅:

Many studies have been done on nanostructured materials that have shown such materials often possess properties superior to those of conventional materials. These enhanced properties can offer the potential for new applications. Nanowires of Si, TaC, HfC, and other materials have been produced, which prompted attempts to produce nanostructured Ta₄HfC₅. There are two mechanisms that can be exploited for nanowire formation, vapor-liquid-solid (VLS) and solid-liquid-solid (SLS). The main idea behind vapor-liquid-solid growth of nanowires is that the catalysts (usually Ni or Fe) act as a liquid-forming agent that reacts with the vapor phase and forms eutectic liquid droplets [1-3]. The steps for VLS can be seen in figure 1A [1]. The process for the SLS mechanism is shown in Figure 1B [2].

In this study iron was used as a forming agent. As mentioned in chapter 5, 4TaC-HfC powders were available that had been milled at different milling times (3, 6, 9, and 18 hours). These powders were prepared (see chapter 5) using samples milled in conditioned vials. Some work was also done with samples milled in unconditioned vials; these contain between 1- 3% iron from the milling wear debris. To explore the effects of varying Fe content on formation of nanostructured material, specimens were also prepared with additional Fe added (5% and 10%) to the conditioned samples.

The purpose was to check the most suitable conditions to achieve a nano Ta₄HfC₅ structure.

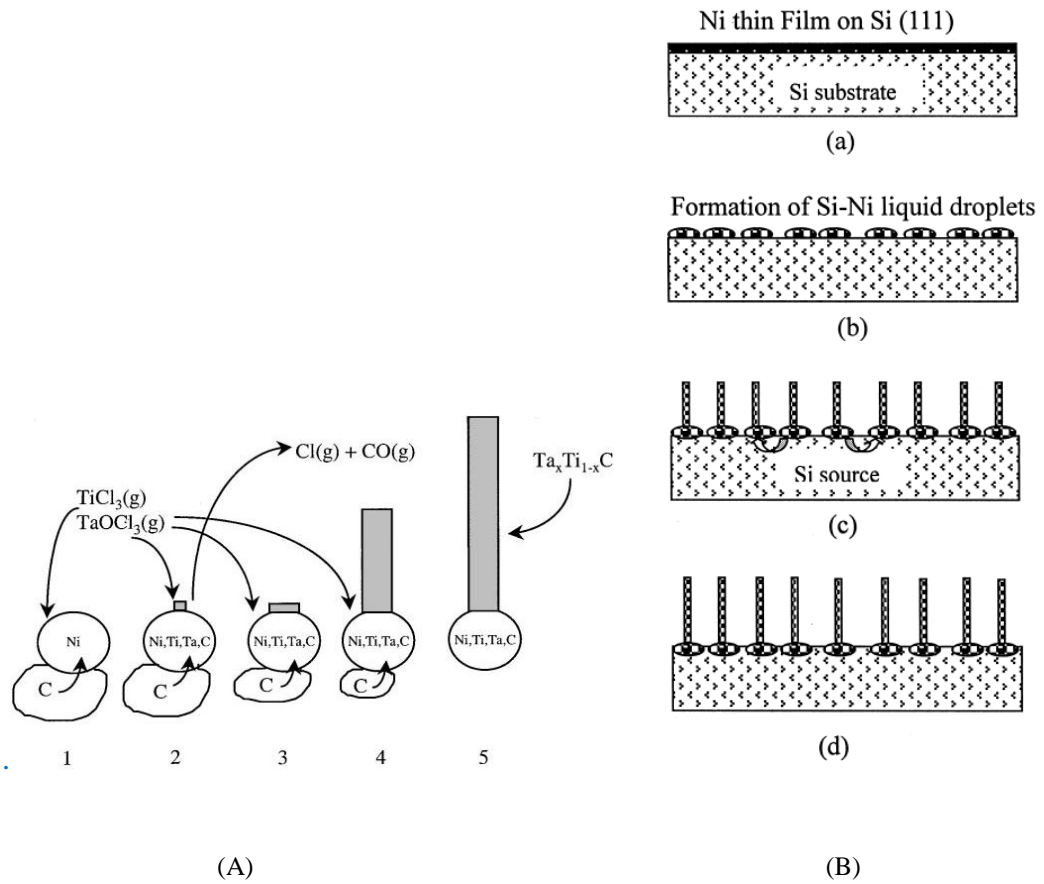


Fig 1 A) A simplified sequence for the carbothermal VLS growth mechanism; the reactions at the catalyst droplet can be described as follows: (1) the catalyst particle (Ni) in contact with carbon start to dissolve the whisker constituents: C, Ta, and Ti. (2) The droplet is supersaturated and a $\text{Ta}_x\text{Ti}_{1-x}\text{C}$ whisker is nucleated. (3) The surface tension balance at the interface between the whisker and the catalyst droplet determines the whisker diameter. (4) As the reactants are continuously being dissolved into the catalyst, the whisker grows, and the carbon particles are consumed. (5) When all carbon in contact with the catalyst droplet has been consumed, the whisker growth terminates. **B)** Schematic depiction of SiNW growth by the SLS mechanism: (a) deposition of a thin layer of Ni on the Si (111). Substrate; (b) formation of the Si-Ni eutectic liquid droplets; (c) continuous diffusion of Si atoms through the substrate-liquid (SL). Interface into the liquid droplets, and growth of SiNWs through the liquid-wire (LS) interface; (d) final state of SiNW growth. The smooth surface of the original substrate becomes rough at the end of SiNW growth [1, 2].

The results from this preliminary study indicate that the best conditions to form nanostructured Ta-Hf-C is milling for 9 hours with less than 3% Fe. As can be seen in Fig. 2a, around 20-30% of nano Ta_4HfC_5 can be obtained if unconditioned 4TaC-HfC is milled for 9 hours. Figure 2b is a higher magnification for the blue circle in Fig. 2a, and Fig. 2c is a higher magnification for the blue circle in Fig. 2b. The nano-structure filaments visible in Fig. 2c are fairly straight and smooth.

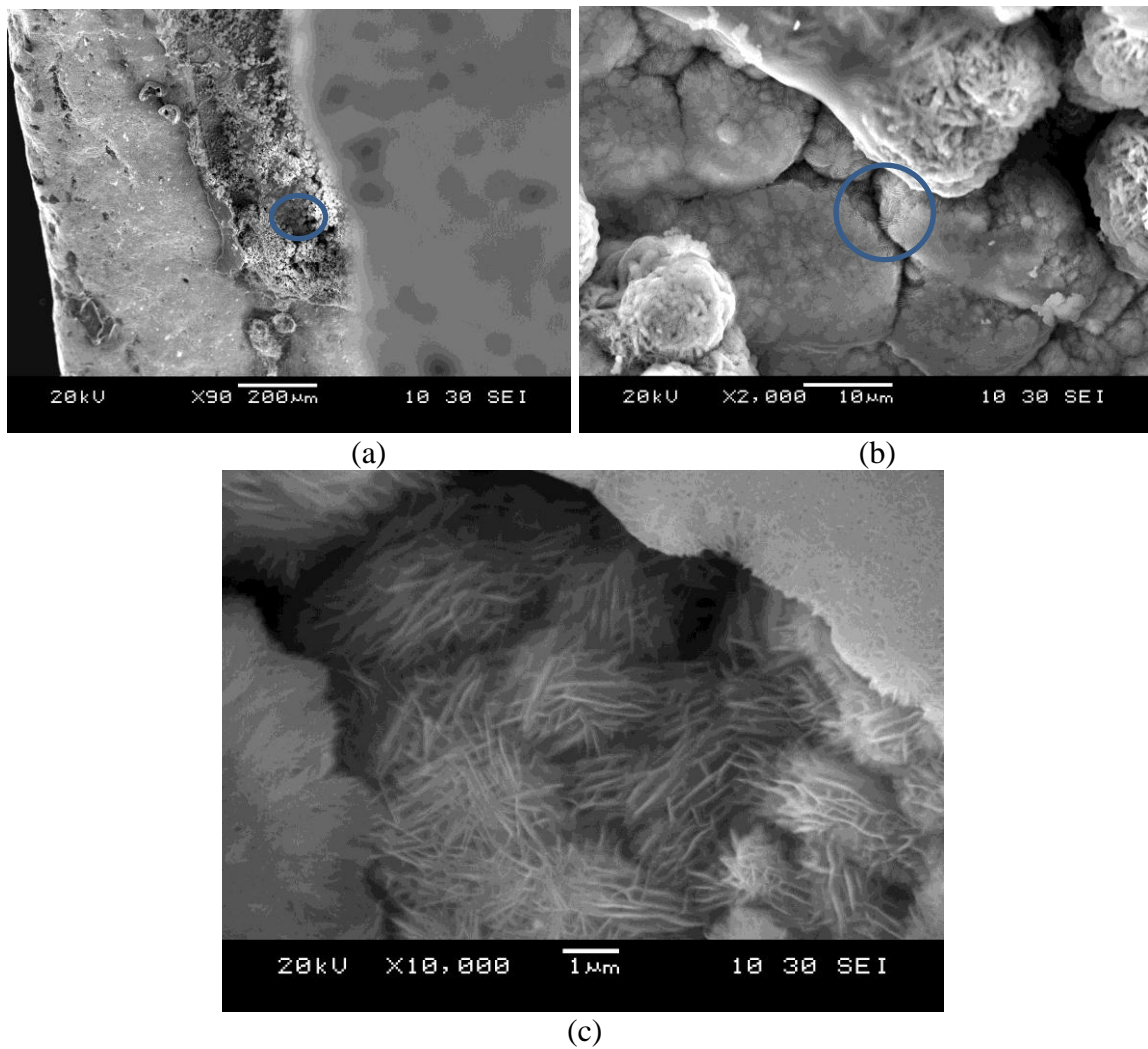


Fig. 2 – Nanostructured filaments visible in Ta_4HfC_5 after 9 hours milling in unconditioned vials

More work needs to be done to verify that the filaments visible in Fig. 2c are Ta_4HfC_5 , and to understand the mechanism driving their formation. It is possible that neither the VLS or SLS mechanisms apply completely in this case. By understanding the mechanism, a higher percentage of nano-structured filaments might be obtained.

Transmission electron microscopy (TEM) examination of the filaments could verify their crystal structure and improve understanding of what these filaments are and how they formed. Whisker diameter, in general, is larger with Fe than with Ni catalyst [1], so if TEM study showed that the filaments are indeed Ta_4HfC_5 , using Ni as a catalyst might produce a smaller filament size and better properties.

6.2.2 Ta_4HfC_5 coating

The preliminary results for using Ta_4HfC_5 as a coating material are shown in Fig. 3. It shows that Ta_4HfC_5 can be applied as a thin-film coating. Ta_4HfC_5 was successfully applied on a steel substrate. To test the adherence of these coatings, the Rockwell C indentation method provides a means to qualitatively assess the coating's adherence to the substrate (Fig. 3 right). There are moderate amounts of delamination and cracking of the film around the indent. The film shows radial cracks, but the appearance of these cracks indicates that the film is brittle rather than showing poor adherence of the film to the substrate. When comparing Fig. 3 with the DIN standard in Fig. 4, it most nearly resembles the HF4 rating [5, 6].

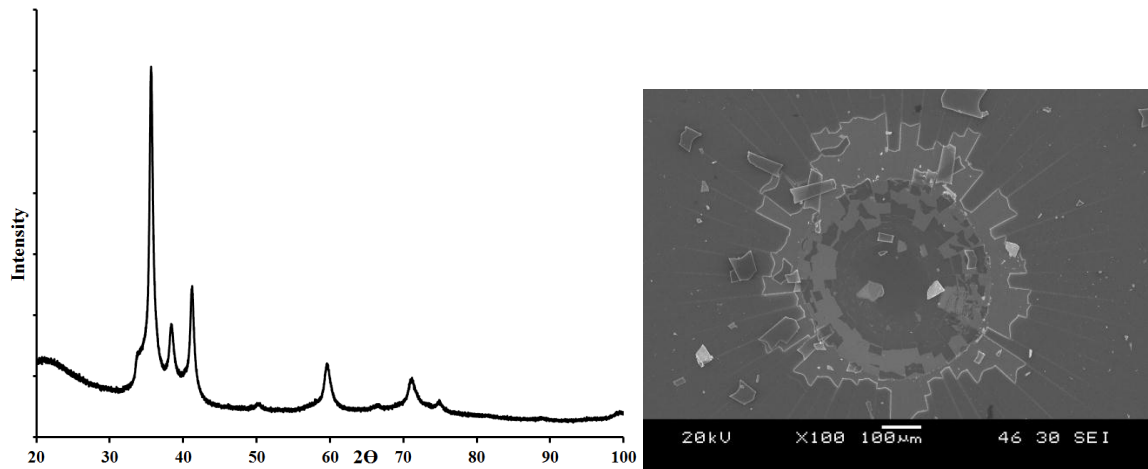


Fig. 3 XRD for Ta₄HfC₅ after pulsed laser deposition coating (left) and Rockwell C indent for Ta₄HfC₅ coating (right)

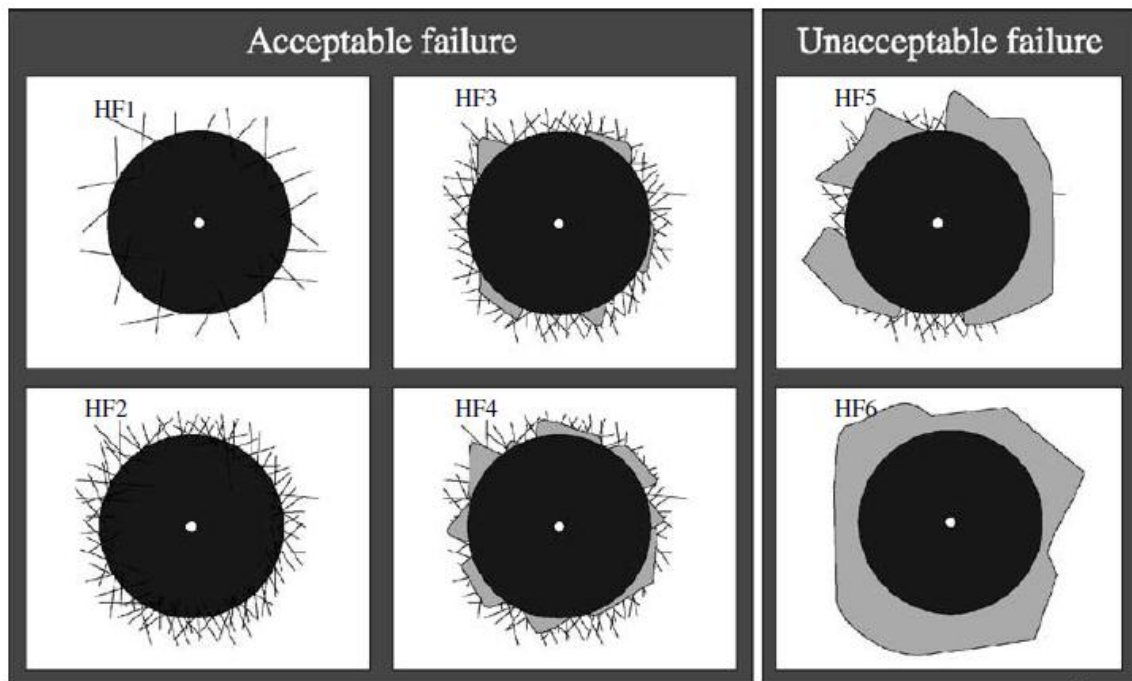


Figure 4: Standard images used to assess film adhesion with the DIN Rockwell C indentation method [4]

More work is needed to optimize the deposition parameters to (1) verify that the Ta₄HfC₅ coating possesses a nanocrystalline grain structure, and (2) attempt to produce better adhesion for Ta₄HfC₅ thin-film coatings.

6.2.3 WB₄ and TaB₄ formation and coating

As can be seen from chapter 5, the research focused on materials containing AlMgB₁₄. Additional exploratory work was performed on two other borides, WB₄ and TaB₄. The preliminary XRD results on WB₄ powders show the formation of WB₄ after 10 hours of milling. The resulting phase wasn't totally pure; there was W₂B₅ present in addition to the WB₄. For the specimen produced in the attempt to produce TaB₄, XRD showed a pattern similar to those published for WB₄ but with a small shift to the left on the 2 θ scale. Thus the success of the efforts to produce TaB₄ was difficult to confirm with certainty due to the absence of a reference pattern for TaB₄ in the literature. Deposition of both our WB₄ and putative TaB₄ material was successfully performed by pulsed laser femtosecond deposition, and a Rockwell C indent for WB₄ was done. When comparing the resulting Rockwell C indent for WB₄ shown in Fig. 5 with the DIN standard shown in Fig. 4, it is obvious that this WB₄ coating has excellent adherence. There are no cracks or delaminations present anywhere around the indentation, which suggests that it may be a promising candidate as a hard coating material.

The TaB₄ material needs further work to confirm that this stoichiometry is actually forming and to verify that the specimen is single-phase. It would also be useful to determine whether the TaB₄ material can be applied as a thin-film coating.

WB₄ needs more work to determine if a pure single phase can be produced and to compare the single-phase properties with those of the two-phase material already produced (WB₄ and W₂B₅).

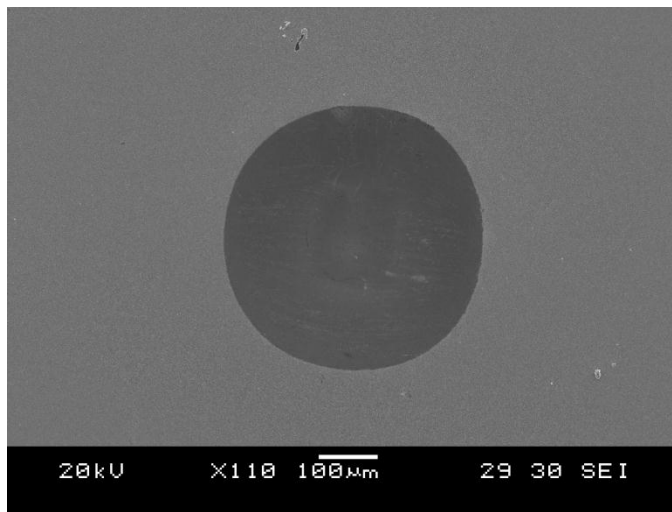


Fig. 5 A Rockwell C indent for WB_4 coating produced by pulsed laser deposition

Acknowledgements

- I would like to gratefully acknowledge Prof. Vitalij Pecharsky, Prof. Scott Chumbley, Prof. Kristen Constant, Prof. Sriram Sundararajan and Prof. Alan Russell for serving on my program of study committee.

- I want to thank Dr. Russell for guiding me through my PhD studies as my major professor.

- Special thanks are also due for Dr. Alan Russell, Dr. Bruce Cook, Mr. Joel Harringa, and Dr. Justin Peters for their patient assistance with my research project. Without their help and useful suggestions I would not have been able to complete this research project.

- Special thanks are also due for my family, especially my wife for their support throughout my graduate study years.

- I also gratefully acknowledge the government of my country (Egypt) for their support, especially Prof. Zeinab Abdel Hamid, the head of the corrosion and surface protection division, CMRDI, Cairo, Egypt and Prof. Mohamed Hamza, head of General Administration for Missions and Academic Supervision, higher ministry of education, Cairo, Egypt.

- This work was performed at Ames Laboratory and supported by the U.S. Department of Energy, Division of Materials Science & Engineering under contract DE-AC02-07CH11358.

Appendix: Standard Deviation for Calculated Hardness and Densities

The standard deviation (s) is a statistic used as a measure of the dispersion or variation in a distribution of N numbers, equal to the square root of the arithmetic mean of the squares of the deviations from the arithmetic mean (\bar{x}). It can be calculated with the following equation and six-step procedure:

$$s = \sqrt{\frac{1}{N-1} \sum_{i=1}^N (x_i - \bar{x})^2}$$

1. Compute the mean value of the N numbers.
2. Calculate the deviations.
3. Square each of these deviations.
4. Add the squares of all the deviations.
5. Divide that sum by N less one.
6. The square root of this result is the standard deviation.

For example, the standard deviation for the first hardness values measured in Table 2, page 85 for Ta₄HfC₅ can be determined as follows:

The readings are: 1998, 1903, 2046, 2007, 2074, 2037, 1871, 1947, 1985, 2012

- 1- The mean, $\bar{x} = 1988$
- 2- The deviations from the mean are 10, -85, 58, 19, 86, 49, -117, -41, -3, 24
- 3- The squares of these values are 100, 7225, 3364, 361, 7396, 2401, 13689, 1681, 9, 576
- 4- The sum of these squares is 36,802
- 5- Divide by total numbers less one $36,802/(10-1) = 4089.11$
- 6- The square root of this value is the standard deviation= 63.94

To convert the result to GPa, it is multiplied by 0.009807; **the result is 0.63.**

Following this procedure to determine the standard deviations for Table 1, page 44 resulted in the following:

	Al₄SiC₄	Al₄SiC₄ + 30% WC	Al₄SiC₄ +30% TiC
Relative density (%)	98.8±0.16	99.5±0.14	98±0.10
Vickers hardness (GPa)	12.7±0.63	14.6±0.24	15.5±0.67

For Table 2, page 85:

Milling Time (hours)	Hardness (GPa at 1 kgf)	Relative density (%)
3	19.5±0.63	97±0.28
6	19.83±0.30	97.7±0.26
9	21±0.45	98.6±0.20
18	21.4±0.57	97±0.28

For Table 3, page 89:

	Hardness (GPa)	Relative density (%)
Ta_4HfC_5	19.8 ± 0.30	97.7 ± 0.26
$\text{Ta}_4\text{HfC}_5 + 30\% \text{WC}$	22.5 ± 0.64	99 ± 0.36
$\text{Ta}_4\text{HfC}_5 + 50\% \text{WC}$	20.1 ± 0.29	98.8 ± 0.12

References:

Chapter 1:

- [1] Z. Inoue, Y. Inomata, H. Tanaka, H. Kawabata, *J. Mater. Sci.* 15 (3) (1980) 575–580.
- [2] S.U.H. Yokokawa, M. Fujita, M. Dokiya, *Metallurgical Transactions B* 18B (1987) 433–444.
- [3] G. Wen, X. Huang, *Journal of the European Ceramic Society* 26 (7) (2006) 1281–1286.
- [4] S.M. Koji Inoue, A. Yamaguchi, *J. Ceram. Soc. Jpn.* 111 (1290) (2003) 126–132.
- [5] X. Huang, G. Wen, X. Cheng, B. Zhang, *Corrosion Science* 49 (5) (2007) 2059–2070.
- [6] V. Solozhenko, O. Kurakevych, *Solid State Communications* 135 (1–2) (2005) 87–89.
- [7] S.M. Koji Inoue, A. Yamaguchi, *J. Ceram. Soc. Jpn.* 111 (1293) (2003) 348–351.
- [8] R. Beyer, E. Johnson, *The Journal of Chemical Thermodynamics* 16 (11) (1984) 1025–1029.
- [9] S.M. Koji Inoue, A. Yamaguchi, *J. Ceram. Soc. Jpn.* 111 (1292) (2003) 267–270.
- [10] J. Lee, S. Lee, T. Nishimura, H. Tanaka, *J. Ceram. Soc. Jpn.* 116 (1354) (2008) 717–721.
- [11] H Jian-feng, Z. Xie-rong, L. He-jun, X. Xin-bo, H. Min, *Mater. Lett.* 58 (21) (2004) 2627–2630.
- [12] O. Yamamoto, M. Ohtani, T. Sasamoto, *J. Materials Research* 17 (4) (2002) 774–778.
- [13] J. Zhao, W. Lin, A. Yamaguchi, J. Ommyoji, J. Sun, *J. Ceram. Soc. Jpn.* 115 (1347) (2007) 761–766.
- [14] K. Inoue, A. Yamaguchi, *J. Am. Ceram. Soc.* 86 (6) (2003) 1028–1030.
- [15] O. Yamamoto, *Solid State Sciences* 5 (2) (2003) 277–279.
- [16] K. Itatani, F. Takahashi, M. Aizawa, I. Okada, I. Davies, H. Suemasu, A. Nozue, *J. Mater. Sci.* 37 (2) (2002) 335–342.

- [17] S.M. Koji Inoue, A. Yamaguchi, J. Ceram. Soc. Jpn. 111 (1295) (2003) 466–470.
- [18] J.O. Motonari Fujita, A. Yamaguchi, J. Ceram. Soc. Jpn. 115 (4) (2007) 272–277.
- [19] O. Gaballa, B. Cook, A. Russell, Ceram. Int. (2010), doi:10.1016/j.ceramint.2011.05.050.
- [20] A.I. Gusev, , A.S. Kurlov and V.N. Lipatnikov, J. Solid State Chem. 180 (2007) 3234–3246.
- [21] Limeng Liu, Feng Ye, Yu Zhou. MAT SCI ENG A-STRUCT 528 (2011) 4710–4714.
- [22] Srinivasa R. Bakshia, Vishal Musaramthotaa, David A. Virzi, Anup K. Keshri, Debrupa Lahiri, Virendra Singhb, Sudipta Seal, Arvind Agarwal, Mat Sci Eng A-Struct 528 (2011) 2538–2547.
- [23] Srinivasa R. Bakshia, Vishal Musaramthotaa, Debrupa Lahiri a, Virendra Singhb, Sudipta Sealb, Arvind Agarwala, MAT SCI ENG A-STRUCT 528 (2011) 1287–1295.
- [24] G. R. Gruzalski and D. M. Zehner, Physical review B 42 (1990) 5.
- [25] C. Kim, G. Gottstein, D. S. Grummon. Acta metall, mater. 42, (7) (1994) 2291-2301.
- [26] Alpa Dashora,B.L.Ahuja. Radiation Physics and Chemistry 79 (2010) 1103–1110.
- [27] L. E. Toth, M. Ishikawa and Y. A. Chang Acta Metallurgica, 16 (1968) 1183-1187.
- [28] M. Desmaison-Brut, N. Alexandre and J. Desmaison Laboratoire de, J. Eur. Ceram. Soc. 17 (1997) 1325-1334.
- [29] A.L. Giorgi, E.G. Szklarz, E.K. Storms, A.L. Bowman, B.T. Matthias, Phys. Rev. 125 (1962) 837–838.
- [30] D. J. Rowcliffe, Mater. Sci. Res. 18, 49 (1983).
- [31] Xiaohong Zhang, Gregory E. Hilmas,William G. Fahrenholtz. Mat Sci Eng A-Struct 501 (2009) 37–43.
- [32] Laura Lo´pez-de-la-Torre, Bjo¨rn Winkler, Ju¨rgen Schreuer, Karsten Knorr, Miguel Avalos-Borja Solid State Communications 134 (2005) 245–250.
- [33] A.M. Fillippi, Met. Trans. 5 (1974) 1423–1427.

- [34] Byung-Ryang Kim , Kee-Do Woo , Jung-Mann Doh , Jin-Kook Yoon, In-Jin Shon. *Ceram. Int.* 35 (2009) 3395–3400.
- [35] Limeng Liu, Feng Ye, Yu Zhou. *Mat Sci Eng A-Struct* 528 (2011) 4710–4714.
- [36] Mingliang Ma, Weiping Shen, Pingping Zhang, Jiaqi Zhang, Qingyun Wang, Changchun Ge. *Materials Letters* 65 (2011) 96–99.
- [37] Xiaohong Zhang,w, Gregory E. Hilmas, and William G. Fahrenholtz. *J. Am. Ceram. Soc.*, 90 [2] (2007) 393–401.
- [38] I.G. Talmy, J.A. Zaykoski, M.M. Opeka. *J. Eur. Ceram. Soc.* 30 (2010) 2253–2263.
- [39] Preprint. Lei Xu & B.S. Majumdar, Darrell Marchant. Air Force Research Laboratory (AFMC).
- [40] C.L. Yeh , E.W. Liu. *Journal of Alloys and Compounds* 415 (2006) 66–72.
- [41] PM Special Feature, Technology of tantalum carbide, December, (1991) 30-34.
- [42] S. A. Shvab and P. S. Kislyi UDC 621.762 : 669.294. Poroshkovaya. *Metallurgiya*, 5 (137) (1974) 29-32.
- [43] J.S. Jackson, *Powder Metall.* 8 (1961) 73–100.
- [44] L. Ramqvist, *Powder Metall.* 9 (1966) 26–46.
- [45] E. Roeder, M. Klerk, *Z. Metalkunde* 54 (1963) 462–470.
- [46] J.J. Fischer, *Ceram. Bull.* 43 (1964) 183–185.
- [47] W.C. Yohe, A.L. Ruoff, *Ceram. Bull.* 57 (27) (1978) 647– 651.
- [48] Z. Shen, M. Johnsson, Z. Zhao, M. Nygren, *J. Am.Ceram. Soc.* 85 (2002) 1921–1927.
- [49] Evan Khaleghi,Yen-Shan Lin, Marc A. Meyersb and Eugene A. Olevskya, *Scripta Materialia* 63 (2010) 577–580.
- [50] Ramqvist L. *Jemkont Ann* 153 (1969) 1–21.
- [51] Vin~es F, Sousa C, Liu P, Rodriguez JA, Illas F. *J Chem Phys* 2005;122: 1747091–17470111.
- [52] Zaoui A, Bouhafs B, Ruterana P. *Mater Chem Phys* 2005;91:108–15.

- [53] Campbell, I. E. and Sherwood, E. M., ed. High-Temperature Materials and Technology, Wiley, New York, 1967.
- [54] Levine, S. R. et al., J. Eur. Ceram. Soc. 2002, 22(14–15), 2757–2767.
- [55] Opeka, M., Talmy, I. G., Wuchina, E. J., Zaykoski, J. A. and Causey, S. J., J. Eur. Ceram. Soc. 19 (1999) 2405–2414.
- [56] Wuchina, E., Opeka, M., Causey, S., Spain, J., Cull, A., Routbort, J. et al., J. Mat. Sci., 2004, 39, 5939–5949.
- [57] Raffaele Savino, Mario De Stefano Fumoa, Laura Silvestroni b, Diletta Sciti J. Eur. Ceram. Soc. 28 (2008) 1899–1907.
- [58] A. Sayir, J. Mater. Sci. Lett. 2004, 39, 5995.
- [59] E. Wuchina, M. M. Opeka, S. Causey, J. Spain, A. Cull, J. Routbort, F. Guitierrez-Mora, J. Mater. Sci. 39 (2004) 5939.
- [60] M. D. Sacks, C.-A. Wang, Z. Yang, A. Jain, J. Mater. Sci. 2004, 39, 6057.
- [61] Stefano Guicciardi, Laura Silvestroni, Giuseppe Pezzotti and Diletta Sciti Adv. Eng. Mater. 9 (2007) 5.
- [62] C. K. Jun And P. T. B. Shaffer J. Less-Common Metals, 4 (1971) 323–327.
- [63] Krajewski, A, D'Alessio, L, De Maria, G, “Physico- Cryst. Res. Technol. 33 (3) (1998) 341–374.
- [64] Guanqun Li, Geyang Li. J. Coat. Technol. Res., 7 (3) 403–407, 2010.
- [65] Sayir, J. Mater. Sci. 39 (2004) 5995 – 6003.
- [66] T. Sato, M. Saida, K. Horikawa, and M. Sasaki J. Vac. Sci. Technol. B 23.2. 2005.
- [67] Diletta Sciti, w Laura Silvestroni, and Alida Bellosi. J. Am. Ceram. Soc., 89 (8) (2006) 2668–2670
- [68] L. Silvestroni, A. Bellosi, C. Melandri, D. Sciti, J.X. Liu, G.J. Zhang. J. Eur. Ceram. Soc. 31 (2011) 619–627
- [69] Diletta Sciti, Laura Silvestroni, Stefano Guicciardi, Daniele Dalle Fabbri, and Alida Bellosi. v. Mater. Res. 24 (6) (2009).

- [70] S.S. Ordanyan, G.P. Zaitsev, S.M. Tats, A.I. Avgustinik, *Izv. AN SSSR: Neorgan. Mater.* 12 (1976) 1577 (in Russian).
- [71] A.A. Lavrentyev, B.V. Gabrel'ian, V.B. Vorzhev, I.Ya. Nikiforov, O.Yu. Khyzhun, J.J. Rehr. *J. Alloy. Compd.* 462 (2008) 4–10.
- [72] Gusev, A I. *Russ. J. Phys. Chem.* Vol. 59, no. 3, pp. 579-584. Mar. 1985. (in Russian).
- [73] C. Agte, *Alterhum, Z. Physik*, No. 6 (1930).
- [74] R. A. Andrievskii, N. S. Strel'nikova, N. I. Poltoratskii, E. D. Kharkhardin, and V. S. Smirnov. *Poroshkovaya Metallurgiya*, 1 (49), (1967) 85-88.
- [75] Final Report, DOE Award Number: DE-FC07-05ID14673. Hui Zhang. (2008).
- [76] Helmut Holleck, Barbara Scholz, Helga Schneider, and Fritz Thummler. *Zeitschrift für metallkunde*, 65 (12) (1974) 738-747.
- [77] Project, 11.04-8061. 901690. NASA Lewis Research Center.
- [78] Mark Patterson, Contract No: NAS3-27272. NASA Lewis Research Center, (1999).
- [79] John J. Fischer. *The American ceramic Society Bulletin*, volume 43, 1964, 183-186.
- [80] Mei Wang, Yinwei Li, Tian Cui, Yanming Ma, and Guangtian Zou. *Appl Phys Lett* 2008;93:101905.
- [81] Ivanovskii, A.L., *Progress in Materials Science* (2011), doi: 10.1016/j.pmatsci.2011.05.004
- [82] Stan Vepreka, *J. Vac. Sci. Technol. B* 20.2., (2002).
- [83] K. S. Kovalchenko, L. G. Bodrova, and E.K. Fen. translated from *poroshkovaya metallurgiya*, 6 (150) (1975) 48-53.
- [84] Matkovich, V. I. and J. Economy, *Acta Crystallography: Section B*, 26, 1970, 616.
- [85] Higashi, Wami and Tetsuzo Ito, *Journal of the Less Common Metals*, 92, 1983, 239.
- [86] “Thermal and Physical Properties of Pure Metals” CRC: Handbook of Chemistry and Physics. Ed. David R. Lide. CRC Press. Ann Arbor, MI. 12-159.

- [87] Lewis, Theron L. A Study of Selected Properties and Applications of AlMgB₁₄ and Related Composites: Ultra-Hard Materials. MS Thesis. Iowa State University. Ames, IA. 2001.
- [88] Cook, B.A., J.L. Harringa, T.L. Lewis, A.M. Russell, and Y. Lee, Journal of Advanced Materials, 36(3), 2004, 56.
- [89] I. Higashi, M. Kobayashi, S. Okada, K. Hamano, T. Lundström T. Journal of Crystal Growth 128 (1993) 1113-1119.
- [90] B.A. Cook, J. L. Harringa, T. L. Lewis, A. M. Russell, Scripta Materialia 42 (2000) 597-602.
- [91] Peters, Justin, Bruce A. Cook, Joel L. Harringa, Alan M. Russell, and Alfred Kracher, Proceedings of the 2005 international conference on Powder Metallurgy and Particulate Materials, 2005, 12.
- [92] Lewis, T.L., B.A. Cook, J.L. Harringa, and A.M. Russell, Materials Science and Engineering A, 35, 2003, 117.
- [93] Freund, L.B. and S. Suresh. Thin Film Materials. Cambridge University Press, New York, New York. 2003.
- [94] Moelle, C., S. Klose, F. Szücs, H.J. Fecht, C. Johnston, P.R. Chalker, and M. Werner, Diamond and Related Materials, 6, 1997, 839
- [95] Justin Steven Peters, Improving hardness and toughness of boride composites based on AlMgB₁₄, PhD Thesis. Iowa State University, Ames, IA, 2007.
- [96] Cook, B.A., J.L. Harringa, T.L. Lewis, and A.M. Russell, A new class of ultra-hard materials based on AlMgB₁₄, Scripta Materialia, 42, 2000, 597.
- [97]. Y. Lee, B.N. Harmon, Journal of Alloys and Compounds 338 (2002) 242-247.
- [98] Suryanarayana C, editor. Non-equilibrium processing of materials, Oxford: Pergamon Press, 1999.
- [99] Suryanarayana C. Metals and Materials 1996; 2:195-209.
- [100] Weeber AW, Bakker H, deBoer FR. Europhys Lett 1986; 2:445-8.
- [101] C. Suryanarayana, Progress in Materials Science 46 (2001) 1-184
- [102] Benjamin JS. Sci Amer 1976; 234(5):40-8.

- [103] Benjamin JS. In: Arzt E, Schultz L, editors. Oberursel, Germany: DGM Informationgesellschaft, 1989. p. 3-18.
- [104] Benjamin JS. Metal Powder Rep 1990; 45:122-7.
- [105] Koch CC, Cavin OB, McKamey CG, Scarbrough JO. Appl Phys Lett 1983; 43:1017-9.
- [106] Koch, C. C., in Materials Science and Technology (Edited by R. W. Cahn, P. Haasen and E. J. Kramer). Weinheim VCH, 1991, Vol. 15, 193. p. 193-245.
- [107] Yamada K, Koch CC. J Mater Res 1993; 8:1317-26.
- [108] Di LM, Bakker H. J Phys C: Condens Matter 1991; 3:3427-32.
- [109] Haringa JL, Cook BA, Beaudry BJ. J Mater Sci 1992; 27:801-4.
- [110] Suryanarayana C. Intermetallics 1995 ;3:153-60.
- [111] Gavrilov D, Vinogradov O, Shaw WJD. In: Poursartip A, Street K, editors. Proc. Inter. Conf. on Composite Materials, ICCM-10, vol. III. Woodhead Publishing, 1995,11.
- [1112] Takacs L, Pardavi-Horvath M. J Appl Phys 1994; 75:5864-6.
- [113] Gerasimov KB, Gusev AA, Ivanov EY, Boldyrev VV. J Mater Sci 1991;26:2495-500.
- [114] Suryanarayana C, Ivanov E, NouR, Contreras MA, Moore JJ, J Mater Res 1999; 14:377-83.
- [115] Chin Z-H, Perng T-P. Mater Sci Forum 1997; 235-238:121-6.
- [116] Kis-Varga, Beke DL. Mater Sci Forum 1996; 225-227:465-70.
- [117] Miki M, Yamasaki T, Ogino Y. Mater Trans Japan Inst Metals 1992;33:839-44.
- [118] Chen Y, Williams JS. Mater Sci Forum 1996; 225-227:881-8.

Chapter 2:

- [1] G.R. Anstis, P. Chantikul, B.R. Lawn, D.B. Marshall, Journal of the American Ceramic Society 64 (1981) 533-538.

[2] D. Chicot, A. Pertuz, F. Roudet, M.H. Staia, J. Lesage, *Materials Science and Technology* 20 (2004) 877-884.

Chapter 3:

[1] Z. Inoue, Y. Inomata, H. Tanaka, H. Kawabata, X-ray crystallographic data on aluminum silicon carbide, α - Al_4SiC_4 and $\text{Al}_4\text{Si}_2\text{C}_5$, *Journal of Materials Science* 15 (3) (1980) 575–580.

[2] S.U.H. Yokokawa, M. Fujita, M. Dokiya, Phase relation associated with the aluminum blast furnace: aluminum oxycarbide melts and Al-C-X ($\text{X} = \text{Fe}, \text{Si}$) liquid alloy, *Metallurgical Transactions B* 18B (1987) 433–444.

[3] G. Wen, X. Huang, Increased high temperature strength and oxidation resistance of Al_4SiC_4 ceramics, *Journal of the European Ceramic Society* 26 (7) (2006) 1281–1286.

[4] S.M. Koji Inoue, A. Yamaguchi, Oxidation behavior of Al_4SiC_4 -SiC sintered bodies, *Journal of the Ceramic Society of Japan* 111 (1290) (2003) 126–132.

[5] X. Huang, G. Wen, X. Cheng, B. Zhang, Oxidation behavior of Al_4SiC_4 ceramic up to 1700 °C, *Corrosion Science* 49 (5) (2007) 2059–2070.

[6] V. Solozhenko, O. Kurakevych, Equation of state of aluminum silicon carbide $[\alpha]\text{-Al}_4\text{SiC}_4$, *Solid State Communications* 135 (1–2) (2005) 87–89.

[7] S.M. Koji Inoue, A. Yamaguchi, Thermal conductivity and temperature dependence of linear thermal expansion coefficient of Al_4SiC_4 sintered bodies prepared by pulse electronic current sintering, *Journal of the Ceramic Society of Japan* 111 (1293) (2003) 348–351.

[8] R. Beyer, E. Johnson, Heat capacity of aluminum silicon carbide (Al_4SiC_4) from 5.26 to 1047 K, *The Journal of Chemical Thermodynamics* 16 (11) (1984) 1025–1029.

[9] S.M. Koji Inoue, A. Yamaguchi, Temperature dependence of electrical resistivity of the Al_4SiC_4 sintered bodies prepared by pulse electronic current sintering, *Journal of the Ceramic Society of Japan* 111 (1292) (2003) 267–270.

[10] J. Lee, S. Lee, T. Nishimura, H. Tanaka, Synthesis of mono-phase, hexagonal plate-like Al_4SiC_4 powder via a carbothermal reduction process, *Journal of the Ceramic Society of Japan* 116 (1354) (2008) 717–721.

- [11] H Jian-feng, Z. Xie-rong, L. He-jun, X. Xin-bo, H. Min, Al_2O_3 -mullite-SiC- Al_4SiC_4 multi-composition coating for carbon/carbon composites, *Materials Letters* 58 (21) (2004) 2627–2630.
- [12] O. Yamamoto, M. Ohtani, T. Sasamoto, Preparation and oxidation of Al_4SiC_4 , *Journal of Materials Research* 17 (4) (2002) 774–778.
- [13] J. Zhao, W. Lin, A. Yamaguchi, J. Ommyoji, J. Sun, Synthesis of Al_4SiC_4 from alumina, silica and graphite, *Journal of the Ceramic Society of Japan* 115 (1347) (2007) 761–766.
- [14] K. Inoue, A. Yamaguchi, Synthesis of Al_4SiC_4 , *Journal of the American Ceramic Society* 86 (6) (2003) 1028–1030.
- [15] O. Yamamoto, Effect of triethanolamine on low-temperature preparation of aluminum silicon carbide, *Solid State Sciences* 5 (2) (2003) 277–279.
- [16] K. Itatani, F. Takahashi, M. Aizawa, I. Okada, I. Davies, H. Suemasu, A. Nozue, Densification and microstructural developments during the sintering of aluminium silicon carbide, *Journal of Materials Science* 37 (2) (2002) 335–342.
- [17] S.M. Koji Inoue, A. Yamaguchi, *Journal of the Ceramic Society of Japan* 111 (1295) (2003) 466–470.
- [18] J.O. Motonari Fujita, A. Yamaguchi, Influence of carbon on sintering of the Al–Si–C–N system composite, *Journal of the Ceramic Society of Japan* 115 (4) (2007) 272–277.
- [19] J. Peters, B. Cook, J. Harringa, A. Russell, Microstructure and wear resistance of low temperature hot pressed TiB_2 , *Wear* 266 (11–12) (2009) 1171–1177.
- [20] J. Peters, B. Cook, J. Harringa, A. Russell, Erosion resistance of TiB_2 – ZrB_2 composites, *Wear* 267 (1–4) (2009) 136–143.
- [21] S. Kang, D. Kim, Synthesis of nano-titanium diboride powders by carbothermal reduction, *Journal of the European Ceramic Society* 27 (2–3) (2007) 715–718.
- [22] R. Konigshofer, S. Fornsinn, P. Steinkellner, W. Lengauer, R. Haas, K. Rabitsch, M. Scheerer, Solid-state properties of hot-pressed TiB_2 ceramics, *International Journal of Refractory Metals and Hard Materials* 23 (4–6) (2005) 350–357.
- [23] M. Gu, C. Huang, B. Zou, B. Liu, Effect of (Ni, Mo) and TiN on the microstructure and mechanical properties of TiB_2 ceramic tool materials, *Materials Science and Engineering: A* 433 (1–2) (2006) 39–44.

- [24] J. Kim, H. Chung, S. Lee, K. Oh, J. Shim, Y. Cho, Mechanochemical synthesis of TiN/TiB₂/Ti-silicide nanocomposite powders and their thermal stability, *Intermetallics* 15 (2) (2007) 206–210.
- [25] S. Shvab, P. Kislyi, Some properties of tantalum carbide powder produced by synthesis from the elements, *Powder Metallurgy and Metal Ceramics* 13 (5) (1974) 368–370.
- [26] M. De Graef, M. McHenry, *Structure of Materials: An Introduction to Crystallography, Diffraction and Symmetry*, Cambridge University Press, 2007.
- [27] S. Cha, S. Hong, B. Kim, Spark plasma sintering behavior of nanocrystalline WC-10Co cemented carbide powders, *Materials Science and Engineering: A* 351 (1–2) (2003) 31–38.
- [28] R. Osof, D. Thompson, Influence of oxygen on the formation of aluminum silicon carbide, *Journal of the American Ceramic Society* 75 (1) (1992) 224–226.
- [29] L.K.R. Chaim, S. Kalabukhov, Densification of nanocrystalline tic ceramics by spark plasma sintering, *International Journal of Applied Ceramic Technology*, in press.
- [30] K. Tsai, The effect of consolidation parameters on the mechanical properties of binderless tungsten carbide, *International Journal of Refractory Metals and Hard Materials* 29 (2011) 188–201.
- [31] T. Li, Q. Li, J. Fuh, P. Yu, C. Wu, Effects of lower cobalt binder concentrations in sintering of tungsten carbide, *Materials Science and Engineering: A* 430 (1–2) (2006) 113–119.
- [32] K. Tsai, C. Hsieh, H. Lu, Sintering of binderless tungsten carbide, *Ceramics International* 36 (2) (2010) 689–692.
- [33] J. Viala, N. Peillon, F. Bosselet, J. Bouix, Phase equilibria at 1000 8C in the AlCSiTi quaternary system: an experimental approach, *Materials Science and Engineering: A* 229 (1–2) (1997) 95–113.

Chapter 4:

- [1] ASM Handbook, *Powder Metallurgy Technology and Application*, vol. 7, 1973.
- [2] B. Mill, *J. Mater. Process. Technol.* 56 (1996) 16–23.
- [3] P. Cosemans, X. Zhu, J.P. Celis, M. Van Stappen, *Surface and Coatings Technology* 174 –175 (2003) 416–420.

- [4] W.D. Fan, H. Wu, K. Jagannadham , B.C. Goral, Surface and Coatings Technology 72 (1995) 78-87.
- [5] B.A. Cook, J. L. Harringa, T. L. Lewis, A. M. Russell, Journal of Advanced Materials 36 (2004) 56-63.
- [6] B.A. Cook, J. L. Harringa, T. L. Lewis, A. M. Russell, Scripta Materialia 42 (2000) 597-602.
- [7] Liwen F Wan and Scott P Beckman, Materials Science and Engineering 18 (2011) 082024, doi:10.1088/1757-899X/18/8/082024.
- [8] Peters, J.S., Doctorate in Philosophy Thesis, Iowa State University of Science and Technology, Ames, IA, 2007.
- [9] Y. Lee, B.N. Harmon, Journal of Alloys and Compounds 338 (2002) 242-247.
- [10] W.G. Fahrenholtz, G. E. Hilmas, I. G. Talmy, and J. A. Zaykoski, Journal of the American Ceramic Society, 90 [5] (2007) 1347–64.
- [11] J.S. Petersa,b, B.A. Cookb, J.L. Harringab, A.M. Russell, Wear 267 (2009) 136–143
- [12] S. F. Moustafa, Z. Abdel-Hamid, Osama G. Baheig, A. Hussein, Advanced Powder Technology 22 (2011), 596-601.
- [13] D. Chicot, A. Pertuz, F. Roudet, M.H. Staia, J. Lesage, Materials Science and Technology 20 (2004) 877–884.
- [14] B.A. Cook, J.L. Harringa, J.S. Peters, A. M. Russell, Wear, 271 (2011) 640– 646.
- [15] Osama Gaballa, Bruce Cook, Alan Russell, Ceramics International 37 (2011) 3117–3121.
- [16] Liao P.K., and Spear K.E., B-Fe (Boron-Iron), Binary Alloy Phase Diagrams, II Ed., Ed. T.B. Massalski, Vol. 1, 1990, p 480-483.
- [17] A. M. Kueck, D. K. Kim, Q. M. Ramasse, L. C. De Jonghe, and R. O. Ritchie, Nano Lett., 2008, 8 (9), 2935–2939.
- [18] Physical metallurgy/ William F. Hosford, William F. Hosford, Boca Raton, FL : Taylor & Francis/CRC Press 2005.

Chapter 5:

- [1] C. Agte, Alterhum, Z. Physik, No. 6 (1930).
- [2] R. A. Andrievskii, N. S. Strel'nikova, N. I. Poltoratskii, E. D. Kharkhardin, and V. S. Smirnov. Poroshkovaya Metallurgiya, 1 (49), (1967) 85-88.
- [3] R. D. Koester and D. P. Moak, J. Am. Ceram. Soc. Volume 50, 1967; 290-297.
- [4] Srinivasa R. Bakshia, Vishal Musaramthotaa, David A. Virzi, Anup K. Keshri, Debrupa Lahiri, Virendra Singhb, Sudipta Seal, Arvind Agarwal, MAT SCI ENG A-STRUCT 528 (2011) 2538–2547.
- [5] Srinivasa R. Bakshia, Vishal Musaramthotaa, Debrupa Lahiri a, Virendra Singhb, Sudipta Sealb, Arvind Agarwala, MAT SCI ENG A-STRUCT 528 (2011) 1287–1295
- [6] G. R. Gruzalski and D. M. Zehner, Physical review B 42 (1990) 5.
- [7] C. Kim, G. Gottstein, D. S. Grummon. Acta metall, mater. 42, (7) (1994) 2291-2301.
- [8] M. Desmaison-Brut, N. Alexandre and J. Desmaison Laboratoire de. J. Eur. Ceram. Soc. 17 (1997) 1325-1334.
- [9] A.L. Giorgi, E.G. Szklarz, E.K. Storms, A.L. Bowman, B.T. Matthias, Phys. Rev. 125 (1962) 837–838.
- [10] D. J. Rowcliffe, Mater. Sci. Res. 18, 49 (1983).
- [11] Xiaohong Zhang, Gregory E. Hilmas, William G. Fahrenholtz. MAT SCI ENG A-STRUCT 501 (2009) 37–43.
- [12] L. L. Torre, B. Winkler, J. Schreuer, K. Knorr, M. A. Borja Solid State Commun. 134 (2005) 245–250
- [13] Ramqvist L. Jemkont Ann 153 (1969) 1–21.
- [14] Vin˜es F, Sousa C, Liu P, Rodriguez JA, Illas F. J Chem Phys 2005;122: 1747091–17470111.
- [15] Zaoui A, Bouhafs B, Ruterana P. Mater Chem Phys 2005;91:108–15.
- [16] Stefano Guicciardi, Laura Silvestroni, Giuseppe Pezzotti and Diletta Sciti Adv. Eng. Mater. 9 (2007) 5.

- [17] Campbell, I. E. and Sherwood, E. M., ed. High-Temperature Materials and Technology, Wiley, New York, 1967.
- [18] Levine, S. R. et al., J. Eur. Ceram. Soc., 2002, 22(14–15), 2757–2767.
- [19].Opeka, M., Talmy, I. G., Wuchina, E. J., Zaykoski, J. A. and Causey, S. J., J. Eur. Ceram. Soc. 19 (1999) 2405–2414.
- [20] Wuchina, E., Opeka, M., Causey, S., Spain, J., Cull, A., Routbort, J. et al., J. Mat. Sci., 2004, 39, 5939–5949.
- [21] Raffaele Savino , Mario De Stefano Fumoa, Laura Silvestroni b, Diletta Sciti J. Eur. Ceram. Soc. 28 (2008) 1899–1907.
- [22] A. Sayir, J. Mater. Sci. Lett. 2004, 39, 5995.
- [23] M. D. Sacks, C.-A. Wang, Z. Yang, A. Jain, J. Mater. Sci. 2004, 39, 6057.
- [24] C.K. Jun and P.T.B. Shaffer, J Less-common Met, 14 (1971) 323-327.
- [25] A.M. Fillippi, Met. Trans. 5 (1974) 1423–1427.
- [26] Byung-Ryang Kim , Kee-Do Woo , Jung-Mann Doh , Jin-Kook Yoon, In-Jin Shon. Ceram. Int. 35 (2009) 3395–3400.
- [27] Limeng Liu, Feng Ye, Yu Zhou. MAT SCI ENG A-STRUCT 528 (2011) 4710–4714.
- [28] Mingliang Ma, Weiping Shen, Pingping Zhang, Jiaqi Zhang, Qingyun Wang, Changchun Ge. Materials Letters 65 (2011) 96–99.
- [29] Xiaohong Zhang,w, Gregory E. Hilmas, and William G. Fahrenholtz. J. Am. Ceram. Soc., 90 [2] (2007) 393–401
- [30] I.G. Talmy, J.A. Zaykoski, M.M. Opeka. J. Eur. Ceram. Soc. 30 (2010) 2253–2263
- [31] C.L. Yeh , E.W. Liu. J. Alloy. Compd. 415 (2006) 66–72.
- [32] Krajewski, A, D’Alessio, L, De Maria, G, Physiso- Cryst. Res. Technol. 33 (3) (1998) 341–374.
- [33] Guanqun Li, Geyang Li. J. Coat. Technol. Res., 7 (3), 2010;403–407.
- [34] T. Sato, M. Saida, K. Horikawa, and M. Sasaki J. Vac. Sci. Technol. B 23.2. 2005.

- [35] E. Roeder, M. Klerk, Z. Metalkunde 54 (1963) 462–470.
- [36] J.J. Fischer, Ceram. Bull. 43 (1964) 183–185.
- [37] W.C. Yohe, A.L. Ruoff, Ceram. Bull. 57 (27) (1978) 647– 651.
- [38] Z. Shen, M. Johnsson, Z. Zhao, M. Nygren, J. Am.Ceram. Soc. 85 (2002) 1921–1927.
- [39] Evan Khaleghi, Yen-Shan Lin, Marc A. Meyersb and Eugene A. Olevskya, Scr. Mater. 63 (2010) 577–580.
- [40] Diletta Sciti, w Laura Silvestroni, and Alida Bellosi. J. Am. Ceram. Soc., 89 (8) (2006) 2668–2670.
- [41] L. Silvestroni , A. Bellosi , C. Melandri, D. Sciti , J.X. Liu , G.J. Zhang. J. Eur. Ceram. Soc. 31 (2011) 619–627.
- [42] Diletta Sciti, Laura Silvestroni, Stefano Guicciardi, Daniele Dalle Fabbriche, and Alida Bellosi. v. Mater. Res. 24 (6) (2009).
- [43] S.S. Ordanyan, G.P. Zaitsev, S.M. Tats, A.I. Avgustinik, Izv. AN SSSR: Neorgan. Mater. 12 (1976) 1577.
- [44] A.A. Lavrentyev , B.V. Gabrelian , V.B. Vorzhev , I.Ya. Nikiforov , O.Yu. Khyzhun, J.J. Rehr. J. Alloy. Compd. 462 (2008) 4–10.
- [45] Helmut Holleck, Barbara Scholz, Helga Schneider, and Fritz Thummler. Zeitschrift für metallkunde, 65 (12) (1974) 738-747
- [46] Ron Jenkins, Robert Snyder. Introduction to X-Ray Powder Diffractometry. John Wiley & sons.Inc.; 1996
- [47] El-Eskandarany MS, Aoki K, Suzuki K. J LESS-COMMON MET 1990;167:113-8.
- [48] Suryanarayana C. Intermetallics 1995;3:153-160.
- [49] C. Suryanarayana, Prog. Mater. Sci., 2001, 46, 1–184.
- [50] M. De Graef, M. McHenry, Structure of Materials: An Introduction to Crystallography, Diffraction and Symmetry, Cambridge University Press, 2007
- [51] W. D. Kingery, H. K. Bowen, D. R. Uhlmann, introduction to Ceramics, 2nd ed., John Wiley & Sons, Inc., New York, 1976

- [52] H. Lee and R. F. Speyer, J. Am. Ceram. Soc., 86 [9] 1468–73 (2003).
- [53] J.-X. Liu, Y.-M. Kan, G.-J. Zhang, J. Am. Ceram. Soc. 93 (2010) 370–373.
- [54] Z.A. Munir, U. Anselmi-Tamburini, M. Ohyanagi, J. Mater. Sci. 41 (2006) 763–777.
- [55] S.R. Bakshi, V. Musaramthota, D. Lahiri, V. Singh, S. Seal, A. Agarwal Mater., Sci. Eng. A, 528 (2011), 1287–1295.
- [56] E. O. Hall, Proc. Phys. Soc. London Vol 64 B, 1951, p747.
- [57] N. J. Petch, J. Iron Steel Inst. Vol. 174, 1953, p25.
- [58] O. Gaballa , B. Cook , A. Russell, Ceram. Int. 37 (2011) 3117–3121
- [59] R. Osof, D. Thompson, J. Am. Ceram. Soc. 75 (1) (1992) 224–226.
- [60] K. Tsai, Int. J. Refract. Met. Hard Mater. 29 (2011) 188–201.

Chapter 6:

- [1] Niklas AhleÅn, Mats Johnsson, Ann-Kristin Larsson, Bo Sundman Journal of the European Ceramic Society 20 (2000) 2607-2618.
- [2] H.F. Yan, Y.J. Xing, Q.L. Hang, D.P. Yu, Y.P. Wang, J. Xu, Z.H. Xi b, S.Q. Feng, Chemical Physics Letters 323 _2000. 224–228
- [3] M. Futamoto, I. Yuito and U. Kawabe, Journal of Crystal Growth 61(1983) 69-74.
- [4] Vidakis, N, A. Antoniadis, and N. Bilalis. Journal of Materials Processing. Technology, 143-144, 2003, 481
- [5] DIN standard, DIN CEN/TS 1071-8
- [6] Lackner, Jurgen, Surface and coating technology, 200, 2005, 1439